

# THE OPTICAL CONDUCTIVITY OF DIRAC MATERIALS



# PHYSICS AT THE DIRAC POINT – THE OPTICAL CONDUCTIVITY OF DIRAC MATERIALS

By

PHILLIP E. C. ASHBY, B.Sc., University of Calgary (2006)  
M.Sc., McMaster University (2009)

A Thesis  
Submitted to the School of Graduate Studies  
in Partial Fulfillment of the Requirements  
for the Degree  
Doctor of Philosophy

McMaster University  
©Copyright by Phillip E. C. Ashby, 2013.

DOCTOR OF PHILOSOPHY (2013)  
(Physics)

McMaster University  
Hamilton, Ontario

TITLE: Physics at the Dirac point – The optical conductivity of Dirac materials

AUTHOR: Phillip E. C. Ashby, B.Sc., University of Calgary (2006)  
M.Sc., McMaster University (2009)

SUPERVISOR: Distinguished University Professor J. P. Carbotte

NUMBER OF PAGES: vi, 81

# Abstract

In this thesis, we present the results for the finite frequency response of a variety of materials. These materials all share the common theme that their low energy excitations are Dirac-like. This coincidence was not by design, and highlights the now-ubiquitous nature of Dirac-quasiparticles in condensed matter physics. We present results for graphene, the high temperature superconducting cuprates, and Weyl semi metals.

For graphene, our calculations revolve around a new experimental technique: Near field infrared spectroscopy. Conventionally it is ok to use the  $\mathbf{q} \rightarrow 0$  limit when calculating the low energy optical response. This new technique is able to directly probe the finite  $\mathbf{q}$  response by using an atomic force microscope tip as an antenna. We computed the optical conductivity of graphene at finite wavevector and studied how the quasiparticle peak is altered by disorder and the electron-phonon interaction.

The calculations on the high  $T_c$  cuprates use a model of the pseudogap phase known as the Yang, Rice and Zhang (YRZ) model. We employed the model to study the resistivity in the pseudogap regime, both in-plane and along the  $c$ -axis. We used a coherent tunneling matrix element to describe transport along the  $c$ -axis. We found that the model was able to reproduce the metalliclike behavior in the plane while being resistive out of plane. We then extended the model to the finite frequency response, as well as the superconducting phase. We found a pseudogap feature at finite frequency that was previously explained through an interlayer collective mode. We also found that microwave spectroscopy puts strong limits on the form of the scattering rate.

Finally, we computed the optical response of Weyl semimetals subjected to an applied magnetic field. Weyl semimetals are a topological phase of matter that have yet to be observed. The form of the conductivity contains a series of asymmetric peaks, whose spacing is a signature of the underlying relativistic dispersion. These peaks remain robust, even with moderate disorder.

# Preface

This is a ‘sandwich thesis’. It contains five published articles. The surrounding material is meant to provide background and place the work into a broader context. All of the original research is found in the five publications.

For the four publications:

Phillip E.C. Ashby and J.P. Carbotte “*Tracking quasiparticle energies in graphene with near-field optics*” Phys. Rev. B **86** 165405 (2012).

Phillip E.C. Ashby and J.P. Carbotte “*Resonating valence bonds and Fermi surface reconstruction: Resistivity in the underdoped cuprates*” Phys. Rev. B **87** 014514 (2013).

Phillip E.C. Ashby and J.P. Carbotte “*c-axis optical conductivity from the Yang-Rice-Zhang model of the underdoped cuprates*” Phys. Rev. B **87** 0184514 (2013).

and

Phillip E.C. Ashby and J.P. Carbotte “*Magneto-optical conductivity of Weyl semimetals*” Phys. Rev. B **87** 245131 (2013).

I am the primary author. I wrote the manuscripts, did all the calculations, and made all of the figures. Jules provided help along the journey, and provided useful edits and advice for the manuscripts I produced.

For the paper

J.P. Carbotte, J.P.F. LeBlanc and Phillip E.C. Ashby “*Impact of electron-phonon coupling on near-field optical spectra in graphene*” Phys. Rev. B **87** 045405 (2013).

I do not appear as the primary author. My contributions to the main text of this article are at the 10% level, but this manuscript could not have moved forward without the insight and results of my previous paper on near field optics. I helped James with two of the figures and with the analysis and results. I also provided useful feedback on the manuscript once it was written. This work is an excellent example of a scientific collaboration.

# Acknowledgements

First and foremost, I owe great thanks to my advisor, Professor Jules Carbotte. His interest in science is full of childish enthusiasm. I cannot count the number of times that I have walked into his office to hear him eager to explain something that he had figured out. He is a source of great inspiration.

I also owe thanks to my former supervisor, Professor Catherine Kallin. Her integrity and attitude toward science have helped to shape the way I think about the world.

I have had an enjoyable stay at McMaster. The faculty, staff and students have always been very supportive and helped to cultivate a positive environment. Special thanks go out to Allan Bayntun, my physics-partner-in-crime. He was always willing to chat about physics, even when the rest of our friends were eye-rolling hard. The amount of times I walked into his office to ask a stupid question about something is nearly innumerable. I'd also like to the rest of my Hamiltonian friends who helped keep me sane. In particular Clare, Patrick, Claire, Josh, Mike, Allan, Sandy, Laura, Andreas, Brendan, Blair, Mark, and Annie. You guys are great.

Finally, I owe deep gratitude to my parents, for raising me to be a person who can be interested in anything around him. They never once gave me a short answer when I was an annoying little kid who kept asking 'why?'. I am very grateful.

*Tiger got to hunt,  
Bird got to fly;  
Man got to sit and wonder, "Why, why why?"  
Tiger got to sleep,  
Bird got to land;  
Man got to tell himself he understand.  
—Kurt Vonnegut, *Cat's Cradle**

# List of Figures

3.1	Crystal structure of graphene . . . . .	16
3.2	Band structure of graphene . . . . .	18
3.3	Optical conductivity of graphene . . . . .	20
4.1	$s$ and $d$ -wave superconducting gaps . . . . .	38
4.2	Cuprate phase diagram . . . . .	40
5.1	Hall conductivity . . . . .	62
5.2	Types of low energy Weyl spectra. . . . .	63



# Contents

<b>1</b>	<b>Introduction</b>	<b>5</b>
<b>2</b>	<b>Preliminaries</b>	<b>9</b>
2.1	Where to find Dirac Fermions . . . . .	10
2.2	The Kubo formula for the optical conductivity . . . . .	11
<b>3</b>	<b>Graphene</b>	<b>15</b>
3.1	Optical conductivity . . . . .	20
3.2	Paper I – Tracking quasiparticle energies in graphene with near-field optics . . . . .	22
3.3	Paper II – Impact of electron-phonon coupling on near-field optical spectra in graphene . . . . .	31
<b>4</b>	<b>The High <math>T_c</math> cuprate superconductors</b>	<b>37</b>
4.1	The high- $T_c$ cuprate superconductors . . . . .	39
4.2	Dirac quasiparticles . . . . .	41
4.3	YRZ Green’s function . . . . .	42
4.4	Luttinger’s theorem . . . . .	44
4.5	Paper III – Resonating valence bonds and Fermi surface reconstruction: Resistivity in the underdoped cuprates . . . . .	46
4.6	Paper IV – c-axis optical conductivity from the Yang-Rice-Zhang model of the underdoped cuprates . . . . .	51

<b>5</b>	<b>Weyl Semimetals</b>	<b>61</b>
5.1	Paper V – Magneto-optical conductivity of Weyl semimetals . . . . .	66
<b>6</b>	<b>Conclusions</b>	<b>73</b>

# Chapter 1

## Introduction

*I think it is a peculiarity of myself that I like to play about with equations, just looking for beautiful mathematical relations which maybe dont have any physical meaning at all. Sometimes they do.”*

– P. A. M. Dirac

Broadly speaking, condensed matter physics is the study of the physical properties of the different phases of matter. In school we are taught about the phases of matter: solids, liquids and gases. Condensed matter physicists focus on the possible states of solids and liquids. In particular, they focus on how electrons behave in these materials. Different solids and liquids are universes with different laws for electrons. These different universes are called the phases of matter.

Superconductivity is one such universe. Metals and insulators represent other distinct universes. To classify these different phases we rely on the measurement of different average properties of the system. For example, metals, insulators and superconductors all have very different AC conductivities.

One might attempt to classify all the states of matter starting from the Hamiltonian for electrons and the underlying lattice

$$\mathcal{H} = \sum_i \frac{p_i^2}{2m} + \sum_i \frac{P_i^2}{2M} + \sum_{i<j} \frac{e^2}{|r_i - r_j|} + \sum_{i<j} \frac{Z^2 e^2}{|R_i - R_j|} - \sum_{i,j} \frac{Ze^2}{|r_i - R_j|}, \quad (1.1)$$

where  $e$  is the electron charge,  $Z$  is the atomic number of the ions;  $p$  ( $P$ ),  $m$  ( $M$ ), and

$r$  ( $R$ ) are the momentum, mass, and position of the electrons (ions), respectively.

The Hamiltonian and appropriate initial conditions, combined with the Schrodinger equation for the many body wavefunction,

$$i\frac{\partial\psi}{\partial t} = \mathcal{H}\psi, \quad (1.2)$$

specifies the quantum state of the system at all times. The solution of this equation for any realistic system, involves an enormous number of degrees of freedom. In addition to the problem with the large number of degrees of freedom is that involved with the range of scales. Typical electronic energies are of the order  $\approx 1eV$ . The phase transition for conventional superconductors onsets at  $\approx 10^{-4}eV$ . This means we would be required to solve the problem over several orders of magnitude in energy; not a simple task! Even if the solution of Equation 1.2 was possible, the structure of the wavefunction would be so complicated that it would be difficult to extract meaningful information.

Fortunately it is not necessary to deal with all these complications. This is because many physical observables are related to average properties of the system. It is because of this that we can often deal with effective models. These models attempt to capture the essential physics of the problem, often using a much smaller set of degrees of freedom.

In this thesis we will explore the optical properties of a few different condensed matter systems. Questions like: ‘why are metals shiny?’, ‘why are clouds white?’, and ‘why is the sky blue?’ all involve the interaction of light with matter. Thus it is very natural to think about the optical response of different materials. We will compute the optical response of several different materials. In particular we consider the finite frequency optical response. It is useful for studying the properties of the metal insulator transition, for example.

All of the materials that we will examine in this thesis share the fact that their low energy excitations are ‘Dirac-like’. That is, they have a dispersion relation that is linear with momentum. This type of dispersion used to be viewed as quite unusual, but is now ubiquitous in condensed matter physics. In this thesis we will look at

graphene, the High- $T_c$  cuprate superconductors, and Weyl semi-metals as examples of materials with Dirac dispersions. Dirac dispersions are also of interest in the new field of topological insulators, whose surface states have a Dirac structure.

In **Chapter 2** we will discuss how Dirac Fermions can appear naturally in condensed matter systems, as well as introducing some standard formalism for the optical conductivity.

**Chapter 3** contains two papers on a new spectroscopic technique, near-field optics, as applied to graphene.

**Chapter 4** features two papers where we study the optical properties of the underdoped cuprates by employing a phenomenological model developed by Yang, Rice and Zhang.

In **Chapter 5** we present one paper where we study the magneto-optical response of a new class of materials, known as Weyl semimetals.

In **Chapter 6** we conclude and talk about possible future directions.



## Preliminaries

The now famous Dirac equation is a great triumph of theoretical physics. It was the first equation to unify the theory of special relativity with quantum mechanics. Dirac wrote his equation in the form [1]

$$i\hbar\frac{\partial\Psi}{\partial t} = (c\boldsymbol{\alpha}\cdot\mathbf{p} + \beta mc^2)\Psi, \quad (2.1)$$

where  $\boldsymbol{\alpha}$  and  $\beta$  were  $4 \times 4$  matrices,  $m$  is the particle's mass,  $c$  is the speed of light, and  $\Psi$  is a 4-component wavefunction, known as a spinor. This multiple component wavefunction gave a natural explanation for Pauli's theory of electron spin. Before this time, the 2-component nature required to explain spin was purely phenomenological. The Dirac equation also led to the prediction of the positron, which was discovered a few years later [2].

When the particles are massless the Dirac equation can be simplified [3]. The  $\boldsymbol{\alpha}$  matrices are all block diagonal, while  $\beta$  is block off-diagonal. So, when  $m = 0$  the 4-component spinor can be split into two parts,  $\psi_L$  and  $\psi_R$ . They satisfy the equation

$$i\hbar\frac{\partial\psi_{R,L}}{\partial t} = \pm c\boldsymbol{\sigma}\cdot\mathbf{p}\psi_{R,L}, \quad (2.2)$$

where  $\boldsymbol{\sigma}$  is the vector of Pauli matrices. This equation is known as the Weyl equation, and  $\psi_L$  and  $\psi_R$  are Weyl Fermions.

## 2.1 Where to find Dirac Fermions

In condensed matter physics, the time evolution of a state is given not by the Dirac equation, but by the Schrodinger equation

$$i\frac{\partial\psi}{\partial t} = \mathcal{H}\psi. \quad (2.3)$$

When  $\mathcal{H}$  is a non-relativistic Hamiltonian, how can we expect to get a Dirac equation? The relativistic form for the energy might be acquired if two bands cross. Accidental band touchings have been studied since the early days of the theory of solids. They were first studied by Herring [4, 5] in 1937. In 1968 Halperin and Rice [6] visited the problem of a quadratic band touching. They showed that this problem was unstable to the formation of bound states of electrons and holes, that is it was unstable to the formation of an excitonic insulating state. There is no reason that bands should touch quadratically. One would assume that a generic band touching should occur linearly, unless there was some symmetry present to forbid it. In 1971 Abrikosov [7, 8] studied the problem of a linear band touching and showed that it was stable. In such a way one can get a Dirac like Hamiltonian in a condensed matter system.

For a non-interacting system (or one where interactions can be effectively mapped onto a non-interacting system, like a Fermi liquid) Bloch's theorem [9] tells us that the wavefunctions  $|\psi_n(\mathbf{k})\rangle$  and the energy eigenvalues,  $E_n(\mathbf{k})$ , are labeled by a band quantum number,  $n$  as well as a continuous quantum number  $\mathbf{k}$ , the crystal momentum. If one considers two such bands,  $E_1(\mathbf{k})$  and  $E_2(\mathbf{k})$ , such that in some region of the Brillouin zone  $|E_1(\mathbf{k}) - E_2(\mathbf{k})| \ll |E_1(\mathbf{k}) - E_n(\mathbf{k})|$  for all other bands  $n$ , then we may write an effective Hamiltonian for the system by expanding in the Bloch states

$$\mathcal{H}_{eff} = \begin{pmatrix} \langle\psi_1(\mathbf{k})|\mathcal{H}|\psi_1(\mathbf{k})\rangle & \langle\psi_1(\mathbf{k})|\mathcal{H}|\psi_2(\mathbf{k})\rangle \\ \langle\psi_2(\mathbf{k})|\mathcal{H}|\psi_1(\mathbf{k})\rangle & \langle\psi_2(\mathbf{k})|\mathcal{H}|\psi_2(\mathbf{k})\rangle \end{pmatrix}. \quad (2.4)$$

We may write this Hamiltonian in terms of the Pauli matrices and the  $2 \times 2$  identity

matrix

$$\mathcal{H}_{eff} = g_0(\mathbf{k})\mathbb{I} + \sum_{i=1}^3 g_i(\mathbf{k})\sigma_i \quad (2.5)$$

for some functions  $g_i(\mathbf{k})$ .

For there to be a band touching it is sufficient to satisfy the condition that  $g_1(\mathbf{k}) = g_2(\mathbf{k}) = g_3(\mathbf{k}) = 0$ . This leads to a very interesting result. In 3-dimensions there are 3 independent components of the crystal momentum that can be varied. So in 3-dimensions there are three variables and three unknowns, and so the implicit function theorem tells us that we can have accidental band touchings in 3-dimensions. However, in 2-dimensions there are only two components of the crystal momentum that can be varied. In general band touchings will not happen for dimension less than three! This problem can be circumvented if there are additional symmetries that constrain equations between the  $g$ 's.

## 2.2 The Kubo formula for the optical conductivity

Here we will show the essentials required to arrive at our standard formulas for the conductivity. For more details on the Kubo formula see a standard many body theory book like Mahan [10] or Altland and Simons [11]. To study the optical conductivity we generally want to know how a material responds to an applied electric field. The incident electric field has the form

$$\mathbf{E}(\mathbf{r}, t) = \mathbf{E}_0 e^{i\mathbf{q}\cdot\mathbf{r} - i\omega t}. \quad (2.6)$$

Within linear response the conductivity is found from the relation

$$J_\alpha(\mathbf{r}, t) = \sigma_{\alpha\beta}(\mathbf{q}, \omega) E_\beta(\mathbf{r}, t). \quad (2.7)$$

To derive a formula for the conductivity one usually starts with a minimally coupled Hamiltonian (working in the gauge  $\nabla \cdot \mathbf{A} = 0$ , and in units where  $c = 1$ )

$$H = \int d^d r \left[ \frac{1}{2m} \psi^\dagger(x) (\mathbf{p} - e\mathbf{A})^2 \psi(x) - e\phi(x) \psi^\dagger(x) \psi(x) \right] + H_{int}. \quad (2.8)$$

The current is found in the usual way

$$\mathbf{j} = -\frac{\delta H}{\delta \mathbf{A}} \quad (2.9)$$

$$= \frac{-ie\hbar}{2m} (\psi^\dagger(x) \nabla \psi(x) - \psi(x) \nabla \psi^\dagger(x)) - \frac{e^2}{m} \mathbf{A} \psi^\dagger(x) \psi(x). \quad (2.10)$$

The first term is known as the paramagnetic current,  $j_p$  and the second term is known as the diamagnetic current  $j_d$ . In some of the literature the diamagnetic term is mistakenly forgotten. While calculating the real part of the conductivity within the Drude approximation, this term does not make a contribution. The diamagnetic terms should be kept so that the conductivity has the correct behaviour at  $\omega = 0$  and so that the conductivity obeys the Kramers-Kronig relations.

The observed current will be the expectation value of the current operator

$$J(\mathbf{r}, t) = \langle \mathbf{j}_p(\mathbf{r}, t) \rangle - \frac{ne^2}{m} \mathbf{A}(\mathbf{r}, t), \quad (2.11)$$

where  $n$  is the electron density. From linear response we know that since the coupling of the paramagnetic current to the vector potential is of the form

$$- \int d^d r \mathbf{j} \cdot \mathbf{A} \quad (2.12)$$

that

$$\langle j_{p\alpha}(\mathbf{r}, t) \rangle = i \int_{t' < t} d^d r' dt' \left\langle \left[ j_{p\alpha}(\mathbf{r}, t), j_{p\beta}(\mathbf{r}', t') \right] \right\rangle \quad (2.13)$$

Then remembering that  $\mathbf{E} = -\frac{\partial \mathbf{A}}{\partial t}$  we obtain the famous formula for the conductivity

$$\sigma_{\alpha\beta}(\mathbf{q}, \omega) = \frac{ine^2}{m(\omega + i0^+)} \delta_{\alpha\beta} + \frac{1}{\omega + i0^+} \int_0^\infty dt e^{i(\omega + i0^+)t} \langle [j_\alpha(-\mathbf{q}, t), j_\beta(\mathbf{q}, 0)] \rangle \quad (2.14)$$

This result is often recast in terms of the retarded current-current correlation function:

$$\Pi_{\alpha\beta}(\mathbf{q}, \omega) = -i \int dt \theta(t - t') e^{i\omega(t-t')} \langle [j_\alpha(-\mathbf{q}, t), j_\beta(\mathbf{q}, t')] \rangle. \quad (2.15)$$

This gives

$$\sigma_{\alpha\beta}(\mathbf{q}, \omega) = \frac{i}{(\omega + i0^+)} \left[ \Pi_{\alpha\beta}(\mathbf{q}, \omega) + \frac{ne^2}{m} \delta_{\alpha\beta} \right]. \quad (2.16)$$

The advantage of this form is that we can use the well established Green's function formalism for computing the current current correlation function. We are also usually interested in the real part of the conductivity, as this corresponds to optical absorption. The imaginary part can easily be obtained from the real part using a Kramers-Kronig relation, if desired. The real part is given by

$$\text{Re}[\sigma_{\alpha\beta}(\mathbf{q}, \omega)] = -\frac{1}{\omega} \text{Im}[\Pi_{\alpha\beta}(\mathbf{q}, \omega)]. \quad (2.17)$$

At the one loop level the current-current correlator is given by

$$\Pi_{\alpha\beta}(\mathbf{q}, \omega) = e^2 T \sum_{\mathbf{k}, \nu_n} [v_\alpha(\mathbf{k}) G(\mathbf{k}, \nu_n) v_\beta(\mathbf{k} + \mathbf{q}) G(\mathbf{k} + \mathbf{q}, \omega + \nu_n)]. \quad (2.18)$$

Finally using the spectral representation for the Green's function

$$G(\mathbf{p}, z) = \int \frac{d\omega}{2\pi} \frac{A(\mathbf{p}, \omega)}{z - \omega}, \quad (2.19)$$

one can cast the problem in terms of the spectral functions,  $A(\mathbf{p}, \omega)$ . The advantage of this form comes when treating a problem where particles have a finite lifetime. There are many Kubo formulas in the literature that involve matrix elements of current operators divided by energy denominators. The form in terms of spectral functions

reduces to these when  $A(\mathbf{k}, \omega) = 2\pi\delta(\omega - \epsilon_{\mathbf{k}})$ , that is, for non-interacting particles. In the presence of interactions described by a self energy  $\Sigma(\mathbf{k}, \omega)$  they take the form

$$A(\mathbf{k}, \omega) = \frac{1}{\pi} \frac{|\text{Im}\Sigma(\mathbf{k}, \omega)|}{(\omega - \text{Re}\Sigma(\mathbf{k}, \omega) - \epsilon_{\mathbf{k}})^2 + |\text{Im}\Sigma(\mathbf{k}, \omega)|^2}, \quad (2.20)$$

and the expression in terms of spectral functions is more useful.

# Graphene

Graphene is a single layer of carbon atoms arranged in a honeycomb lattice. It was first studied in 1947 by Wallace [12], who was attempting to calculate the band structure of graphite. The three-dimensional graphite calculation was too difficult, and so he ended up studying the simpler two-dimensional version. Graphene can be thought of as the building block of other forms of carbon. By rolling it up into balls, one obtains fullerenes, rolling it up along one direction produces cylinders known as carbon nanotubes, and stacking many layers together gives graphite.

The Mermin-Wagner theorem [13, 14] forbids the breaking of a continuous symmetry for systems with dimension 2 or less. Thus, for a long time Wallace's calculation remained a theoretical curiosity. It was thought that graphene would be unstable, and form a different allotrope of carbon. This changed in 2004 when graphene was isolated by Geim and Novoselov [15] using mechanical ex-foliation (the 'scotch tape method'). Graphene overcomes the assumptions of the Mermin-Wagner theorem since it is free to ripple in the plane, or is often mounted on a substrate. The observation of graphene was first confirmed by an optical interference experiment on silicon dioxide wafers.

The relativistic band structure in graphene stirred up a great deal of interest once it was successfully isolated. It opened the door to the possibility of studying relativistic quantum mechanics in table-top experiments. One relativistic effect is Klein tunneling [16]. Klein tunneling is the ability for the electron waves to penetrate large

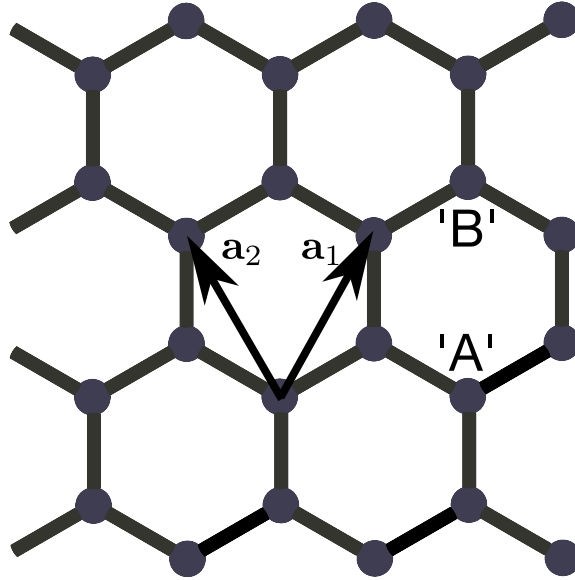


Figure 3.1: Graphene naturally forms a honeycomb lattice. The set of basis vectors,  $\mathbf{a}_1$  and  $\mathbf{a}_2$  is shown. The two inequivalent points A and B are also labeled. Notice that A and B have different nearest neighbor vectors.

potential barriers. The chirality of the electronic wavefunctions in graphene suppresses backscattering, leading to the Klein effect. Thus the electrons near the Dirac points can move through disorder unhindered, leading to high carrier mobility. In graphene  $v_F \approx 10^6$  plays the role of the speed of light. Hence graphene is like a universe with a slower speed of light. This leads to a different value for the fine structure constant. For electrons in QED the fine structure constant is  $\alpha_{QED} = e^2/(\hbar c) \approx 1/137$ . In graphene  $\alpha_{\text{graphene}} = e^2/(\hbar v_F) \approx 2.2$ . This could lead to the possibility of studying possible strong coupling effects in graphene.

The crystal structure of graphene is shown in Figure 3.1. Graphene is a simple example of a Bravais lattice with a 2 point basis. There are two chemically equivalent, but topologically inequivalent sites often referred to as A and B, that make up the lattice. The honeycomb network of carbon atoms is formed from  $sp^2$  hybridized bonds. The conduction electrons reside in an additional  $p$  orbital that sticks out of the plane. The hopping of electrons between these orbitals can be most simply treated within a tight binding formalism.

The lattice vectors can be written

$$\mathbf{a}_1 = \frac{a}{2} (1, \sqrt{3}), \mathbf{a}_2 = \frac{a}{2} (-1, \sqrt{3}), \quad (3.1)$$

where  $a = \sqrt{3}a_0$ , with  $a_0$  the carbon-carbon distance.

The tight-binding Hamiltonian for nearest neighbor hopping has the form

$$H = -t \sum_{\langle i,j \rangle, \sigma} \left( a_{i,\sigma}^\dagger b_{j,\sigma} + \text{H.c.} \right). \quad (3.2)$$

Here  $t$  is a hopping integral, and  $a_{i,\sigma}$  ( $a_{i,\sigma}^\dagger$ ) annihilates (creates) an electron with spin  $\sigma$  on site  $\mathbf{r}_i$  of sublattice A (likewise for the B sublattice).

This Hamiltonian is a set of  $2 \times 2$  matrices in momentum space with eigenvalues

$$E(\mathbf{k}) = \pm t \sqrt{|f(\mathbf{k})|^2}, \quad (3.3)$$

where  $f(\mathbf{k}) = 1 + e^{i\mathbf{k}\cdot\mathbf{a}_1} + e^{i\mathbf{k}\cdot\mathbf{a}_2}$  is the matrix element after evaluating the sum over nearest neighbors. Some simple algebra leads to

$$E(\mathbf{k}) = \pm t \sqrt{3 + 4 \cos\left(\frac{k_x a}{2}\right) \cos\left(\frac{k_y \sqrt{3} a}{2}\right) + 2 \cos(k_x a)}. \quad (3.4)$$

The resulting band structure is shown in Figure 3.2. We can see that there are two bands, as expected for a Bravais lattice with a two point basis. These bands touch at isolated points in the Brillouin zone. Solving  $E(\mathbf{k}) = 0$  we find that the band touchings happen at two distinct points, called  $K$  and  $K'$ . They are given by

$$K = \left( \frac{4\pi}{3a}, 0 \right), K' = \left( \frac{2\pi}{3a}, \frac{2\pi}{\sqrt{3}a} \right). \quad (3.5)$$

The low energy physics will be dominated by these points. To make their Dirac like nature explicit we can expand around the  $K$  (or  $K'$ ) point. Writing  $\mathbf{k} = K + \mathbf{q}$  the Hamiltonian takes the form

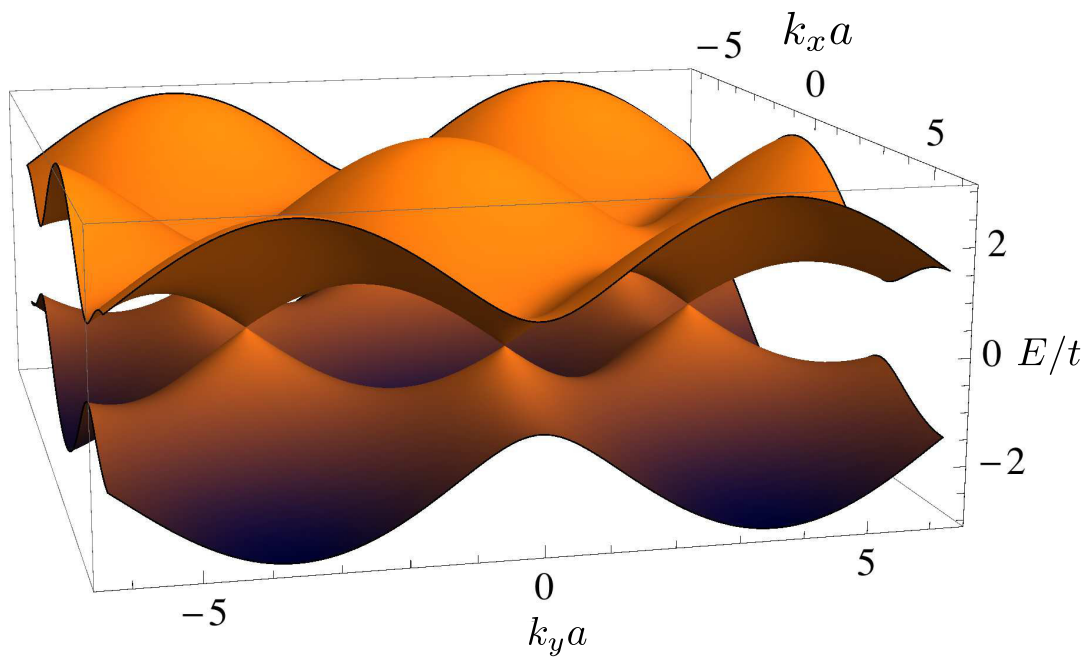


Figure 3.2: The band structure of graphene in the tight binding model. Notice the isolated points in the Brillouin zone where the conduction and valence bands touch. It is around these points that the dispersion has a Dirac like structure. These points dominate the low energy physics.

$$H = \frac{\sqrt{3}at}{2} \begin{pmatrix} 0 & q_x - iq_y \\ q_x + iq_y & 0 \end{pmatrix}. \quad (3.6)$$

With the identification  $v_F = \frac{\sqrt{3}at}{2}$ , we have  $H = v_F \boldsymbol{\sigma} \cdot \mathbf{k}$ , where  $\boldsymbol{\sigma}$  is the vector of Pauli matrices. In this form it becomes obvious that the low energy Hamiltonian takes the same form as the equation for massless Dirac Fermions. Interestingly, the velocity is also independent of energy. This is in stark contrast to usual Schrodinger particles where  $v \propto \sqrt{E}$ .

The wavefunctions around the point  $K$  can be found by solving the eigenvalue problem

$$-iv_F \boldsymbol{\sigma} \cdot \nabla \psi = E \psi. \quad (3.7)$$

In momentum space we have

$$\psi_{\pm}(\mathbf{q}) = \frac{1}{\sqrt{2}} \begin{pmatrix} e^{-i\theta_{\mathbf{q}}/2} \\ \pm e^{i\theta_{\mathbf{q}}/2} \end{pmatrix}, \quad (3.8)$$

where the  $\pm$  labels the band index given by the Energy  $E = \pm v_F q$ , and  $\theta_{\mathbf{q}} = \arctan\left(\frac{q_y}{q_x}\right)$ . Defining the variables  $\theta_{\mathbf{q}\mathbf{q}'} = \theta_{\mathbf{q}} - \theta_{\mathbf{q}'}$  and  $s = \pm 1$ , the wavefunction overlap is given by

$$F_{ss'}(\theta_{\mathbf{q}\mathbf{q}'})) = \psi_{s'}^{\dagger}(\mathbf{q}') \psi_s(\mathbf{q}) = \frac{1}{2} [1 + ss' \cos(\theta_{\mathbf{q}\mathbf{q}'})]. \quad (3.9)$$

The wavefunction overlap encodes information about the allowed scattering processes in graphene. Specifically, the angular dependence suppresses backscattering. This is a reflection of the fact that the low energy quasiparticles in graphene are chiral. This wavefunction overlap naturally arises in the formula for the conductivity since it involves both inter- and intra-band processes.

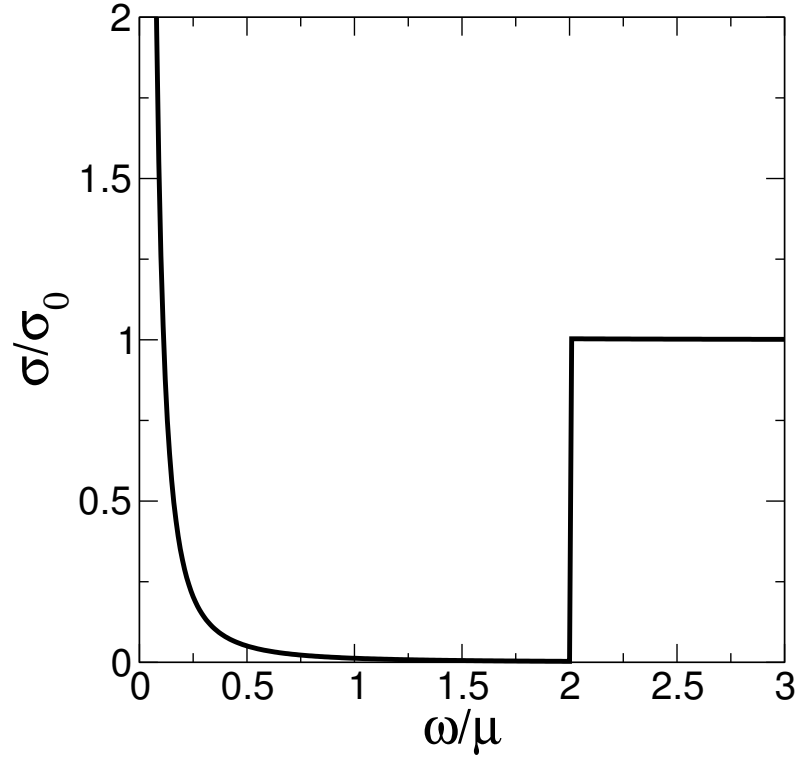


Figure 3.3: The  $q = 0$  limit of the optical conductivity of graphene is shown. Note that the delta function was broadened according to  $\delta(z) \rightarrow \frac{1}{\pi} \frac{\epsilon}{\epsilon^2 + z^2}$  with  $\epsilon = 0.01$  for graphing purposes. This figure can be compared to the finite  $q$  graphs shown in the manuscripts.

### 3.1 Optical conductivity

For comparison to the finite  $q$  conductivity presented in the papers that follow, I include the expression for the conductivity in the  $q = 0$  case. It is shown in Figure 3.3. There is an intraband piece corresponding to the free charge carriers, and an interband piece at higher energies. The gap between the inter and intra band pieces is due to the Pauli exclusion principle.

After extracting the spectral functions from the graphene Green's function and substituting them into the Kubo formula, the conductivity is given by

$$\begin{aligned} \frac{\sigma_{xx}(\omega)}{\sigma_0} &= \frac{4}{\omega} \int_{\mu-\omega}^{\mu} d\omega' \int \epsilon d\epsilon [\delta(\omega' + \omega - \epsilon)\delta(\omega' - \epsilon) + \delta(\omega' + \omega + \epsilon)\delta(\omega' + \epsilon) \\ &\quad + \delta(\omega' + \omega + \epsilon)\delta(\omega' - \epsilon) + \delta(\omega' + \omega - \epsilon)\delta(\omega' + \epsilon)], \end{aligned} \quad (3.10)$$

where  $\sigma_0 = e^2/4$  and  $\mu$  is the chemical potential. The first two terms are the intraband terms and the second two are the interband terms. Looking at the intraband terms and doing the energy integral gives

$$\frac{4}{\omega} \int_{\mu-\omega}^{\mu} d\omega' |\omega'| \delta(\omega) \quad (3.11)$$

$$= \frac{4}{\omega} \delta(\omega) \left( \mu\omega - \frac{\omega^2}{2} \right) \quad (3.12)$$

$$= 4\mu\delta(\omega). \quad (3.13)$$

For the interband terms doing the energy integral leaves

$$\frac{4}{\omega} \int_{\mu-\omega}^{\mu} d\omega' |\omega'| \delta(2\omega' + \omega) \quad (3.14)$$

$$= \theta(\omega - \mu - \omega/2) - \theta(-\omega/2 - \mu) \quad (3.15)$$

$$= \theta(\omega - 2\mu). \quad (3.16)$$

So we arrive at the result

$$\frac{\sigma_{xx}(\omega)}{\sigma_0} = 4\mu\delta(\omega) + \theta(\omega - 2\mu). \quad (3.17)$$

## 3.2 Paper I – Tracking quasiparticle energies in graphene with near-field optics

Reprinted with permission as follows: Phillip E.C. Ashby and J.P. Carbotte “*Tracking quasiparticle energies in graphene with near-field optics*” Phys. Rev. B **86** 165405 (2012). Copyright (2012) by the American Physical Society.

Near field optics is a new technique developed for probing the finite wavevector response in various materials. The technique uses an atomic force microscope tip as an antennae for the incident radiation. The sharp tip effectively acts as an antennae that provides a finite wavevector for the radiation. In particular, graphene was being studied using this technique. In this paper we study the optical response of graphene at finite momentum transfer. In particular we focused in on the properties of the quasiparticle peak. We studied the optical conductivity at finite temperatures, and were able to derive a formula for the finite wavevector conductivity in the presence of residual scattering.

PHYSICAL REVIEW B **86**, 165405 (2012)**Tracking quasiparticle energies in graphene with near-field optics**

Phillip E. C. Ashby\*

*Department of Physics and Astronomy, McMaster University, Hamilton, Ontario, Canada L8S 4M1*

J. P. Carbotte†

*Department of Physics and Astronomy, McMaster University, Hamilton, Ontario, Canada L8S 4M1 and  
The Canadian Institute for Advanced Research, Toronto, Ontario, Canada M5G 1Z8*

(Received 13 August 2012; published 2 October 2012)

Advances in infrared nanoscopy have enabled access to the finite momentum optical conductivity  $\sigma(\mathbf{q}, \omega)$ . The finite momentum optical conductivity in graphene has a peak at the Dirac fermion quasiparticle energy  $\epsilon(k_F - q)$ , i.e., at the Fermi momentum minus the incident photon momentum. We find that the peak remains robust even at finite temperature as well as with residual scattering. It can be used to trace out the fermion dispersion curves. However, this effect depends strongly on the linearity of the Dirac dispersion. Should the Dirac fermions acquire a mass, the peak in  $\sigma(q, \omega)$  shifts to lower energies and broadens as optical spectral weight is redistributed over an energy range of the order of the mass gap energy. Even in this case structures remain in the conductivity, which can be used to describe the excitation spectrum. By contrast, in graphene strained along the armchair direction, the peak remains intact but shifts to a lower value of  $q$  determined by the anisotropy induced by the deformation.

DOI: [10.1103/PhysRevB.86.165405](https://doi.org/10.1103/PhysRevB.86.165405)

PACS number(s): 78.67.Wj, 72.80.Vp, 81.05.ue

**I. INTRODUCTION**

Graphene, first isolated in 2004,<sup>1</sup> has been the host of a variety of novel electronic properties. The main difference in graphene is its unique energy dispersion. The charge carriers in graphene are massless Dirac fermions, which accounts for the differences from the conventional 2D electron gas. Remarkable behavior has already been reported in the plasmon dispersion relation,<sup>2-5</sup> as well as the optical conductivity,<sup>6-8</sup> which supports a transverse electromagnetic mode.<sup>9</sup> There is also recent evidence for plasmarons,<sup>10,11</sup> a new type of quasiparticle formed by the interaction of charge carriers with plasmons. Optical spectroscopy is a useful tool for obtaining information about the dynamics of charge carriers and has been used to great success in graphene.<sup>12</sup>

The real part of the  $q \rightarrow 0$  optical conductivity in graphene is well known. At finite chemical potential,  $\mu$ , it contains a Drude peak at  $\omega = 0$  due to intraband absorption, followed by a Pauli-blocked region. There is then a sharp rise at  $\omega = 2\mu$  to a universal background conductivity  $\sigma_0 = e^2/4$ ,<sup>7,13-15</sup> due to interband transitions. Experimentally, the region that should be Pauli-blocked and have no absorption does not fall below about  $\sigma_0/3$ .<sup>16</sup> Electron-electron interactions, electron-phonon interactions, and impurity scattering can all provide contributions to the optical conductivity in this region, but nothing as large as the observed value.<sup>17-20</sup> The origin of this anomalously large background is still a mystery.

More recent experiments have granted access to the finite momentum transfer optical conductivity  $\sigma(\mathbf{q}, \omega)$ .<sup>21-23</sup> In the paper by Fei *et al.*,<sup>21</sup> they describe how an atomic force microscope (AFM) operating in tapping mode allows one to obtain information about the finite  $q$  conductivity. The incident light scatters off the tip and is confined to a nanoscale region. The precise details depend on the geometry of the tip, and Fei *et al.* report a distribution of  $q$  values with a peak at  $q \approx 3.4 \times 10^5 \text{ cm}^{-1}$ . In principle, a sharper tip would lead to higher confinement, and thus larger values of  $q$  could be accessible through adjustments to the AFM tip.

In this paper we study the properties of the quasiparticle peak at  $\omega = q$  in the real part of the optical conductivity. In Sec. II we discuss the properties of this peak and its relationship to the joint density of states at  $T = 0$  as well as at finite temperatures. We find that the quasiparticle peak remains robust even at large temperatures. In Sec. III we consider the presence of residual scattering and provide a simple analytical formula for the quasiparticle peak. Again, the peak position remains robust, even for large impurity concentration. We finally consider two methods of altering the Dirac dispersion in Sec. IV, gapped and strained graphene. We find that these modifications do alter the position of the quasiparticle peak and, so, the linearity and isotropy are crucial for its robustness.

**II. FORMALISM AND EXPRESSIONS FOR THE CONDUCTIVITY**

The  $xx$  component of the real part of the finite temperature optical conductivity is given by

$$\frac{\sigma_{xx}(\mathbf{q}, \omega)}{\sigma_0} = \frac{8}{\omega} \int [f(\omega') - f(\omega' + \omega)] d\omega' \int \frac{d^2\mathbf{k}}{2\pi} \times \sum_{s,s'} F_{ss'}(\phi) A^s(\mathbf{k}, \omega') A^{s'}(\mathbf{k} + \mathbf{q}, \omega' + \omega). \quad (1)$$

In the above,  $\sigma_0 = e^2/4$  is the universal background conductivity,  $F_{ss'}(\phi)$  are the coherence (or chirality) factors,  $f(\omega) = 1/(e^{\beta\omega} + 1)$  is the Fermi-Dirac distribution function, and  $A^s(\mathbf{k}, \omega)$  is the spectral density. We chose our  $x$  direction along the zig-zag axis (see Fig. 1). From here on we use  $\sigma(\mathbf{q}, \omega)$  to denote  $\sigma_{xx}(\mathbf{q}, \omega)$ . We work in units where  $\hbar = v_F = 1$ .

The spectral densities,  $A^s(\mathbf{k}, \omega)$ , reduce to Dirac delta functions in the bare-band case. In the presence of interactions described by a self energy  $\Sigma_s(\mathbf{k}, \omega)$ , they are given by

$$A^s(\mathbf{k}, \omega) = \frac{1}{\pi} \frac{|\text{Im}\Sigma_s(\mathbf{k}, \omega)|}{[\omega - \text{Re}\Sigma_s(\mathbf{k}, \omega) - \epsilon_{\mathbf{k}}^s]^2 + |\text{Im}\Sigma_s(\mathbf{k}, \omega)|^2}, \quad (2)$$

where  $\epsilon_{\mathbf{k}}^s = sk - \mu$ .

The peaks in the spectral density control the shape of the optical conductivity and correspond broadly to two types of processes: intraband and interband transitions. The intraband transitions occur at  $\omega = q$  and are the focus of this paper. Interband scattering is responsible for subsequent peaks in the spectral functions, which occur at  $\omega = 2\mu - q$  and  $\omega = 2\mu + q$ . We will first consider the bare-band case and examine the effect of impurity scattering in Sec. III.

### A. Results for bare bands, $T = 0$

Since the spectral functions are simply given by Dirac delta functions in the bare-band case, the physics is governed by the coherence factor  $F_{ss'}(\phi)$ , which encodes information about scattering. It is given by

$$F_{ss'}(\phi) = \frac{1}{2}(1 + ss' \cos \phi). \quad (3)$$

The angle  $\phi$  is defined in terms of the angles of  $\mathbf{k}$  and  $\mathbf{k} + \mathbf{q}$ , denoted by  $\theta_{\mathbf{k}}$  and  $\theta_{\mathbf{k}+\mathbf{q}}$ , respectively (Fig. 1). For the optical conductivity,  $\phi = \theta_{\mathbf{k}} + \theta_{\mathbf{k}+\mathbf{q}}$ . The longitudinal dielectric function is related to the density-density correlation function, often called the polarizability,  $\Pi$ . In comparison to the optical conductivity, the polarizability has  $\phi = \theta_{\mathbf{k}} - \theta_{\mathbf{k}+\mathbf{q}}$ .

We can write down an expression for  $F_{ss'}(\phi)$  in terms of the magnitudes of  $\mathbf{k}$  and  $\mathbf{q}$  and their angles with respect to the  $k_x$

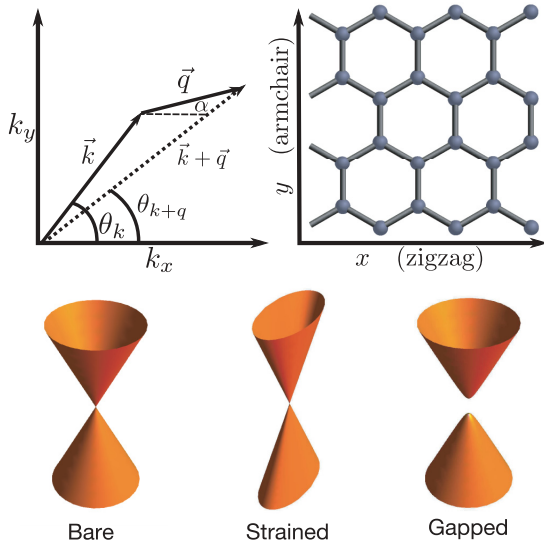


FIG. 1. (Color online) (Top) The scattering geometry in  $k$  space for the optical conductivity and polarizability. Both the optical conductivity and polarizability contain coherence factors  $F_{ss'}(\phi) = \frac{1}{2}(1 + ss' \cos \phi)$ . The important difference is that  $\phi = \theta_{\mathbf{k}} + \theta_{\mathbf{k}+\mathbf{q}}$  in the optical conductivity, while  $\phi = \theta_{\mathbf{k}} - \theta_{\mathbf{k}+\mathbf{q}}$  in the polarizability. We orient our axes so that  $x$  is along the so-called zigzag direction of graphene, while the  $y$  axis is along the armchair direction. (Bottom) Energy dispersions for bare, strained, and gapped graphene. The effect of strain distorts the Dirac cones from a circular to an elliptical cross section. Gapped graphene retains its circular shape, but the low-energy dispersion is now quadratic, and the Dirac point is no longer accessible.

axis,  $\theta$ , and  $\alpha$ , respectively (Fig. 1). We have

$$F_{ss'}(\phi) = \frac{1}{2} \left[ 1 + ss' \frac{k \cos(2\theta) + q \cos(\theta + \alpha)}{\sqrt{k^2 + q^2 + 2kq \cos(\theta - \alpha)}} \right], \quad (4)$$

for the optical conductivity, and

$$F_{ss'}(\phi) = \frac{1}{2} \left[ 1 + ss' \frac{k + q \cos(\theta - \alpha)}{\sqrt{k^2 + q^2 + 2kq \cos(\theta - \alpha)}} \right], \quad (5)$$

for the polarizability, which we include for comparison. Notice that the polarizability only involves the angle  $\theta - \alpha$ , while the optics contains  $\theta - \alpha$ ,  $\theta + \alpha$ , and  $2\theta$ . A consequence of this is that for the polarizability, the dependence on the direction of the photon momentum  $\mathbf{q}$  can be eliminated by a shift in the integration variable. For the optical conductivity, no simple change of variables exists, and  $F_{ss'}(\phi)$  remains dependent on the angle  $\mathbf{q}$  makes with respect to the  $k_x$  axis.

In an isotropic system only two directions need to be considered for  $\mathbf{q}$ :  $\mathbf{q}$  along  $k_x$  (longitudinal) and  $\mathbf{q}$  along  $k_y$  (transverse). This gives

$$F_{ss'}(\phi) = \frac{1}{2} \left[ 1 + ss' \frac{k \cos(2\theta) + q \cos(\theta)}{\sqrt{k^2 + q^2 + 2kq \cos(\theta)}} \right], \quad (6)$$

for the longitudinal part of  $\sigma_{xx}$ , and

$$F_{ss'}(\phi) = \frac{1}{2} \left[ 1 + ss' \frac{k \cos(2\theta) - q \sin(\theta)}{\sqrt{k^2 + q^2 + 2kq \sin(\theta)}} \right], \quad (7)$$

for its transverse part. The difference between Eqs. (6) and (7) has a drastic difference in the shape of  $\sigma(\mathbf{q}, \omega)$ , its longitudinal part diverges at  $\omega = q$ , while the transverse parts vanishes at  $\omega = q$  (Fig. 2).

To understand this difference in behavior, we introduce a reference function, the joint density of states (JDOS). It is

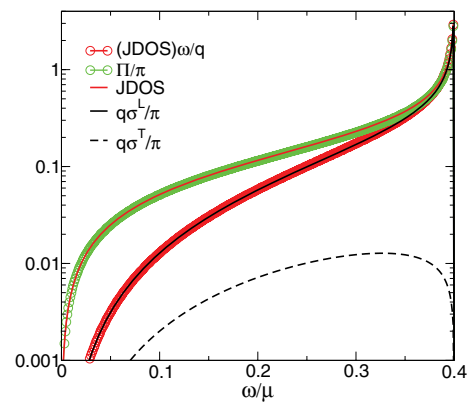


FIG. 2. (Color online) The real part of the longitudinal and transverse conductivity,  $\sigma^L$  and  $\sigma^T$ , for  $q = 0.4$  scaled by  $q/\pi$  as a function of  $\omega/\mu$ . JDOS and the polarizability  $\Pi$  as a function of  $\omega/\mu$ . The prefactors have been chosen to make the longitudinal conductivity and JDOS agree at  $\omega = q$ .

given by

$$\text{JDOS}(\mathbf{q}, \omega) = 4 \int \frac{d^2\mathbf{k}}{(2\pi)^2} [f(\epsilon_{\mathbf{k}}^s - \mu) - f(\epsilon_{\mathbf{k}+\mathbf{q}}^{s'})] \delta(\omega + \epsilon_{\mathbf{k}}^s - \epsilon_{\mathbf{k}+\mathbf{q}}^{s'}), \quad (8)$$

where the factor of 4 is from the degeneracy (spin and valley) in graphene. The JDOS for the intraband piece at  $T = 0$  is given by

$$\text{JDOS}(\mathbf{q}, \omega) = \frac{1}{4\pi^2 \sqrt{q^2 - w^2}} \left\{ \Theta(w - q + 2\mu) \left[ (2\mu + w) \sqrt{(2\mu + w)^2 - q^2} - (q^2 - 2w^2) \ln \frac{\sqrt{(2\mu + w)^2 - q^2} + (2\mu + w)}{q} \right] \right. \\ \left. - \Theta(2\mu - q - w) \left[ (2\mu - w) \sqrt{(2\mu - w)^2 - q^2} - (q^2 - 2w^2) \ln \frac{\sqrt{(2\mu - w)^2 - q^2} + (2\mu - w)}{q} \right] \right\}. \quad (9)$$

The longitudinal and transverse conductivity differ from the joint density of states by the coherence factors, as mentioned above. Both the joint density of states and the conductivity contain the same delta function. Evaluating the coherence factors Eqs. (6) and (7) at  $\omega = q$  subject to the delta function constraint shows that  $F_{++} = 1$  and 0, respectively. This explains the fact that the longitudinal conductivity has a square root singularity (inherited from the JDOS), while the transverse conductivity is zero.

A physical picture for this difference is as follows. We consider a possible optical transition with momentum transfer  $q$  and energy  $\omega = q$  from an occupied state below the chemical potential, to an empty state above the chemical potential. We will consider the momentum of the final state to determine the contribution to the conductivity. For the longitudinal case, that is,  $q$  taken along the  $k_x$  direction, the final state momentum is the sum of the magnitude of the initial momentum  $k$  and the photon momentum  $q$  and results in a maximum momentum along  $k_x$ . For the transverse case, the initial  $\mathbf{k}$  must also be transverse to be an allowed transition (recall  $\omega = q$ ). The resulting state has no momentum along the  $k_x$  direction, and so the transverse conductivity vanishes.

The joint density of states, Eq. (9), bares a strong resemblance to both the polarizability  $\Pi$  and the longitudinal conductivity, which have been computed previously.<sup>2,4,5,24</sup> The conductivity, polarizability, and joint density of states are all shown in Fig. 2. The factor  $q/\pi$  multiplying the conductivity was chosen to make the functions agree at  $\omega = q$ , and the factor  $1/\pi$  multiplying the polarizability was

chosen to make the polarizability have the same prefactor as the JDOS.

The agreement between the joint density of states and the polarizability is excellent (Fig. 2). In fact, the difference is given by

$$\text{JDOS} - \frac{1}{\pi} \Pi \\ = \frac{w^2}{2\pi^2 \sqrt{q^2 - w^2}} \left[ \ln \frac{w + 2\mu + \sqrt{(2\mu + w)^2 - q^2}}{2\mu - w + \sqrt{(2\mu - w)^2 - q^2}} \right], \quad (10)$$

and so the differences between the two are logarithmically small. In Fig. 3 we also see that  $\frac{w}{q} \text{JDOS}$  agrees remarkably well with  $\frac{q}{\pi} \sigma^L$ . The difference between these two functions is in fact controlled by the same logarithmic factor as in Eq. (10).

### B. Finite temperature

We now turn to the effect of finite temperature. In this case, the expression for the real part of the longitudinal conductivity is

$$\frac{\sigma^L(\mathbf{q}, \omega)}{\sigma_0} = \frac{4}{\pi \omega} \sum_{ss'} \int d^2\mathbf{k} [f(\epsilon_{\mathbf{k}}^s - \mu) - f(\epsilon_{\mathbf{k}+\mathbf{q}}^{s'})] \\ \times F_{ss'}(\phi) \delta(\omega + \epsilon_{\mathbf{k}}^s - \epsilon_{\mathbf{k}+\mathbf{q}}^{s'}), \quad (11)$$

where  $F_{ss'}(\phi)$  is given as in Eq. (6). We use the delta function to do the integral over the angular variables and find that the conductivity naturally separates into two parts, one part for  $\omega < q$  and the other for  $\omega > q$ . They are given by

$$\frac{\sigma_{<}}{\sigma_0} = \frac{8}{\pi} \frac{w}{q^2 \sqrt{q^2 - w^2}} \left\{ \int_0^\infty dx \left[ \frac{\sinh \frac{w}{2T}}{\cosh \frac{w}{2T} + \cosh \frac{q+2x-2\mu}{2T}} \right] \sqrt{x(x+q)} + \int_0^\infty dx \left[ \frac{\sinh \frac{w}{2T}}{\cosh \frac{w}{2T} + \cosh \frac{q+2x+2\mu}{2T}} \right] \sqrt{x(x+q)} \right\} \\ \approx \frac{8}{\pi} \frac{w}{q^2 \sqrt{q^2 - w^2}} \left\{ \int_0^\infty dx \left[ \frac{\sinh \frac{w}{2T}}{\cosh \frac{w}{2T} + \cosh \frac{q+2x-2\mu}{2T}} \right] \sqrt{x(x+q)} \right\}, \quad (12)$$

for  $\omega < q$ , and

$$\frac{\sigma_{>}}{\sigma_0} = \frac{8}{\pi} \frac{w}{q^2 \sqrt{w^2 - q^2}} \left\{ \int_0^q dx \left[ \frac{\sinh \frac{w}{2T}}{\cosh \frac{w}{2T} + \cosh \frac{q-2x-2\mu}{2T}} \right] \sqrt{x(q-x)} \right\}, \quad (13)$$

for  $\omega > q$ . We have simplified the expression for  $\sigma_{<}$  by noting that the thermal factors in the second term cause it to be much smaller than the first.

PHILLIP E. C. ASHBY AND J. P. CARBOTTE

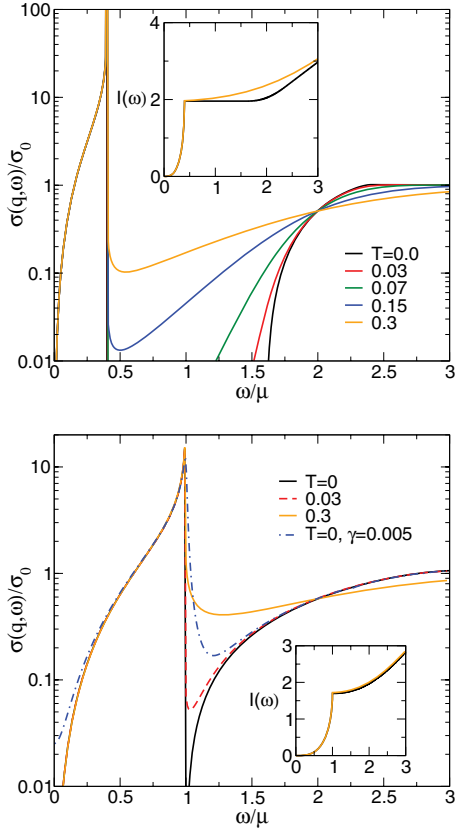
PHYSICAL REVIEW B **86**, 165405 (2012)

FIG. 3. (Color online) (Top panel) The real part of the finite momentum optical conductivity  $\sigma(\mathbf{q}, \omega)$  as a function of  $\omega/\mu$  for  $q/k_F = 0.4$  and  $T/\mu = 0, 0.03, 0.07, 0.15, 0.3$  for bare bands. There is a strong quasiparticle peak at  $\omega = q$ , which is unaffected by the finite temperature. The finite temperature smears the interband contribution and begins to fill in the Pauli-blocked region for large enough temperature. (Bottom panel) The real part of the finite momentum optical conductivity  $\sigma(\mathbf{q}, \omega)$  as a function of  $\omega/\mu$  for  $q/k_F = 1.0$  and  $T/\mu = 0, 0.03, 0.3$  for bare bands. Included for comparison is the  $T = 0$  result with a residual scattering rate  $\gamma/\mu = 0.005$ . (Insets): The insets show the optical spectral weight for  $T/\mu = 0, 0.3$ . The quasiparticle peak holds less spectral weight at larger momentum transfer ( $q$ ). For the  $q/k_F = 0.4$  case, we can see that the finite temperature has transferred spectral weight to the previously Pauli-blocked region.

The remaining integrals were evaluated numerically and the results for  $T/\mu = 0, 0.03, 0.07, 0.15, 0.3$  are shown for momentum transfer  $q/k_F = 0.4$  in Fig. 3. There is a sharp quasiparticle peak from intraband transitions at  $\omega = q$ . It remains sharp even at elevated temperatures. However, the interband transitions are thermally broadened. One naively expects thermal broadening to occur over a width  $\sim T$ , and we see the effect is much larger for the interband transitions. This excess broadening can be understood as an enhancement from the square root singularity present in the JDOS. All the finite

temperature curves intersect at the point  $\omega = 2\mu$ . This could be used as a method of determining the chemical potential. We also computed the optical spectral weight (see insets Fig. 3) given by

$$I(\omega) = \int_0^\omega d\omega' \frac{\sigma(\mathbf{q}, \omega')}{\sigma_0}. \quad (14)$$

We see that finite temperature shifts spectral weight from the interband region into the previously forbidden region  $q < \omega < 2\mu - \omega$ . Figure 3 also shows the finite temperature effect for momentum transfer  $q/k_F = 1.0$ . Again the quasiparticle peak is sharp, and the interband transitions are smeared. Notice that for larger  $q$  the spectral weight carried by the quasiparticle peak is diminished. Increasing  $q$  has the effect of decreasing the spectral weight carried by the quasiparticle peak. This spectral weight is regained in the interband transitions so that the optical sum rule remains satisfied.

Although we cannot obtain an analytic formula for the spectral weight carried by the peak at general  $q$ , we can obtain expressions for the spectral weight at  $T = 0$  in the limit  $q \rightarrow 0$ , for both the longitudinal and transverse conductivity. For the quasiparticle peak, in the  $q \rightarrow 0$  limit we obtain

$$\frac{\sigma^L}{\sigma_0} \approx \frac{8\mu\omega^2}{\pi q^2 \sqrt{q^2 - \omega^2}}, \quad (15)$$

$$\frac{\sigma^T}{\sigma_0} \approx \frac{8\mu}{\pi q^2 \sqrt{q^2 - \omega^2}}. \quad (16)$$

So that

$$\int_0^q d\omega \frac{\sigma^L}{\sigma_0} = \int_0^q d\omega \frac{\sigma^T}{\sigma_0} = 2\mu, \quad (17)$$

and both the transverse and longitudinal peaks carry the same spectral weight in this limit. The fact that the quasiparticle peak in the longitudinal and transverse conductivities have the same spectral weight, combined with isotropy implies that the peak carries the same weight regardless of the direction of  $q$  in the  $q \rightarrow 0$  limit.

### III. EFFECT OF IMPURITIES

We have, until now, considered only the bare-band case. We now consider the effect of scattering. The simplest approximation that includes scattering is to take a self energy with  $\text{Im}\Sigma(\mathbf{k}, \omega) = \gamma$  and  $\text{Re}\Sigma(\mathbf{k}, \omega) = 0$ . Note that, in particular, we ignore vertex corrections. In this case, and at  $T = 0$ , the general formula for the intraband conductivity, Eq. (1), becomes

$$\begin{aligned} \frac{\sigma^L}{\sigma_0} &= \frac{8}{\omega} \int_{-\omega}^0 d\omega' \int k dk \int_0^{2\pi} \frac{d\theta}{2\pi} F_{++}(\phi) \\ &\times \frac{1}{\pi^2 \gamma^2 + (\omega' + k + \mu)^2} \\ &\times \frac{\gamma}{\gamma^2 + (\omega' + \omega + \sqrt{k^2 + q^2 + 2kq \cos \theta} + \mu)^2}. \end{aligned} \quad (18)$$

We are only interested in the case when  $\omega, \gamma, q \ll \mu$ . In this case, consideration of the Lorentzian factors tells us that the dominant part of the integral in Eq. (18) is from the region  $k \approx \mu$ . This allows us to simplify the expressions for both

$F_{++}$  as well as the second Lorentzian in Eq. (18). Working to lowest order in  $q$  we obtain

$$\frac{\sigma^L}{\sigma_0} = \frac{8}{\omega} \int_{-\omega}^0 d\omega' \int k dk \int_0^{2\pi} \frac{d\theta}{2\pi} \cos^2(\theta) \frac{1}{\pi^2} \frac{\gamma}{\gamma^2 + (\omega' + k + \mu)^2} \frac{\gamma}{\gamma^2 + (\omega' + \bar{\omega} + k + \mu)^2}, \quad (19)$$

where  $\bar{\omega} = \omega + q \cos(\theta)$ . The integration over  $k$  can be performed and we have

$$\begin{aligned} \frac{\sigma^L}{\sigma_0} = \frac{8\gamma^2}{\pi^2 \omega} \int_{-\omega}^0 d\omega' \int_0^{2\pi} \frac{d\theta}{2\pi} \cos^2(\theta) & \left[ \frac{-2}{\bar{\omega}} \frac{1}{2\gamma^2 + \bar{\omega}^2} \left( \omega' + \frac{\bar{\omega}}{2} \right) \ln \left| \frac{(\omega' + \mu)^2 + \gamma^2}{(\omega' + \bar{\omega} + \mu)^2 + \gamma^2} \right| \right. \\ & \left. - 4\gamma - \frac{\bar{\omega}}{\gamma} (\omega' + \bar{\omega} + \mu) \tan^{-1} \left( \frac{\omega' + \bar{\omega}}{\gamma} + \mu \right) + \frac{\bar{\omega}}{\gamma} (\omega' + \mu) \tan^{-1} \left( \frac{\omega'}{\gamma} + \mu \right) \right]. \end{aligned} \quad (20)$$

Under our conditions that  $\omega, \gamma, q \ll \mu$ , this simplifies to

$$\frac{\sigma^L}{\sigma_0} = \frac{4\mu}{\pi^2} \int_0^{2\pi} d\theta \frac{2\gamma \cos^2 \theta}{(w + q \cos \theta)^2 + 4\gamma^2}. \quad (21)$$

A similar calculation gives the transverse conductivity

$$\frac{\sigma^T}{\sigma_0} = \frac{4\mu}{\pi^2} \int_0^{2\pi} d\theta \frac{2\gamma \cos^2 \theta}{(w + q \sin \theta)^2 + 4\gamma^2}, \quad (22)$$

and the polarizability

$$\Pi = \frac{\omega\mu}{\pi^2} \int_0^{2\pi} d\theta \frac{2\gamma}{(w + q \cos \theta)^2 + 4\gamma^2}. \quad (23)$$

These integrals can all easily be evaluated. They are most conveniently expressed in terms of the complex number

$$Z = \frac{1}{\sqrt{(w - q + 2i\gamma)(w + q + 2i\gamma)}}. \quad (24)$$

Our final expressions for the quasiparticle peak in the presence of scattering are

$$\frac{\sigma^L}{\sigma_0} = \frac{16\gamma\mu}{\pi q^2} \left[ 1 - 2\omega \text{Re}(Z) + \frac{\omega^2}{2\gamma} \text{Im}(Z^*) + 2\gamma \text{Im}(Z) \right], \quad (25)$$

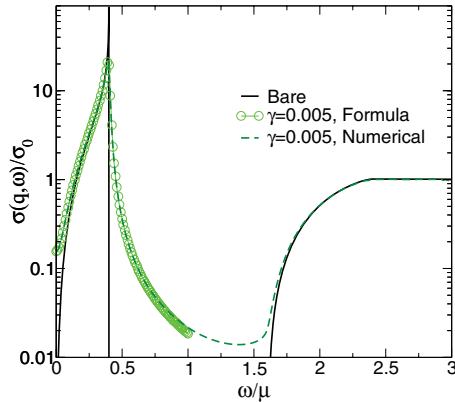


FIG. 4. (Color online) The real part of the longitudinal optical conductivity  $\sigma(\mathbf{q}, \omega)$  for  $q/k_f = 0.4$  as a function of  $\omega/\mu$ . Included are the result for bare bands at  $T = 0$  in black, a numerical evaluation of Eq. (1) including impurity scattering with  $\gamma/\mu = 0.005$  in dashed green, and our analytic expression for the quasiparticle peak, Eq. (25), in light green circles.

$$\frac{\sigma^T}{\sigma_0} = \frac{16\mu\gamma}{\pi q^2} \left[ \frac{\text{Im}(Z^*)}{2\gamma|Z|^2} - 1 \right], \quad (26)$$

$$\text{Im}(\Pi) = \frac{2\omega\mu}{\pi} \text{Im}(Z^*). \quad (27)$$

The agreement between the analytic expressions and a numerical calculation of Eq. (1) is excellent (Fig. 4). We verified that this agreement is maintained up to  $q = 1.0$ , even though our derivation assumed  $q$  was a small parameter. We show evaluations of the longitudinal conductivity, Eq. (25), for two impurity concentrations in Fig. 5 for  $q = 0.4$  and  $1.0$ . The case with no impurity scattering is included for reference. The peak becomes progressively broadened as we increase the impurity scattering rate,  $\gamma$ , but the peak position remains robust, even for large disorder.

Interestingly, our formulas for the conductivity with finite residual scattering are almost the same as the  $q \rightarrow 0$  limit of the conductivity given in Eqs. (15) and (16) with the replacement  $\omega \rightarrow \omega + 2i\gamma$ . There is an additional term present in our formulas that is not captured by this simple substitution. For the longitudinal conductivity, our expression is the same as

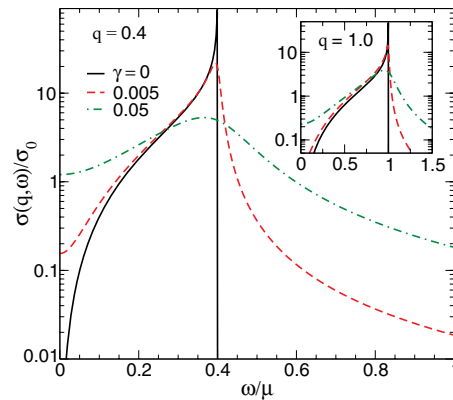


FIG. 5. (Color online) The quasiparticle peak in the real part of the optical conductivity for momentum transfer  $q = 0.4$  (main panel) and  $q = 1.0$  (inset) as a function of  $\omega/\mu$ . We show impurity concentrations of  $\gamma/\mu = 0, 0.05$ , and  $0.005$ . The position of the peak stays robust even with large impurity content and is broadened as the impurity content increases.

PHILLIP E. C. ASHBY AND J. P. CARBOTTE

PHYSICAL REVIEW B **86**, 165405 (2012)

[compare with Eq. (15)]

$$\frac{\sigma^L}{\sigma_0} = 8\mu \operatorname{Re} \left[ \frac{(\omega + 2i\gamma)^2}{\pi q^2 \sqrt{q^2 - (\omega + 2i\gamma)^2}} \right] + \frac{16\gamma\mu}{\pi q^2}. \quad (28)$$

While for the transverse conductivity it is the same as [compare with Eq. (16)]

$$\frac{\sigma^T}{\sigma_0} = 8\mu \operatorname{Re} \left[ \frac{\sqrt{q^2 - (\omega + 2i\gamma)^2}}{\pi q^2} \right] - \frac{16\gamma\mu}{\pi q^2}. \quad (29)$$

As a final remark, we comment on the difference between the polarizability and the optical conductivity. In the noninteracting case it has been shown<sup>24</sup> that the polarizability is related to the conductivity through the standard formula

$$\sigma^L = \frac{\omega}{q^2} \operatorname{Im}(\Pi). \quad (30)$$

We remarked on the differences between the coherence factors of the polarizability and the conductivity in Sec. II A. In the noninteracting case, the spectral densities in Eq. (1) reduce to delta functions, and the delta-function constraints restrict the coherence factors of the polarizability and the conductivity to be related through only the factor  $\omega/q^2$ . In the presence of impurities, the delta functions become broadened and the coherence factors are no longer proportional. In fact, we see that the replacement given by Eq. (30) using the polarizability in the presence of impurities Eq. (27) only generates one of the terms present in the optical conductivity Eq. (25). It is

$$\begin{aligned} \text{JDOS}(\mathbf{q}, \omega) = & \frac{1}{4\pi^2 \sqrt{q^2 - \omega^2}} \left\{ \Theta(\omega - qx_0 + 2\mu) \left[ (2\mu + w) \sqrt{(2\mu + w)^2 - q^2 x_0^2} \right. \right. \\ & - (q^2 x_0^2 - 2w^2) \ln \frac{\sqrt{(2\mu + w)^2 - q^2 x_0^2} + (2\mu + w)}{qx_0} \left. \right] - \Theta(2\mu - qx_0 - w) \left[ (2\mu - w) \sqrt{(2\mu - w)^2 - q^2 x_0^2} \right. \\ & \left. \left. - (q^2 x_0^2 - 2w^2) \ln \frac{\sqrt{(2\mu - w)^2 - q^2 x_0^2} + (2\mu - w)}{qx_0} \right] \right\}, \end{aligned} \quad (32)$$

$$\quad (33)$$

where  $\mu = \sqrt{k_F^2 + \Delta^2}$  and  $x_0 = \sqrt{1 + \frac{4\Delta^2}{q^2 - \omega^2}}$ . Figure 6 shows the quasiparticle peak in the optical conductivity for several values of the gap, as well as the joint density of states. We see that as the gap opens, the joint density of states flattens out and is pulled back to smaller values of  $\omega$ . Consequently, this behavior is inherited in the optical conductivity. The peak is shifted to smaller values of  $\omega$  and broadened as  $\Delta$  increases. In particular, the flattening onsets at  $\omega_l = \sqrt{k_F^2 + \Delta^2} - \epsilon(k_F - q)$  and persists to  $\omega_u = \epsilon(k_F + q) - \sqrt{k_F^2 + \Delta^2}$ , where the conductivity then vanishes.

### B. Strained graphene

We consider, for simplicity, the case where strain is applied along the armchair (or  $y$ ) direction in graphene (Fig. 1). The effect of such a strain can be captured by introducing two strain parameters,  $\gamma_x$  and  $\gamma_y$ , which control the anisotropy into the

worth noting that the term generated by the polarizability is the dominant term near  $\omega = q$ . At small values of  $\omega$ , the  $Z$ -independent piece becomes the dominant contribution. All the terms not proportional to the polarizability are suppressed by factors of  $\gamma$  so that the correct limit is obtained as we turn off impurity scattering.

## IV. MODIFICATIONS TO THE DIRAC SPECTRUM

Finally, we examine the consequences of altering the energy spectrum in graphene on the quasiparticle peak in the optical conductivity. We will consider two physical mechanisms for altering the spectrum in graphene. The first is the opening of a mass gap,  $\Delta$ . The second is the application of strain, which makes the Fermi velocities along  $x$  and  $y$  different. These alterations to the spectrum are shown pictorially in Fig. 1.

### A. Gapped graphene

In graphene with gap  $\Delta$ , the energy eigenvalues are no longer linear in  $k$  but instead are given by

$$\epsilon_k = \sqrt{k^2 + \Delta^2}. \quad (31)$$

The optical conductivity of gapped graphene was first studied by Scholz and Schliemann.<sup>24</sup> As we saw in Sec. II, the peak in the optical conductivity depended strongly on the joint density of states. The joint density of states for gapped graphene is

Dirac Hamiltonian<sup>25–27</sup>

$$\mathcal{H} = \gamma_x \sigma_x k_x + \gamma_y \sigma_y k_y. \quad (34)$$

First we consider the longitudinal conductivity, that is,  $q$  along  $k_x$ . By examining the Kubo formula for the conductivity, Eq. (1), we find that the change of variables  $\bar{k} = (\gamma_x k_x, \gamma_y k_y)$  is sufficient to give us a result for the strained conductivity. There is a Jacobian from the  $k$ -space integration that contributes a factor  $1/(\gamma_x \gamma_y)$ . Additionally, there is a factor of  $v_F^2$  (1 in our units), which contributes a  $\gamma_x^2$  (for  $\sigma_{xx}$ ). Last, since  $q$  appears only in  $\epsilon_{\mathbf{k}+\mathbf{q}}$ , it is changed to  $\bar{q} = q\gamma_x$ . Expressed in terms of  $\bar{k}, \bar{q}$ , all the integrations are the same as the unstrained case. Thus, we arrive at the simple result

$$\sigma_{\text{strained}}^L(q, \omega) = \frac{\gamma_x}{\gamma_y} \sigma_{\text{iso}}^L(q\gamma_x, \omega). \quad (35)$$

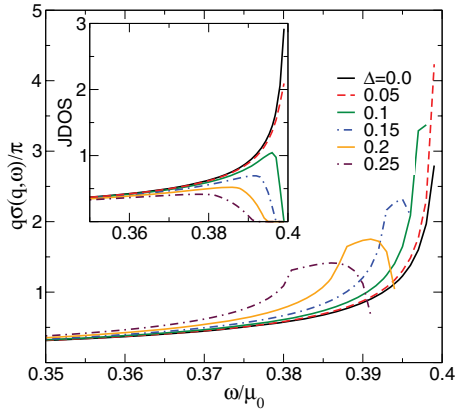


FIG. 6. (Color online) The quasiparticle peak in the real part of the optical conductivity as a function of  $\omega/\mu$  for  $q/k_F = 0.4$  for graphene with mass gap  $\Delta = 0, 0.05, 0.1, 0.15, 0.2, \text{ and } 0.25$ . The peak is pulled to smaller values of  $q$  and slowly broadened as the mass gap increases. The broadening happens over an energy scale approximately given by the mass gap and is physically caused by changes in the joint density of states (shown in the inset).

A similar calculation for the transverse conductivity gives

$$\sigma_{\text{strained}}^T(q, \omega) = \frac{\gamma_x}{\gamma_y} \sigma_{\text{iso}}^T(q\gamma_y, \omega). \quad (36)$$

We see that the position of the peak is shifted from  $\omega = q$  to  $\omega = \gamma_x q$ , and the overall conductivity is modified by the ratio  $\gamma_x/\gamma_y$ .

This shift in the peak is also understandable from the physical picture described in Sec. II A described earlier. Considering the same transitions described there gives the peak at  $\omega = q$ . The effect of strain on the system is to distort the shape of the cone. Focusing on the  $x$  direction, we have that, geometrically, this changes the lengths of the vectors by a factor  $\gamma_x$ . To still land on the energy dispersion (and thus be

an allowed transition), the energy must also be modified by a factor of  $\gamma_x$ . This simple geometric consideration gives the shift in the peak position.

## V. CONCLUSIONS

We have considered the peak in the real part of the near-field optical conductivity. The peak is located at  $\omega = q$ , and, as long as the dispersion is linear and isotropic, this position is robust. This quasiparticle peak is due to intraband transitions and is the finite  $q$  analog of the Drude peak, in the  $q = 0$  conductivity. At  $q = 0$ , the peak carries  $2\mu$  worth of spectral weight so that the optical sum rule is satisfied. At finite  $q$ , the quasiparticle peak carries less weight, with the missing weight transferred to interband processes.

We find that both finite temperatures and finite residual scattering rate fill in the Pauli-blocked region, and that this filling is enhanced near  $\omega = q$  due to a square-root singularity in the density of states. We used the Kubo formula in the bubble approximation, which ignores vertex corrections, to understand how the bare band picture is modified, in the presence of residual scattering. This allowed us to derive simple expressions for quasiparticle peaks in longitudinal and transverse conductivity, as well as the contribution from intraband scattering to the polarizability.

Finally, we examined the effect of altering the Dirac dispersion on this peak. We found that in the presence of a gap, the peak was shifted to smaller values of  $\omega$ , and reduced in size, no longer able to feel the square-root singularity in the JDOS. The peak also broadened as the mass gap increased. In the presence of strain, the effect was to scale the height of the peak by a geometric factor related to the ratio of the anisotropies induced by the strain, in addition to the position of the peak being shifted by the relevant anisotropy parameter.

## ACKNOWLEDGMENTS

This work was supported by the Natural Sciences and Engineering Research Council of Canada (NSERC) and the Canadian Institute for Advanced Research (CIFAR).

\* ashbype@mcmaster.ca

† carbotte@mcmaster.ca

<sup>1</sup>K. S. Novoselov, A. K. Geim, S. V. Morozov, D. Jiang, Y. Zhang, S. V. Dubonos, I. V. Grigorieva, and A. A. Firsov, *Science* **306**, 666 (2004).

<sup>2</sup>E. H. Hwang and S. Das Sarma, *Phys. Rev. B* **75**, 205418 (2007).

<sup>3</sup>R. Sensarma, E. H. Hwang, and S. Das Sarma, *Phys. Rev. B* **82**, 195428 (2010).

<sup>4</sup>B. Wunsch, T. Stauber, F. Sols, and F. Guinea, *New J. Phys.* **8**, 318 (2006).

<sup>5</sup>T. Stauber and G. Gómez-Santos, *Phys. Rev. B* **82**, 155412 (2010).

<sup>6</sup>T. Stauber, N. M. R. Peres, and A. K. Geim, *Phys. Rev. B* **78**, 085432 (2008).

<sup>7</sup>A. B. Kuzmenko, E. van Heumen, F. Carbone, and D. van der Marel, *Phys. Rev. Lett.* **100**, 117401 (2008).

<sup>8</sup>F. Wang, Y. Zhang, C. Tian, C. Girit, A. Zettl, M. Crommie, and Y. R. Shen, *Science* **320**, 206 (2008).

<sup>9</sup>S. A. Mikhailov and K. Ziegler, *Phys. Rev. Lett.* **99**, 016803 (2007).

<sup>10</sup>A. Bostwick, F. Speck, T. Seyller, K. Horn, M. Polini, R. Asgari, A. H. MacDonald, and E. Rotenberg, *Science* **328**, 999 (2010).

<sup>11</sup>J. P. Carbotte, J. P. F. LeBlanc, and E. J. Nicol, *Phys. Rev. B* **85**, 201411 (2012).

<sup>12</sup>M. Orlita and M. Potemski, *Semicond. Sci. Technol.* **25**, 063001 (2010).

<sup>13</sup>V. P. Gusynin, S. G. Sharapov, and J. P. Carbotte, *Phys. Rev. Lett.* **98**, 157402 (2007).

<sup>14</sup>T. Ando, Y. Zheng, and H. Suzuura, *J. Phys. Soc. Jpn.* **71**, 1318 (2002).

<sup>15</sup>V. P. Gusynin, S. G. Sharapov, and J. P. Carbotte, *New J. Phys.* **11**, 095013 (2009).

PHILLIP E. C. ASHBY AND J. P. CARBOTTE

PHYSICAL REVIEW B **86**, 165405 (2012)

- <sup>16</sup>Z. Q. Li, E. A. Henriksen, Z. Jiang, Z. Hao, M. C. Martin, P. Kim, H. L. Stormer, and D. N. Basov, *Nat. Phys.* **4**, 532 (2008).
- <sup>17</sup>N. M. R. Peres, T. Stauber, and A. H. C. Neto, *Europhys. Lett.* **84**, 38002 (2008).
- <sup>18</sup>T. Stauber and N. M. R. Peres, *J. Phys.: Condens. Matter* **20**, 055002 (2008).
- <sup>19</sup>T. Stauber, N. M. R. Peres, and A. H. Castro Neto, *Phys. Rev. B* **78**, 085418 (2008).
- <sup>20</sup>J. P. Carbotte, E. J. Nicol, and S. G. Sharapov, *Phys. Rev. B* **81**, 045419 (2010).
- <sup>21</sup>Z. Fei *et al.*, *Nano Lett.* **11**, 4701 (2011).
- <sup>22</sup>Z. Fei *et al.*, *Nature* **487**, 82 (2012).
- <sup>23</sup>J. Chen *et al.*, *Nature* **487**, 77 (2012).
- <sup>24</sup>A. Scholz and J. Schliemann, *Phys. Rev. B* **83**, 235409 (2011).
- <sup>25</sup>V. M. Pereira, R. M. Ribeiro, N. M. R. Peres, and A. H. C. Neto, *Europhys. Lett.* **92**, 67001 (2010).
- <sup>26</sup>A. Sharma, V. N. Kotov, and A. H. C. Neto, arXiv:1206.5427v2 (2012).
- <sup>27</sup>F. M. D. Pellegrino, G. G. N. Angilella, and R. Pucci, *Phys. Rev. B* **84**, 195407 (2011).

### 3.3 Paper II – Impact of electron-phonon coupling on near-field optical spectra in graphene

Reprinted with permission as follows: J.P Carbotte, J.P.F. LeBlanc and Phillip E.C. Ashby “*Impact of electron-phonon coupling on near-field optical spectra in graphene*” Phys. Rev. B **87** 045405 (2013). Copyright (2013) by the American Physical Society.

In this paper we follow up on our previous paper, but examine the effects of the electron-phonon interaction on the near field conductivity. While I am not the primary author on this paper, my previous manuscript “Tracking quasiparticle energies in graphene with near-field optics” provided much background needed to push this project forward. Again, we studied the properties of the quasiparticle peak in graphene to gain an understanding of how this interaction changes the bare results.

PHYSICAL REVIEW B 87, 045405 (2013)

**Impact of electron-phonon coupling on near-field optical spectra in graphene**J. P. Carbotte,<sup>1,2</sup> J. P. F. LeBlanc,<sup>3,\*</sup> and Phillip E. C. Ashby<sup>1</sup><sup>1</sup>*Department of Physics and Astronomy, McMaster University, Hamilton, Ontario L8S 4M1, Canada*<sup>2</sup>*The Canadian Institute for Advanced Research, Toronto, Ontario M5G 1Z8, Canada*<sup>3</sup>*Max-Planck Institute for the Physics of Complex Systems, 01187 Dresden, Germany*

(Received 4 September 2012; revised manuscript received 29 October 2012; published 7 January 2013)

The finite momentum transfer  $\mathbf{q}$  longitudinal optical response  $\sigma^L(\mathbf{q}, \omega)$  of graphene has a peak at an energy  $\omega = \hbar v_F q$ . This corresponds directly to a quasiparticle peak in the spectral density at a momentum relative to the Fermi momentum  $k_F - q$ . Inclusion of coupling to a phonon mode at  $\omega_E$  results, for  $\omega < |\omega_E|$ , in an electron-phonon renormalization of the bare bands by a mass enhancement factor  $(1 + \lambda)$ , and this is followed by a phonon kink for  $\omega$  around  $\omega_E$  where additional broadening begins. Here we study the corresponding changes in the optical quasiparticle peaks, which we find continue to track directly the renormalized quasiparticle energies until  $q$  is large enough that the optical transitions begin to sample the phonon kink region of the dispersion curves, where linearity in momentum and the correspondence to a single-quasi-particle energy are lost. Nevertheless there remain in  $\sigma^L(\mathbf{q}, \omega)$  features analogous to the phonon kinks of the dispersion curves which are observable through variation of  $q$  and  $\omega$ .

DOI: 10.1103/PhysRevB.87.045405

PACS number(s): 78.67.Wj, 71.38.Cn, 78.66.Tr

Important information on the charge dynamics of the Dirac fermions in graphene is obtained in optical-absorption experiments. Results are reviewed by Orlita and Potemski.<sup>1</sup> For bare bands the real part of the zero-momentum limit optical conductivity  $\sigma(\mathbf{q} = 0, \omega)$  has a Drude peak around  $\omega = 0$ , which has its origin in the intraband optical transitions. There is also an additional piece due to the interband transitions with onset at twice the chemical potential, which provides a constant universal background of value  $\sigma_0 = \pi e^2 / 2h$ .<sup>2-4</sup> While in the clean limit the Pauli blocked region between the Drude and the universal background would have essentially no conductivity, experimental work<sup>5</sup> has found instead a value of order  $\sigma_0/3$ . This observation can be partially explained<sup>6-9</sup> due to impurities, electron-phonon interactions (EPIs), and Coulomb correlations, although its precise origin remains controversial. In conventional metals the electron-phonon interaction is known to renormalize many of their properties.<sup>10</sup> It leads to incoherent phonon-assisted Holstein sidebands<sup>11</sup> in addition to the main coherent Drude response with optical spectral weight now being distributed between these two parts. The effect on the Drude weight can be expressed in terms of the electron-phonon mass renormalization parameter  $\lambda$ . The Drude weight is reduced by a multiplicative factor of  $1/(1 + \lambda)$ , while the remaining  $\lambda/(1 + \lambda)$  is transferred to the sideband due to the new absorption processes in which a phonon is created by a photon along with a hole-particle pair. In graphene, electron-phonon effects have been seen<sup>12</sup> in the electronic density of states (DOS),  $N(\omega)$ , measured in scanning tunneling spectroscopy (STS). These observations are expected in systems where the DOS is energy dependent.<sup>13-16</sup> Phonon “kinks” have also been seen in angle-resolved photoemission spectroscopy (ARPES)<sup>17,18</sup> as predicted theoretically.<sup>19-22</sup> Recently, near-field optical techniques have been used to obtain information on the finite momentum conductivity<sup>23-26</sup> rather than the standard long-wavelength,  $q \rightarrow 0$ , limit. This has allowed for nanoimaging<sup>23-25</sup> of the graphene plasmons and could in principle be employed to get information on plasmarons,<sup>26</sup> a scattering resonance of an electron and a plasmon.<sup>27</sup> In this paper we show how  $\sigma(\mathbf{q}, \omega)$  can provide information

on electron-phonon renormalization effects complementary to ARPES and STS.

The Kubo formula for the real part of the finite momentum optical conductivity is approximated by the simplest bubble diagram, which is not exact since it neglects vertex corrections. Cappelluti and Benfatto<sup>28</sup> have studied the effect of vertex corrections on the conductivity of graphene and found that, as is the case in conventional metals, their main effect can be incorporated into Eq. (1) by changing the scattering rate from its quasiparticle value to an appropriate optical rate which contains an extra factor of  $(1 - \cos \beta)$ , where  $\beta$  is the scattering angle. This well-known factor gives more weight to backward scattering and de-emphasises forward scattering. In this approximation interactions are included through and is given by

$$\frac{\sigma(\mathbf{q}, \omega)}{\sigma_0} = \frac{8}{\omega} \int_{-\omega}^0 d\omega' \int \frac{d^2\mathbf{k}}{2\pi} \sum_{s,s'=\pm} F_{ss'}(\phi) \times A^s(\mathbf{k}, \omega') A^{s'}(\mathbf{k} + \mathbf{q}, \omega' + \omega), \quad (1)$$

where  $A^s(k, \omega)$  is the spectral function of the Dirac fermions. The overlap factor,  $F_{ss'}(\phi)$ , has the form  $F_{ss'}(\phi) = \frac{1}{2}[1 + ss' \cos \phi]$ , where  $\phi$  is the sum of the angles of initial momentum  $\mathbf{k}$  and final momentum  $\mathbf{k} + \mathbf{q}$ , with respect to the  $k_x$  axis (zigzag direction). We define  $\alpha$  to be the angle between the  $k_x$ -axis and  $\mathbf{q}$  and obtain

$$F_{ss'}(\phi) = \frac{1}{2} \left[ 1 + ss' \frac{k \cos(2\theta) + q \cos(\theta + \alpha)}{\sqrt{k^2 + q^2 + 2kq \cos(\theta - \alpha)}} \right]. \quad (2)$$

In this representation,  $\theta$  is the angle over which  $\mathbf{k}$  is integrated in Eq. (1). The values of  $s$  and  $s'$  are each either  $+1$  or  $-1$ , which represents the upper ( $+$ ) and lower ( $-$ ) Dirac cones. For simplicity we take the chemical potential to fall in the upper cone, representing an electron doped sheet. In general the conductivity  $\sigma_{ij}(q, \omega)$  can be written as a linear combination of a longitudinal part  $\sigma^L(q, \omega)$  and a transverse part  $\sigma^T(q, \omega)$ .<sup>29</sup> If we select  $\mathbf{q} = q\hat{x}$ , where  $\alpha = 0$  in our orientation, then we find that the conductivity along the  $x$  direction,  $\sigma_{xx}(q, \omega)$ , has

CARBOTTE, LEBLANC, AND ASHBY

 PHYSICAL REVIEW B **87**, 045405 (2013)

only a contribution from the longitudinal conductivity, i.e.,  $\sigma_{xx}(q, \omega) = \sigma^L(q, \omega)$ , while the conductivity along the  $y$  axis,  $\sigma_{yy}(q, \omega)$ , has only a contribution from the transverse part, i.e.,  $\sigma_{yy}(q, \omega) = \sigma^T(q, \omega)$ . Throughout this work, we are interested in examining quasi-particle-like peaks which appear only in the longitudinal part of the near-field optical spectra, and therefore we will limit our discussion to examining  $\sigma^L(q, \omega)$ .

Denoting the self-energy by  $\Sigma_s(k, \omega)$ , the spectral function is

$$A^s(\mathbf{k}, \omega) = \frac{1}{\pi} \frac{|\text{Im}\Sigma_s(\mathbf{k}, \omega)|}{[\omega - \text{Re}\Sigma_s(\mathbf{k}, \omega) - \epsilon_k^s]^2 + [\text{Im}\Sigma_s(\mathbf{k}, \omega)]^2}, \quad (3)$$

$$-\text{Im}\Sigma^{\text{EPI}}(\omega, \omega_E) = \begin{cases} \frac{\pi A}{W_c} |\omega - \omega_E + \mu_0|, & \text{for } \omega_E < \omega < W_c - \mu_0 + \omega_E \\ \frac{\pi A}{W_c} |\omega + \omega_E + \mu_0|, & \text{for } -\omega_E > \omega > -W_c - \mu_0 - \omega_E \end{cases}, \quad (4)$$

from which the real part can be obtained through a Kramers-Kronig transform. We use the notation set out in Ref. 9, where more details can be found. In Eq. (4),  $A$  is a constant that can be adjusted to get a desired value of the mass enhancement parameter  $\lambda$ , and  $W_c$  is a cutoff on the bare band energies adjusted to get the correct number of states in the Dirac approximation of two valleys in the Brillouin zone. By definition  $\lambda$  is obtained from the small  $\omega$  limit of the real part of  $\Sigma(\omega)$ . In this limit,  $\text{Re}\Sigma^{\text{EPI}}(\omega) = \text{Re}\Sigma^{\text{EPI}}(0) - \lambda\omega$ , where the constant piece,  $\text{Re}\Sigma^{\text{EPI}}(0)$ , shifts the chemical potential from its bare to interacting value.

The real part of the longitudinal conductivity follows from a numerical evaluation of Eq. (1). Results are shown in Fig. 1 for ten values of  $q/k_F$  from 0.0  $\rightarrow$  0.9. The solid black curve is the well-known<sup>6-9</sup>  $q = 0$  case and is included here for comparison. There is a Drude piece at small  $\omega$ , which is followed by a boson assisted part that sets in abruptly at  $\omega = \omega_E$ . Here we have used a model for the self-energy which also includes a constant impurity scattering term  $\eta$ , in addition to the self-energy from the electron-phonon interaction. This constant scattering contributes no energy renormalization but broadens the Drude component. The EPI, however, reduces the optical spectral weight of the coherent Drude part and redistributes it in the phonon assisted part, which corresponds to intraband absorption. At higher energies (not shown here) there is additional absorption due to interband optical transitions, which in the bare band case start abruptly at a frequency of twice the chemical potential. With electron-phonon coupling these also spill into the Pauli blocked region below  $2\mu$ . When  $q$  is finite we get the series of curves labeled by the energy of the position of the peaks in  $\sigma^L(q, \omega)$ . One might refer to these peaks as quasiparticle peaks since their energies correspond exactly to  $\epsilon_{k_F - q}^+$  in the bare band case.

Here, for small values of  $q$ , the peaks in  $\sigma(q, \omega)$  correspond instead to the renormalized quasiparticle energies  $\epsilon^+(k_F - q)/[1 + \lambda]$ . However, when  $q$  approaches the phonon energy

where  $\epsilon_k^s = sv_F k - \mu$ , where  $v_F$  is the Fermi velocity. The self-energy  $\Sigma_s(\mathbf{k}, \omega)$  can, in general, depend on band index and momentum as well as on energy. Detailed calculations of the electron-phonon interaction in graphene have been presented by Park and coworkers,<sup>30,31</sup> who conclude that a reasonable approximation to the complete calculations is to use a model of coupling to a single phonon of energy  $\omega_E = 200$  meV with no dependence on valley index and momentum. Here we follow this suggestion. If one were inclined, a distribution of phonon modes can be created through an integration over  $\omega_E$  in Eq. (4) weighted by the phonon density of states at each frequency, as has been done previously.<sup>9,32</sup> For an electron-phonon interaction (EPI) which includes coupling to a single phonon at frequency  $\omega_E$ , the imaginary part of the self-energy,  $\Sigma^{\text{EPI}}(\omega)$ , is given by

this simple renormalization ceases to hold. The broadening of the curves increases above  $\omega = \omega_E$ . This indicates that a new channel for scattering has opened: in our case, phonon emission. In the inset of Fig. 1, we plot the imaginary part of the self-energy, which contains a sharp jump in scattering at the phonon energy. Note that the Dirac point in the inset occurs where the imaginary part of the EPI self-energy is zero, which comes from a zero in the electronic density of states at this energy.

Figure 2 illustrates in a schematic fashion the effect of the electron-phonon interaction on the Dirac cone dispersion

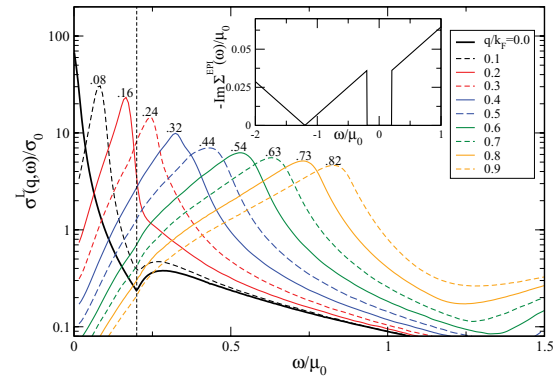


FIG. 1. (Color online) The real part of the finite momentum longitudinal optical conductivity  $\sigma^L(q, \omega)/\sigma_0$  as a function of  $\omega/\mu_0$  for a selection of values of  $q/k_F$  from 0.0  $\rightarrow$  0.9 (as defined in the legend). These include an electron-phonon interaction with  $\lambda \approx 0.18$  for a single optical phonon mode at  $\omega_E = 200$  meV (shown by the vertical dashed line), where  $\mu_0 = 1$  eV,  $A = 0.08$  eV, and  $W_c = 7.0$  eV, and a residual scattering  $\eta = 0.005\mu_0$ . Inset:  $-\text{Im}\Sigma^{\text{EPI}}(\omega)/\mu_0$  as in Eq. (4) for parameters in the main frame.

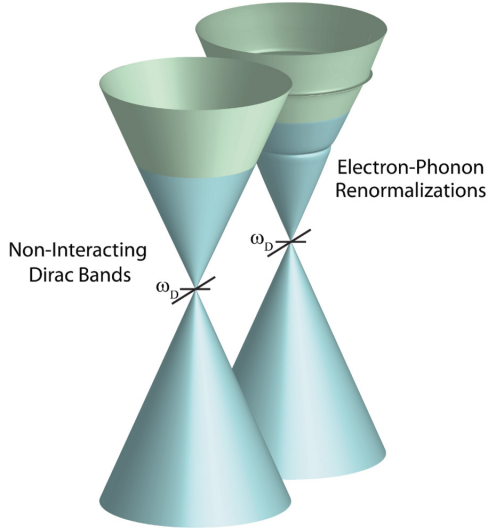


FIG. 2. (Color online) Schematic of doped Dirac bands. An electron-phonon interaction renormalizes the Dirac bands, changing the slope through the Dirac point and producing kinks at  $\omega = \pm\omega_E$ , where the Fermi level ( $\omega = 0$ ) is illustrated by a change in color.

relations. For the bare case, the Fermi velocity sets the angular dimension of each cone. Interactions distort the cones in two important ways. First, around the Fermi level the bare Fermi velocity is renormalized to a dressed value through a mass enhancement factor of  $(1 + \lambda)$ . As we move away from the Fermi energy this simple law starts to break down and phonon structures (referred to as “kinks”) develop at  $\omega = \pm\omega_E$  from the Fermi energy, and they are measured in ARPES experiments. These features are shown in the inset of Fig. 3. The solid red curve depicts the peaks in the phonon renormalized spectral function, which illustrates the kinks at  $\pm\omega_E$  as compared to the dashed black curve, which is the bare cone dispersion. In general the renormalized dispersion curves are also broadened.

Here we want to know how the phonon “kinks” in the dressed dispersions manifest in the near-field optics. This is illustrated in the main frame of Fig. 3, where the energies of the peaks in the real part of the optical conductivity  $\sigma(q, \omega)$  are traced as a function of momentum,  $k_F - q$ , and are shown as the solid black curve. These are compared with the solid red curve which traces the peaks in the spectral density  $A(k, \omega)$  as a function of momentum, relative to the Fermi level. The open circles with the green curve represent a straight line having a Fermi velocity renormalized by  $1/(1 + \lambda)$  as compared to the bare dispersions shown as the dashed curve. Note that for energies a bit above the phonon energy at  $\omega_E$  the peaks in the optical conductivity and in the single-particle spectral density of ARPES agree with each other and both fall on the renormalized Dirac fermion energy  $\epsilon_k^+/(1 + \lambda)$  (light solid green curve). In Fig. 4 we show the transitions which contribute to the optical conductivity at  $\omega = q$ . Because of the linearity of the Dirac dispersion curves, all transitions with  $q_1 + q_2 = q$  contributed to the same energy  $\omega$ , and this large degeneracy

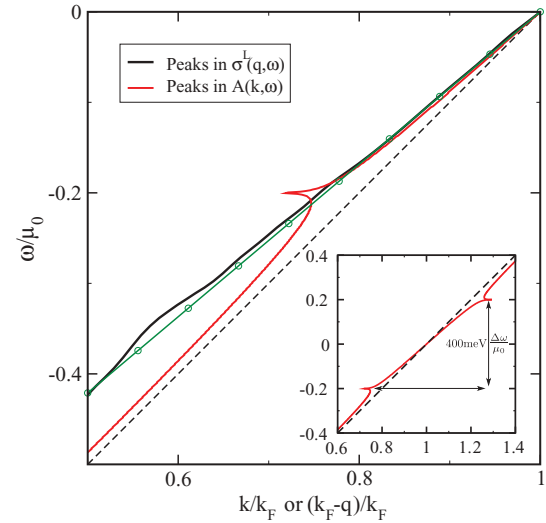


FIG. 3. (Color online) The peaks in  $\sigma^L(q, \omega)$  plotted as a function of  $k_F - q$  coincide with peaks in the EPI renormalized spectral function  $A(k, \omega)$ , plotted as a function of  $k$ . For comparison, the bare dispersion is shown by the dashed line, while the green line with circles is the bare dispersion divided by  $(1 + \lambda)$ , which is the slope of the EPI renormalized spectral function (shown in red) at  $k = k_F$ . The peaks in  $\sigma^L(q, \omega)$  sample the renormalized dispersion until near  $\omega = -\omega_E$ . Inset:  $A(k, \omega)$  as in the main frame but showing both positive and negative frequencies.

produces a peak at  $\omega = q$  in  $\sigma^L(q, \omega)$ . This only holds for linear dispersions. Above  $\omega_E$  this simple relationship ceases to hold with optics (solid black) roughly tracing the renormalized dispersion (green curve), while ARPES (solid red) is closer to

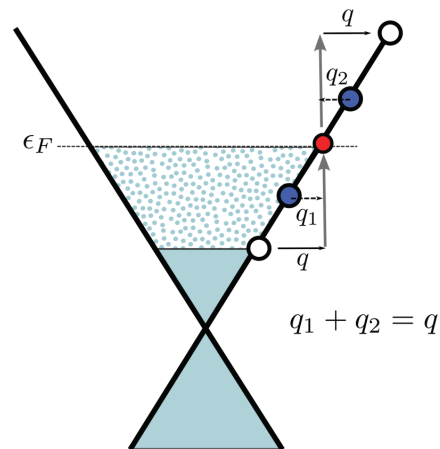


FIG. 4. (Color online) Schematic showing the many optical transitions from occupied states at energy  $\epsilon = -q_1$  to unoccupied states at  $\epsilon = q_2$ , which all contribute to  $\sigma^L(q, \omega)$  at  $\omega = q$  when the dispersion curves are linear. The large degeneracy of transitions gives a peak in the optical conductivity at  $\omega = q$ .

CARBOTTE, LEBLANC, AND ASHBY

 PHYSICAL REVIEW B **87**, 045405 (2013)

the bare dispersion (dashed). While the dressed quasiparticle spectral peaks show a phonon kink at  $\omega = \omega_E$  there is no discernible structure in the optical conductivity at this energy. It is important to remember that optics involves a joint density of states from an initial occupied electron state to a final unoccupied one. While many optical transitions correspond to a given energy it is clear that transitions from a kink to a second kink have a large weight and thus introduce structures into  $\sigma^L(q, \omega)$  for frequencies which fall in magnitude just below  $|2\omega_E|$ .

Very recently, Ashby and Carbotte<sup>33</sup> have studied the case of residual scattering alone and for small  $q$  values have derived in first order an analytic formula which has proved quite accurate. Here we have generalized their work to include the electron-phonon interaction in the regime where the renormalized quasiparticle energies are well represented by the formula  $\epsilon_k^+/(1 + \lambda)$ . We obtain

$$\frac{\sigma^L(q, \omega)}{\sigma_0} = \frac{4\mu_0}{\pi} \int_0^{2\pi} \frac{d\theta}{2\pi} \frac{2 \cos^2(\theta)(2\eta)}{(2\eta)^2 + [\omega(1 + \lambda) + q \cos \theta]^2}. \quad (5)$$

To obtain this expression we have made an approximation by including only the coherent part of the Green's function,  $G(k, \omega)$ , where the standard  $\omega$  is replaced by  $\omega(1 + \lambda)$ . In the clean limit ( $\eta \rightarrow 0$ ) we get

$$\frac{\sigma^L(q, \omega)}{\sigma_0} = \frac{8\mu_0}{\pi} \left(\frac{\omega}{\bar{q}}\right)^2 \frac{1}{\sqrt{\bar{q}^2 - \omega^2}} \frac{1}{1 + \lambda}, \quad (6)$$

with  $\bar{q} = q/(1 + \lambda)$ . We see that the square-root singularity is at  $\omega = \bar{q}$  rather than at  $q$  as in the bare band case. Also the optical spectral weight under  $\sigma^L(q, \omega)$  is reduced by a factor of  $1/(1 + \lambda)$  and is given by

$$\int_0^\infty d\omega \frac{\sigma^L(q, \omega)}{\sigma_0} = 2\mu_0/(1 + \lambda). \quad (7)$$

The missing optical spectral weight is transferred to a phonon assisted Holstein sideband described by the incoherent piece of the Green's function. This band starts at the phonon energy  $\omega_E$ , as is seen most clearly in the first two curves in Fig. 1 for  $q/k_F = 0.0$  and  $0.08$ . For a finite value of  $\eta$ , taking out the  $(1 + \lambda)$  factor next to  $\omega$  in Eq. (5) will leave an overall multiplicative factor of  $1/(1 + \lambda)$  in addition to changing  $q$  to  $\bar{q}$ . The scattering rate is also renormalized in the same manner as  $\bar{\eta} = \eta/(1 + \lambda)$ . This result means that the electron-phonon interaction reduces the effective residual scattering rate at low frequencies. These scalings are all in agreement with previous work<sup>9</sup> for the conventional case of  $q = 0$ , which exhibits a Drude peak (intraband transitions) in the energy region below the onset of the interband transitions, which start at  $\omega = 2\mu_0$ .

In Fig. 3 we concentrated on the energies of the renormalized peaks in the optical conductivity and their relationship to peaks in the quasiparticle spectral density. Both are due to the real part of the quasiparticle self-energies. In Fig. 5 we illustrate the effect of interactions on the broadening of the peaks, which depends on the imaginary part of the self-energy. For each of the four values of  $q/k_F$  we show three cases. The dashed lines include both real and imaginary parts for the full self-energy with coupling to the phonon as well as to impurities ( $\eta$ ). Open circles are for the clean limit (no scattering) of

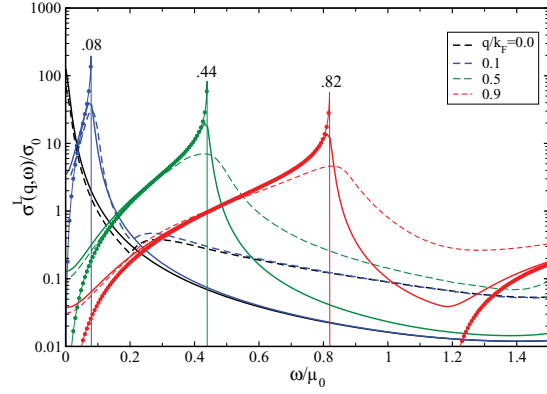


FIG. 5. (Color online) The real part of the finite momentum optical conductivity  $\sigma^L(q, \omega)/\sigma_0$  as a function of  $\omega/\mu_0$  for a selection of values of  $q/k_F$ . The dashed lines include the electron-phonon interaction identically to Fig. 1 for  $q/k_F$  displayed in the legend, while the solid lines include only the residual scattering of  $\eta = 0.005\mu_0$  but for shifted  $q$  values (marked near the peaks). The solid circles mark the analytical clean limit results, with an adjusted Fermi velocity to obtain the same peak positions.

Eq. (6) but where the energies  $\epsilon_k^+$  of the bare bands have been shifted to peak at the same energy as the renormalized bands (values labeled on individual peaks). We first note that all of these curves have a rise as  $\omega$  approaches  $q$  from below, above which they drop sharply to zero. The peak at  $\omega = q$  in the solid lines, which include a small residual scattering rate of  $\eta = 0.005\mu_0$ , shows smearing which results in a finite conductivity for  $\omega$  just above  $q$ . When the electron-phonon interaction is also included (dashed lines) this smearing of the spectral peak above  $\omega = q$  is further increased due to boson assisted processes. This additional interaction, however, has little effect at  $\omega = q$  for small  $q$ , as illustrated in the  $q/k_F = 0$  and  $0.1$  cases as compared with the larger  $q = 0.5$  and  $0.9$ . For the small  $q$  values there is no effect of the EPI in the region of the peak, except to shift the frequency at which the peak occurs by a factor of the EPI renormalization,  $(1 + \lambda)$ . For larger  $q$  values, the EPI causes a significant reduction in the peak height and filling of the Pauli blocked region. These effects are due to a finite imaginary part of the electron-phonon self-energy. While the quasiparticle self-energy has a sharp onset at  $\omega = \omega_E$ , as shown in the inset of Fig. 1, its effect on  $\sigma^L(q, \omega)$  is much more gradual because many optical transitions (initial and final states) are involved in the creation of a hole-particle pair, as depicted in Fig. 4. If we restrict our discussion to scattering processes in the vicinity of  $\omega = q$ , then for  $q < \omega_E$  these transitions will include initial and final states with energies always below  $\omega_E$  and therefore not sample the EPI scattering rate. For  $q > \omega_E$  the transitions will begin to sample states with energies both above and below  $|\omega_E|$  and therefore have an averaging of EPI scattering rates.

To conclude, we have calculated the effect of electron-phonon coupling on the finite momentum optical response of graphene with the aim of getting a first understanding of how this interaction modifies the bare band results. A Kubo formula is employed in the simplest bubble approximation,

IMPACT OF ELECTRON-PHONON COUPLING ON NEAR- . . .

PHYSICAL REVIEW B **87**, 045405 (2013)

which neglects vertex corrections but includes electron-phonon renormalizations in the Dirac fermion spectral density  $A(k, \omega)$ . In addition, there appears in the formula for the finite  $q$  conductivity an important scattering factor,  $F_{ss'}(\phi)$ , which incorporates chiral properties of the Dirac charge carriers associated with initial and final electronic states. As such, this factor depends in a fundamental way on the direction of  $q$  relative to the crystal lattice and direction of measurement. The conductivity in the  $x$  direction,  $\sigma_{xx}$ , for a general direction of momentum  $q$  can be decomposed into a linear combination of the longitudinal response for  $q$  scattering which occurs along the zigzag direction ( $k_x$ ) and a transverse part for  $q$  scattering along the armchair direction ( $k_y$ ). Here, a peak is identified in  $\sigma^L(q, \omega)$  which is directly related to the quasiparticle energy  $\epsilon^+(k_F - q)$  in the bare band case. The electron-phonon interaction is found to shift the position of this peak in energy and to broaden it. However, for values of  $q$  small enough that only optical transitions involving both initial and final states with energies well below the phonon energy  $\omega_E$  enter, the peaks in  $\sigma^L(q, \omega)$  still track perfectly those in the electron spectral function  $A(k, \omega)$  measured in ARPES, and both relate directly to the renormalized quasiparticle

energies  $\epsilon^+(k_F - q)/(1 + \lambda)$ . However, as the magnitude of  $q$  is increased, the quasiparticle dispersion curve starts to deviate significantly from linearity and exhibit a phonon kink. At this point quasiparticle and optics begin to deviate from each other. For example, optics shows no kink structure at  $\omega = \omega_E$ . Instead the phonon structure in  $\sigma^L(q, \omega)$  is found to have shifted to higher energies in the region of  $\omega \lesssim 2\omega_E$ . In this energy range, optical transitions involving a phonon kink in both initial and final states become possible, and this leads to deviations of the optical spectrum from linearity in analogy to the phonon kinks at  $\omega_E$  found in the renormalized Dirac fermion energies. In this case there is a contribution from other optical transitions which emphasize less phonon structure, and so the image of the phonon is not as sharp in optics as it is in ARPES. Finally, we found that at higher energies,  $\omega > \omega_E$ , the optical peaks continue to track well the renormalized energies  $\epsilon^+(k_F - q)/(1 + \lambda)$  while the quasiparticle peaks move instead toward their bare band values.

This research was supported in part by the Natural Sciences and Engineering Research Council of Canada and the Canadian Institute for Advanced Research.

\*jpfleblanc@gmail.com

<sup>1</sup>M. Orlita and M. Potemski, *Semicond. Sci. Technol.* **25**, 063001 (2010).<sup>2</sup>V. P. Gusynin, S. G. Sharapov, and J. P. Carbotte, *Phys. Rev. Lett.* **98**, 157402 (2007).<sup>3</sup>T. Ando, Y. Zheng, and H. Suzuura, *J. Phys. Soc. Jpn.* **71**, 1318 (2002).<sup>4</sup>V. P. Gusynin, S. G. Sharapov, and J. P. Carbotte, *New J. Phys.* **11**, 095013 (2009).<sup>5</sup>Z. Li, E. A. Henriksen, Z. Jiang, Z. Hao, M. C. Martin, P. Kim, H. L. Stormer, and D. N. Basov, *Nat. Phys.* **4**, 532 (2008).<sup>6</sup>N. M. R. Peres, T. Stauber, and A. H. Castro Neto, *EPL* **84**, 38002 (2008).<sup>7</sup>T. Stauber and N. M. R. Peres, *J. Phys.: Condens. Matter* **20**, 055002 (2008).<sup>8</sup>T. Stauber, N. M. R. Peres, and A. H. Castro Neto, *Phys. Rev. B* **78**, 085418 (2008).<sup>9</sup>J. P. Carbotte, E. J. Nicol, and S. G. Sharapov, *Phys. Rev. B* **81**, 045419 (2010).<sup>10</sup>R. E. Prange and L. P. Kadanoff, *Phys. Rev.* **134**, A566 (1964).<sup>11</sup>T. Mori, E. J. Nicol, S. Shizuka, K. Kuniyasu, T. Nojima, N. Toyota, and J. P. Carbotte, *Phys. Rev. B* **77**, 174515 (2008).<sup>12</sup>G. Li, A. Luican, and E. Y. Andrei, *Phys. Rev. Lett.* **102**, 176804 (2009).<sup>13</sup>B. Mitrovic and J. P. Carbotte, *Can. J. Phys.* **61**, 758 (1983).<sup>14</sup>B. Mitrovic and J. P. Carbotte, *Can. J. Phys.* **61**, 784 (1983).<sup>15</sup>E. Cappelluti and L. Pietronero, *Phys. Rev. B* **68**, 224511 (2003).<sup>16</sup>E. J. Nicol and J. P. Carbotte, *Phys. Rev. B* **80**, 081415(R) (2009).<sup>17</sup>A. Bostwick, T. Ohta, T. Seyller, K. Horn, and E. Rotenberg, *Nat. Phys.* **3**, 36 (2007).<sup>18</sup>S. Y. Zhou, D. A. Siegel, A. V. Fedorov, and A. Lanzara, *Phys. Rev. B* **78**, 193404 (2008).<sup>19</sup>M. Calandra and F. Mauri, *Phys. Rev. B* **76**, 205411 (2007).<sup>20</sup>C.-H. Park, F. Giustino, C. D. Spataru, M. L. Cohen, and S. G. Louie, *Phys. Rev. Lett.* **102**, 076803 (2009).<sup>21</sup>C.-H. Park, F. Giustino, C. D. Spataru, M. L. Cohen, and S. G. Louie, *Nano Lett.* **9**, 4234 (2009).<sup>22</sup>W.-K. Tse and S. Das Sarma, *Phys. Rev. Lett.* **99**, 236802 (2007).<sup>23</sup>Z. Fei, G. O. Andreev, W. Bao, L. M. Zhang, A. S. McLeod, C. Wang, M. K. Stewart, Z. Zhao, G. Dominguez, M. Thiemens, M. M. Fogler, M. J. Tauber, A. H. Castro-Neto, C. N. Lau, F. Keilmann, and D. N. Basov, *Nano Lett.* **11**, 4701 (2011).<sup>24</sup>Z. Fei, A. S. Rodin, G. O. Andreev, W. Bao, A. S. McLeod, M. Wagner, L. M. Zhang, Z. Zhao, M. Thiemens, G. Dominguez, M. M. Fogler, A. H. Castro Neto, C. N. Lau, F. Keilmann, and D. N. Basov, *Nature* **487**, 82 (2012).<sup>25</sup>J. Chen, M. Badioli, P. Alonso-González, S. Thonggrattanasiri, F. Huth, J. Osmond, M. Spasenović, A. Centeno, A. Pesquera, P. Godignon, A. Z. Elorza, N. Camara, F. J. G. de Abajo, R. Hillenbrand, and F. H. L. Koppens, *Nature* **487**, 77 (2012).<sup>26</sup>J. P. Carbotte, J. P. F. LeBlanc, and E. J. Nicol, *Phys. Rev. B* **85**, 201411(R) (2012).<sup>27</sup>B. Lundqvist, *Phys. Kondens. Mater.* **6**, 193 (1967).<sup>28</sup>E. Cappelluti and L. Benfatto, *Phys. Rev. B* **79**, 035419 (2009).<sup>29</sup>A. Scholz and J. Schliemann, *Phys. Rev. B* **83**, 235409 (2011).<sup>30</sup>C.-H. Park, F. Giustino, M. L. Cohen, and S. G. Louie, *Phys. Rev. Lett.* **99**, 086804 (2007).<sup>31</sup>C.-H. Park, F. Giustino, C. D. Spataru, M. L. Cohen, and S. G. Louie, *Nano Lett.* **8**, 4229 (2008).<sup>32</sup>F. Doğan and F. Marsiglio, *Phys. Rev. B* **68**, 165102 (2003).<sup>33</sup>P. E. C. Ashby and J. P. Carbotte, *Phys. Rev. B* **86**, 165405 (2012).

# Chapter 4

## The High $T_c$ cuprate superconductors

Superconductivity is a phenomenon that is characterized by zero resistance below some critical temperature,  $T_c$ . In the superconducting state the material also displays perfect diamagnetism, the screening of any applied magnetic fields. This expulsion of magnetic fields is known as the Meissner effect [17]. Superconductivity was first observed in 1911 in mercury by Kamerlingh Onnes [18]. At  $T \approx 4K$  the resistance abruptly disappeared. Ironically, he also observed the superfluid transition (the analogue of superconductivity for particles with no electric charge) of liquid helium in the same experiment. A search for more superconductors was spurred to try and understand the phenomenon. Superconductivity was consequently found in many metals and alloys, all at low temperatures.

Theoretical progress on superconductivity was slow, and not for a lack of effort. In the 1930's the London brothers put forward a phenomenological theory for the electromagnetic response of superconductors [19], which could account for the Meissner effect. Further theoretical progress did not come until the 1950's. In 1950 Ginzburg and Landau [20] put forward their phenomenological theory of superconductivity. This was an extension of Landau's theory of second order phase transitions to the superconducting state. In particular the Ginzburg Landau theory was an expansion for the free energy in terms of a complex order parameter. The theory worked remarkably well, but lacked a rigorous derivation. Furthermore, the identification of the order parameter with a physical quantity was not put forward in the original publication.

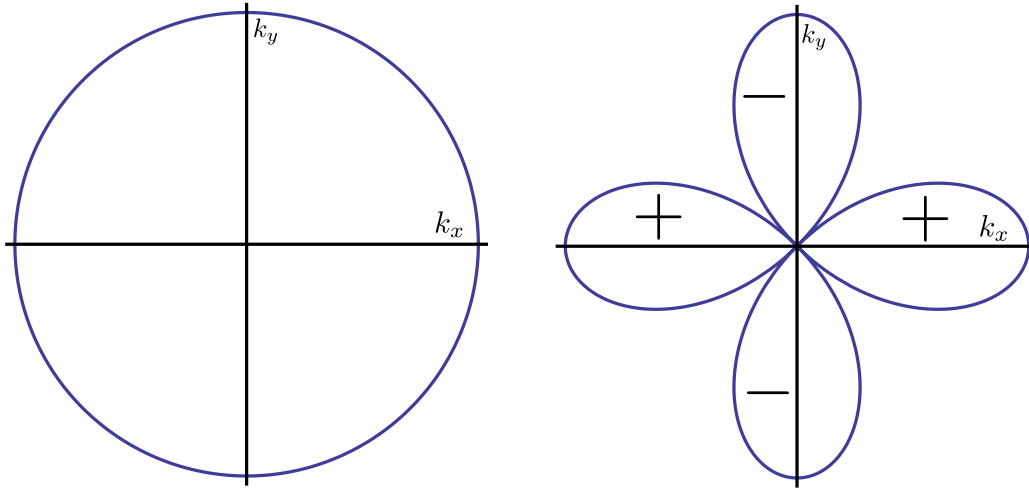


Figure 4.1: The momentum space structure of an  $s$ -wave (left) and  $d$ -wave (right) gap. The  $s$ -wave gap structure corresponds to that of the conventional superconductors. The high  $T_c$  cuprates are now known to have a  $d$ -wave gap. Since this gap vanishes at points in momentum space, there are low energy excitations about these points.

In 1957, Bardeen, Cooper, and Schrieffer [21] put forward the first microscopic theory of superconductivity (BCS theory). A few years earlier a paper by Cooper [22] had shown that the regular Fermi-liquid state was unstable in the presence of an attractive interaction. This instability leads to the formation of bound states of electrons, now known as Cooper pairs.

The BCS calculation started from a simplified electronic Hamiltonian and a trial wavefunction for the paired state. Using a variational method they found the best such wavefunction. In 1959, Gor'kov [23] showed that the Ginzburg Landau theory was a limiting case of the microscopic theory, close to the superconducting transition temperature,  $T_c$ . This identified the complex order parameter with the center of mass wavefunction of the Cooper pairs from the microscopic theory.

With the phase transition to the superconducting state comes the formation of an energy gap,  $\Delta$ . This gap is an energy cost for exciting quasiparticles from the ground state. In conventional superconductors, the attractive interaction is mediated by the electron-phonon interaction. In this case the attractive interaction occurs in the lowest angular momentum channel ( $s$ -wave), and the energy gap is isotropic. In 1965, a paper by Kohn and Luttinger [24] showed that a weak attractive interaction

can be generated through Coulomb repulsion. This attractive interaction appears in higher angular momentum channels. This opened up the door to the possibility of superconductors with non  $s$ -wave gaps.

Two different gaps are shown in Figure 4.1, the isotropic  $s$ -wave gap, and a gap with  $d_{x^2-y^2}$  symmetry. The former is relevant to the classic conventional superconductors, while the  $d$ -wave gap is of importance to the cuprate superconductors, as we will see in the next section. The fact that the  $d$ -wave gap vanishes at several points, means there are low energy quasiparticles at these nodes. Their signatures show up in thermodynamic and transport data.

## 4.1 The high- $T_c$ cuprate superconductors

In 1986 high temperature superconductivity was discovered by Bednorz and Muller [25]. Superconductivity was reported in Ba doped  $\text{La}_2\text{CuO}_4$  early in the year at  $T_c \approx 30\text{K}$ . The Meissner effect was confirmed later in the same year [26]. This observation was reproduced by many other groups and spurred a search for superconductivity in the oxide family. One year later Wu *et al.* [27] discovered high temperature superconductivity in  $\text{YBa}_2\text{Cu}_3\text{O}_7$  at  $92\text{K}$ . This pushed the realm of superconductivity above the boiling point of liquid nitrogen, a truly high temperature regime.

There are now many copper oxide materials that belong to the high temperature family. All of them have tetragonal crystal structure, or an orthorhombic structure, which is very nearly tetragonal. The common structural theme is the presence of copper oxygen planes ( $\text{CuO}_2$ ) in the  $ab$  plane separated by various spacing layers in the  $c$  direction. Transport is very weak along the  $c$  direction. Thus, the cuprates are often viewed as quasi-2D systems: a stack of weakly coupled 2D planes.

Common to the cuprate family is the famous phase diagram as a function of doping, shown in Figure 4.2. Near  $x = 0$  the cuprates are insulating anti-ferromagnets. Strong on-site Coulomb repulsion prevents placing more than one electron per copper site. The localized magnetic moments live on the copper site, alternating in direction. The anti-ferromagnetic order is rapidly suppressed ( $x \sim 0.03$ ) as a function of doping,  $x$ . Superconductivity emerges after the static anti-ferromagnetic order is fully suppressed,

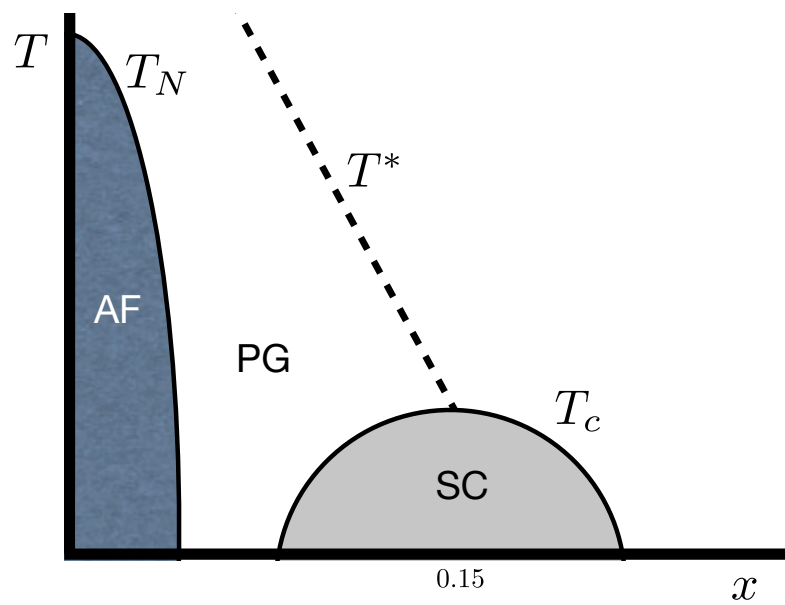


Figure 4.2: A cartoon version of the cuprate phase diagram. The parent compound is the anti-ferromagnetic phase (AF) pictured to the left. As hole doping,  $x$  is increased this static anti-ferromagnetic order is suppressed, eventually giving way to the superconducting dome (SC). Below the temperature  $T^*$  is the pseudogap (PG) phase.

although anti-ferromagnetic spin fluctuations still remain. The superconducting transition temperature increases with doping, to a maximum, known as ‘optimal doping’ ( $x \sim 0.15$ ). Beyond optimal doping the transition temperature decreases and the superconducting phase disappears at large dopings ( $x \sim 0.3$ ). The pseudogap phase is an anomalous state that exists below a temperature  $T^*$ . It is characterized by a partial gap in the excitation spectrum. There is no consensus as to the nature of the pseudogap state at this time. Since superconductivity condenses from this phase, a more complete understanding of pseudogap phase is believed to be essential to understanding the mechanism behind high temperature superconductivity. Above optimal doping, the normal state is non-Fermi liquid like and is commonly referred to as a ‘Strange metal’. It is most famously characterized by its DC resistivity which exhibits a linear temperature dependence. This temperature dependence is in sharp contrast to a normal Fermi-liquid whose resistivity goes like  $T^2$ . This Fermi-liquid behavior is recovered in the normal state of the cuprates at large doping.

## 4.2 Dirac quasiparticles

The cuprates are now known to be  $d$ -wave superconductors. Their gap function takes the form

$$\Delta_{\mathbf{k}} = 2\Delta_0(\cos(k_x) - \cos(k_y)), \quad (4.1)$$

where  $\Delta_0$  is the maximum value of the superconducting gap. Within a BCS mean field theory, the effective Hamiltonian is of the form

$$H = \sum_{\mathbf{k}, \sigma} (\epsilon_{\mathbf{k}} - \mu) c_{\sigma, \mathbf{k}}^\dagger c_{\sigma, \mathbf{k}} + \sum_{\mathbf{k}} \left( \Delta_{\mathbf{k}} c_{\uparrow, \mathbf{k}}^\dagger c_{\downarrow, -\mathbf{k}}^\dagger + \text{H.c.} \right), \quad (4.2)$$

where  $\epsilon_{\mathbf{k}}$  is the normal state dispersion. The quasiparticle excitation energies are given by

$$E_{\mathbf{k}} = \sqrt{(\epsilon_{\mathbf{k}} - \mu)^2 + \Delta_{\mathbf{k}}^2}. \quad (4.3)$$

Near the intersection of the Fermi surface and the nodes of  $\Delta_{\mathbf{k}}$ ,  $\epsilon_{\mathbf{k}} - \mu \approx v_F k_{\perp}$  and  $\Delta_{\mathbf{k}} \approx v_{\Delta} k_{\parallel}$ , where  $v_{\Delta} = \Delta_0/p_F$ , and  $k_{\perp}$  and  $k_{\parallel}$  are the wavevectors relative to the Fermi surface in the perpendicular and parallel directions. Thus the dispersion has the form

$$E_k = \sqrt{(v_F k_{\perp})^2 + (v_{\Delta} k_{\parallel})^2}, \quad (4.4)$$

which is an anisotropic Dirac dispersion. The anisotropy is controlled by the dimensionless number  $v_F/v_{\Delta}$ . Interestingly, these emergent Dirac Fermions are massless, and the Dirac node stays at zero energy even as the chemical potential is changed.

### 4.3 YRZ Green's function

The Yang, Rice and Zhang (YRZ) model for the underdoped cuprates is a phenomenological model aimed at understanding the pseudogap phase of the cuprate phase diagram. Presumably, an understanding of the pseudogap state will shed light on the mechanism responsible for High  $T_c$  superconductivity. The YRZ model has been able to qualitatively agree with many available experimental data. This agreement comes largely from the fact that the YRZ model naturally reconstructs the Fermi surface as the doping is changed. The motivation for the YRZ model comes from the study of doped spin-liquids. YRZ took the resonating valence bond gap to play the role of the pseudogap when they wrote down the form for the electronic propagator. In their model the gap appears on the surface where the umklapp scattering is strongest (the anti-ferromagnetic Brillouin zone). This gap eats away at the large Fermi surface at the intersection with the anti-ferromagnetic Brillouin zone leading to reconstructed Fermi pockets.

The YRZ model [28] for the underdoped cuprates begins with an ansatz for the coherent part of the single particle Green's function. Their ansatz was made by proposing a self energy analogous to one derived in the study of a doped spin liquid on two-leg Hubbard ladders by Konik *et al.* [29]. The self energy derived by Konik *et*

al. was of the form

$$\Sigma_a = \frac{\Delta^2}{\omega + \epsilon_a(\mathbf{k})}, \quad (4.5)$$

where  $\epsilon_a(\mathbf{k})$  is the half-filling energy in the two-leg ladder system. The YRZ ansatz for the self energy is of the same form

$$\Sigma_{pg} = \frac{\Delta_{pg}^2}{\omega + \xi_{\mathbf{k}}^0}, \quad (4.6)$$

where  $\Delta_{pg}$  is the pseudogap, and  $\xi_{\mathbf{k}}^0$  is the nearest neighbor hopping term, which defines the half-filled state at zero doping.

The YRZ Green's function is

$$G(\mathbf{k}, \omega) = \frac{g_t}{\omega - \xi_{\mathbf{k}} - \Delta_{pg}^2/(\omega + \xi_{\mathbf{k}}^0)} \quad (4.7)$$

$$= g_t \frac{\omega + \xi_{\mathbf{k}}^0}{\omega^2 - \omega\xi_{\mathbf{k}} + \omega\xi_{\mathbf{k}}^0 - \xi_{\mathbf{k}}\xi_{\mathbf{k}}^0 - \Delta_{pg}^2} \quad (4.8)$$

$$= g_t \frac{\omega + \xi_{\mathbf{k}}^0}{(\omega - E_{\mathbf{k}}^+)(\omega - E_{\mathbf{k}}^-)} \quad (4.9)$$

$$= g_t \left( \frac{W_{\mathbf{k}}^+}{\omega - E_{\mathbf{k}}^+} + \frac{W_{\mathbf{k}}^-}{\omega - E_{\mathbf{k}}^-} \right), \quad (4.10)$$

where  $g_t$  is a Gutzwiller renormalization factor,

$$E_{\mathbf{k}}^{\pm} = \frac{\xi_{\mathbf{k}} - \xi_{\mathbf{k}}^0}{2} \pm \sqrt{\tilde{\xi}_{\mathbf{k}}^2 + \Delta_{pg}^2}, \quad (4.11)$$

$$W_{\mathbf{k}}^{\pm} = \frac{1}{2} \left( 1 \pm \frac{\tilde{\xi}_{\mathbf{k}}}{E_{\mathbf{k}}^{\pm}} \right), \quad (4.12)$$

and  $\tilde{\xi}_{\mathbf{k}} = (\xi_{\mathbf{x}} + \xi_{\mathbf{k}}^0)/2$ .

To obtain the superconducting Green's function, one proceeds in the normal way, but taking the YRZ model as the normal state. From the above representation of the Green's function we can see that the YRZ ansatz for the self energy results in a

two-band model. Denoting the band index by  $\alpha = \pm$  we have

$$G_S^\alpha = g_t \frac{W_{\mathbf{k}}^\alpha}{\omega - E_{\mathbf{k}}^\alpha - \Delta_{\mathbf{k}}^2 / (\omega + E_{\mathbf{k}}^\alpha)} \quad (4.13)$$

$$= g_t \frac{W_{\mathbf{k}}^\alpha (\omega + E_{\mathbf{k}}^\alpha)}{(\omega - E_S^\alpha)(\omega + E_S^\alpha)}, \quad (4.14)$$

where  $E_S^\alpha = \sqrt{E_{\mathbf{k}}^2 + \Delta_{\mathbf{k}}^2}$ . This leads to the standard looking form for the Green's function for a superconductor in terms of  $u^\alpha = \sqrt{\frac{1}{2} \left(1 + \frac{E_{\mathbf{k}}^\alpha}{E_S^\alpha}\right)}$  and  $v^\alpha = \sqrt{\frac{1}{2} \left(1 - \frac{E_{\mathbf{k}}^\alpha}{E_S^\alpha}\right)}$ :

$$G_S^\alpha = g_t W_{\mathbf{k}}^\alpha \left( \frac{u_{\mathbf{k}}^{\alpha 2}}{\omega - E_S^\alpha} + \frac{v_{\mathbf{k}}^{\alpha 2}}{\omega + E_S^\alpha} \right) \quad (4.15)$$

From here the spectral functions required for the Kubo formula can be obtained using the usual relation  $A(\mathbf{k}, \omega) = -2\text{Im}G(\mathbf{k}, \omega + i0^+)$ .

For superconductivity the anomalous Green's function  $F(\mathbf{k}, t) = -i \langle \mathcal{T} c_{\uparrow \mathbf{k}}(t) c_{\downarrow -\mathbf{k}}(0) \rangle$  acquires a non-zero value and is important in determining the conductivity. Adding a band index to the usual formula for  $F$  gives

$$F^{\alpha \mathbf{k}, \omega} = -\frac{\Delta_{\mathbf{k}}}{\omega + E_{\mathbf{k}}^\alpha} G_S^\alpha(\mathbf{k}, \omega) \quad (4.16)$$

$$= g_t W_{\mathbf{k}}^\alpha \frac{\Delta_{\mathbf{k}}}{2E_S^\alpha} \left( \frac{1}{\omega + E_S^\alpha} - \frac{1}{\omega - E_S^\alpha} \right). \quad (4.17)$$

The corresponding anomalous spectral function required for the conductivity follows from  $B(\mathbf{k}, \omega) = -2\text{Im}F(\mathbf{k}, \omega + i0^+)$ .

## 4.4 Luttinger's theorem

In the mid 1950's Landau [30] formulated the ideas behind Fermi-liquid theory. The principles of Fermi liquid theory form the basis of traditional condensed matter theory. The key concept is that the thermodynamic and kinetic properties for the low energy excitations in an interacting Fermion system are described by free Fermions. To understand Fermi liquid theory we can consider a non-interacting system labeled

by some set of occupation numbers. The assumption of Fermi liquid theory is that as we turn on interactions, the free fermion states adiabatically change into the full interacting states labeled by the same occupation numbers. That is, there is a one-to-one mapping between the interacting and the non-interacting problems. As one goes to the interacting problem certain quantities, such as the quasiparticle mass,  $m$ , may change. The properties that we measure in the lab depend on this effective mass. These concepts underpin our description of all metals. We have also been able to understand other states of matter, like superconductivity, as an instability of the Fermi liquid state.

In 1960, Luttinger [31] gave a proof relating to Landau's conjecture. His proof established a relationship between the particle density  $n = N/V$  and the Fermi-liquid excitations. Interestingly the Luttinger theorem is not bounded by the restrictions of Fermi liquid theory and can be applied to systems without sharply defined quasiparticles. The proof relies on the analytic properties of the Green's function in the complex plane. For details on the proof, please see page 166 in Abrikosov, Gorkov and Dzyaloshinski [32].

In  $d$ -dimensions Luttinger's theorem reads

$$n = 2 \int_{G(\mathbf{k},0) > 0} \frac{d^d k}{(2\pi)^d}. \quad (4.18)$$

The integration region is over the region where the Green's function at  $\omega = 0$  is positive. The Green's function may only change sign at its zeroes or its poles. The poles of the Green's function specify the Fermi surface. The zeroes of the Green's functions define a Luttinger surface. In the case of Fermi-liquid theory this relation tells us that the density is equal to the number of states below the Fermi surface. The YRZ Green's function also has zeros, and we use this relation to determine the chemical potential as we change our doping in our calculations.

## 4.5 Paper III – Resonating valence bonds and Fermi surface reconstruction: Resistivity in the underdoped cuprates

Reprinted with permission as follows: Phillip E.C. Ashby and J.P. Carbotte “*Resonating valence bonds and Fermi surface reconstruction: Resistivity in the underdoped cuprates*” Phys. Rev. B **87** 014514 (2013). Copyright (2013) by the American Physical Society.

The pseudogap phase of the underdoped cuprates has remained mysterious since its discovery. In this paper we employed a model of the underdoped cuprates with the aim of studying the resistivity along both the c-axis as well as in the ab-plane. We focused on the resistivity in the pseudogap phase only. It is known that the resistivity is metallic-like in the ab-plane, and insulating-like along the c-direction. In our paper we use a coherent tunneling terms to describe c-axis transport. We compared our findings qualitatively with those of experiments on the cuprates and found good agreement. This result is very interesting, since one might naively think that coherent tunneling would lead to a metallic-like response. This work was largely motivated by two factors. One was the success of the YRZ model in its applications to other properties of the underdoped cuprates. The second was a paper by Levchenko and Norman [33], that presented a simple calculation for the resistivity and Hall coefficient. We also compared our findings with an arc-model for the cuprates, which we argue is a phenomenological limit of the YRZ model.

PHYSICAL REVIEW B 87, 014514 (2013)

**Resonating valence bonds and Fermi surface reconstruction: Resistivity in the underdoped cuprates**

 Phillip E. C. Ashby<sup>1,\*</sup> and J. P. Carbotte<sup>1,2,†</sup>
<sup>1</sup>*Department of Physics and Astronomy, McMaster University, Hamilton, Ontario, Canada L8S 4M1*
<sup>2</sup>*The Canadian Institute for Advanced Research, Toronto, Ontario, Canada M5G 1Z8*

(Received 5 November 2012; revised manuscript received 14 January 2013; published 28 January 2013)

The pseudogap phase of the underdoped cuprates is the host to a variety of novel electronic phenomenon. An example is the dc resistivity that shows metallic behavior in the  $ab$  plane, while the  $c$ -axis response is insulating. We apply a model, originally formulated by Yang, Rice, and Zhang [Phys. Rev. B 73, 174501 (2006)], to study the resistivity in the pseudogap phase. This model is able to reproduce the qualitative features of the resistivity, including the systematic deviations from linear behavior for the in-plane conductivity, and the insulating behavior along the  $c$  axis. We compare this to the predictions of the arc model and find similar qualitative behavior. We find that the most important element in understanding the resistivity is the reconstruction of the Fermi surface, which puts strong restrictions on the number of quasiparticles allowed to participate in dc transport.

 DOI: [10.1103/PhysRevB.87.014514](https://doi.org/10.1103/PhysRevB.87.014514)

PACS number(s): 74.72.Kf, 74.20.Mn, 74.25.F–

The pseudogap is the precursor phase from which high- $T_C$  superconductivity condenses in the underdoped cuprates. Understanding the pseudogap phase is believed to be central for deducing the mechanism that underpins high- $T_C$  superconductivity.<sup>1</sup> To study the low-lying excitations in this phase, it is essential to understand the character of its Fermi surface (FS). Photoemission [angle-resolved photoemission spectroscopy (ARPES)] in the pseudogap phase observes segments of FS along the Brillouin zone (BZ) diagonals. These segments were originally interpreted as disconnected segments of FS and became known as Fermi arcs.<sup>2</sup> Recently, they have been resolved as pockets with small spectral weight along the antiferromagnetic Brillouin zone (AFBZ) boundary.<sup>3</sup> Evidence for pockets is compounded by the observation of quantum oscillations, which requires a closed FS.<sup>4</sup> The nature of the FS reconstruction in the pseudogap phase has been the subject of much debate and has led to a number of theoretical proposals.

One class of theories of the pseudogap phase involves competing order parameters whose fluctuations serve to reconstruct the FS into the observed pockets. These models involve broken translational symmetry, such as charge- or spin-density waves. Other theories of the pseudogap begin from the idea of preformed Cooper pairs that lack off-diagonal long-range order.<sup>5</sup> Indeed, superconducting fluctuations have been seen to exist above  $T_C$  in the form of a disordered vortex liquid.<sup>6</sup> However, these fluctuations fail to persist to the temperature scale associated with pseudogap behavior.<sup>7</sup> An alternative approach is that the pseudogap arises naturally as one dopes a Mott insulator, which then leads to both insulating and strongly correlated electronic behavior.<sup>8</sup> This was the approach that Yang, Rice, and Zhang adopted when they put forth their model of the underdoped cuprates in 2006.<sup>9</sup>

The Yang-Rice-Zhang (YRZ) model consists of an ansatz for the coherent piece of the single-particle Green's function in the pseudogap phase. It is based on results for Anderson's resonating valence bond (RVB) spin liquid.<sup>10,11</sup> In this description, as the Mott insulating state is approached a gap opens on the AFBZ boundary. This gap is an RVB spin gap and appears as an energy scale separate from superconductivity.

Since its debut, the YRZ model has been shown to capture many properties of the cuprates that were considered anomalous. In particular, it has been shown to give good agree-

ment with Raman spectra,<sup>12,13</sup> ARPES,<sup>3,14</sup> specific heat,<sup>15</sup> penetration depth,<sup>16</sup> and tunneling spectroscopy.<sup>17</sup> Perhaps most remarkably is that the YRZ model captures all of this behavior with doping as the only free parameter.

A related model, the arc model, has also been shown to capture the qualitatively correct behavior in the underdoped cuprates.<sup>13,15,16</sup> In this model, a gap is placed on the antinodal portion of the metallic Fermi surface, leaving Fermi arc segments. The length of the remaining FS serves the same role doping does in the YRZ model. Thus it seems that the qualitative behavior of many of these experiments can be captured by any model that gives the disappearance of FS along the antinodal direction.

Both the arc model and the YRZ model contain reconstructed holelike Fermi surfaces along the nodal direction. One might wonder if this is in contradiction to the experiments that show electronlike transport properties. In fact, a recent paper has shown that bilayer charge ordering can further reconstruct a nodal FS into a FS of electronlike pockets.<sup>18</sup>

In this paper we compute the in-plane ( $ab$ ) and out-of-plane ( $c$ -axis) resistivity using both the YRZ model and the arc model for the pseudogap phase of the underdoped cuprates. This calculation is of an essentially different character than the previous studies, as it requires us to add ingredients not present in the initial formulation of the YRZ model. Specifically, the resistivity relies on the scattering rate and the extension to the  $c$ -axis needs some assumption to be made about the interlayer tunneling matrix element. After adding these ingredients we show that the YRZ and arc models agree qualitatively with dc-transport experiments. Although these two models have different underlying physics, they give qualitatively similar predictions for the resistivity in the underdoped cuprates.

*The YRZ model.* The YRZ ansatz for the coherent part of the electron Green's function for a doping  $x$  is

$$G(\mathbf{k}, \omega) = \frac{g_t}{\omega - \xi(\mathbf{k}) - \Delta_{\text{PG}}^2 / [\omega + \xi^0(\mathbf{k})]}, \quad (1)$$

where  $g_t = 2x/(1+x)$  is a Gutzwiller renormalization factor,  $\xi(\mathbf{k}) = \xi^0(\mathbf{k}) - 4t'(x)\cos(k_x)\cos(k_y) - 2t''(x)[\cos(2k_x) + \cos(2k_y)] - \mu_p$  is the tight-binding dispersion on a square lattice out to third-nearest neighbors, and  $\xi^0(\mathbf{k}) = -2t(x)[\cos(k_x) + \cos(k_y)]$  is the first-nearest-neighbor term.

PHILLIP E. C. ASHBY AND J. P. CARBOTTE

PHYSICAL REVIEW B 87, 014514 (2013)

Here  $\mu_p$  is a chemical potential determined from the Luttinger sum rule. The RVB gap  $\Delta_{\text{PG}}$  plays the role of the pseudogap and has  $d$ -wave symmetry, i.e.,  $\Delta_{\text{PG}} = \Delta_0(1 - x/x_c)$  [ $\cos(k_x) - \cos(k_y)$ ]. We use values for all parameters in the YRZ model as they appear in the original YRZ paper.<sup>9</sup> We work in units where  $\hbar = k_B = 1$  and all energies are measured in units of  $t_0$ .

Equation (1) would be the Green's function for a superconductor if  $\xi^0(\mathbf{k}) = \xi(\mathbf{k})$ . This difference causes the gap to open on the surface defined by  $\xi^0(\mathbf{k})$ , which in our case is the AFBZ. This gap naturally reconstructs the large FS into pockets and can give rise to an interesting electronic response. Given this Green's function, we can compute the conductivity and hence the resistivity.

The dc conductivity is given by the Kubo formula

$$\sigma_{ij} = -\lim_{\omega \rightarrow 0} \left[ \frac{\text{Im}[\Pi_{ij}(\omega)]}{\omega} \right]. \quad (2)$$

The current-current correlation function  $\Pi_{ij}(\omega)$  is evaluated at the one-loop level

$$\Pi_{ij}(\omega) = e^2 T \sum_{\mathbf{k}, \nu_n} [v_i(\mathbf{k}) G(\mathbf{k}, \nu_n) v_j(\mathbf{k}) G(\mathbf{k}, \omega + \nu_n)], \quad (3)$$

where  $v_i$  is the  $i$ th component of the velocity and the  $\nu_n$  are Matsubara frequencies. For the  $ab$  conductivity we use  $v_x = d\xi(\mathbf{k})/dk_x$ . For the  $c$ -axis conductivity, we replace  $v^2$  with  $t_{\perp}^2(\mathbf{k})d^2$ , where  $d$  is the interlayer distance and  $t_{\perp}(\mathbf{k}) = t_{\perp}[\cos(k_x) - \cos(k_y)]^2$  is the interlayer tunneling matrix element. This matrix element was first suggested by Anderson.<sup>19</sup> It was used in the nodal liquid model of the cuprates, which reproduced the insulatinglike behavior associated with the pseudogap.<sup>20</sup> The final component that we need to compute the conductivity is the scattering rate  $\Gamma$ , which broadens the spectral densities. To correspond with experiments we follow the suggestion of Ito *et al.*<sup>21</sup> and take a temperature-dependent scattering rate. For our calculations we include a small residual scattering and take  $\Gamma = 0.01 + 2\pi\lambda T$ , with  $\lambda = 0.3$ . These choices leave us with doping as our only tunable parameter.

Figure 1 shows the in-plane and out-of-plane resistivities as a function of temperature for a few values of doping. The qualitative agreement with experiments<sup>21,22</sup> is good for both the in-plane and out-of-plane results. At high temperatures the in-plane resistivity is linear. As the pseudogap opens (moving down in doping), there is a progressively larger deviation from the linear behavior. This deviation from linearity is a loss of metallicity associated with the shrinking of the FS. The  $c$ -axis resistivity shows strong insulating behavior at low values of doping and becomes increasingly metallic as optimal doping is approached, just as in the experiments.

To understand these results, we found it instructive to introduce a joint density of states (JDOS). The JDOS can be thought of as a reference function that captures the effect of the pseudogap. This function is shown for the optimally doped and underdoped cases in Fig. 2 for the  $c$  axis. The only difference in the JDOS between the  $ab$ - and  $c$ -axis conductivities is the factor  $[\cos(k_x) - \cos(k_y)]^2$  from the tunneling matrix element. This factor suppresses the spectral density near zero frequency.

At optimal doping the JDOS contains only a single peak and the dependence on the resistivity is controlled solely by the thermal factors appearing in the evaluation of Eq. (3).

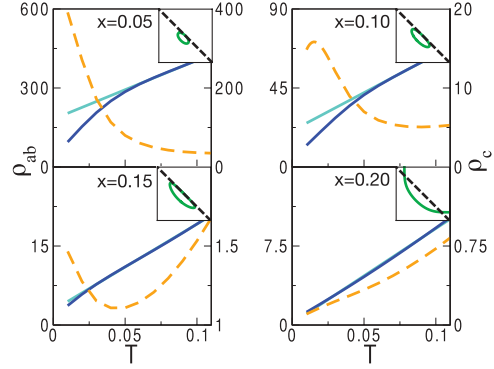


FIG. 1. (Color online) In-plane (solid blue curve, in units  $e^{-2}d$ ) and  $c$ -axis (dashed orange curve, in units  $e^{-2}t_{\perp}^{-2}d^{-1}$ ) resistivities as a function of temperature in the YRZ model for dopings  $x = 0.05, 0.10, 0.15,$  and  $0.2$ . The solid light blue lines are fits to the linear  $T$  region. The  $c$ -axis resistivity shows insulatinglike behavior and the in-plane resistivity shows a systematic deviation from linearity induced by the pseudogap energy scale. The insets show the Fermi surfaces (shown for one-quarter of the BZ-AFBZ boundary indicated by the dashed line) given by the YRZ Green's function.

Explicitly, the thermal factors are given by  $-df/d\omega$ , where  $f = 1/[1 + \exp(\omega/T)]$  is the Fermi function. At low temperatures, when the thermal factors are more sharply peaked, we get a higher conductivity and hence a lower resistivity. As we increase the temperature the thermal factors broaden and we get a smaller conductivity (larger resistivity). The underdoped case is more interesting. In the underdoped case

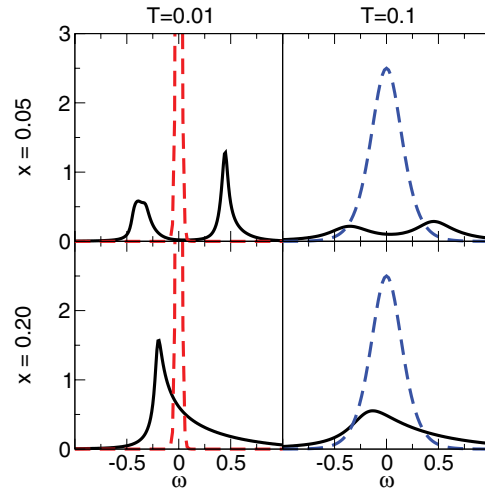


FIG. 2. (Color online) Joint density of states involved in the conductivity calculation for  $x = 0.05$  (highly underdoped) and  $x = 0.20$  (optimal doping) at low and high temperatures. The red dashed curves are the thermal factors for the low-temperature case and have peak height  $\approx 25$ . The blue dashed curves are the thermal factors for the high- $T$  case. As the JDOS becomes more flat (pseudogap fingerprint blurred out) we return to a more metalliclike behavior.

the opening of the pseudogap causes the peak to split into two pieces, separated by an energy on the order of the gap scale. The thermal factors behave as before, but there is no spectral weight remaining in the low- $T$  case. This gapping of the region near  $\omega = 0$  naturally gives insulating behavior. As the temperature is increased the JDOS broadens due to increased scattering and our resistivity falls back down accordingly. Within the YRZ model the resistivity is determined by this interplay between thermal factors and the structure of the density of states coming from the pseudogap.

*The arc model.* We now turn our attention to a model that can be thought of as a phenomenological version of the YRZ model, namely, the arc model. The arc model can be derived from the YRZ model through a series of approximations. This was first done by Leblanc and co-workers.<sup>15,16</sup> The procedure is as follows. In Eq. (1) we take  $\xi(\mathbf{k}) = \xi^0(\mathbf{k})$ . We then take the dispersions to be of the continuum form, that is,  $\xi(\mathbf{k}) = \frac{\hbar^2}{2m^*}k^2 - \mu \equiv \epsilon$ . Then  $\frac{d^2k}{(2\pi)^2} = Nd\epsilon \frac{d\theta}{2\pi}$ , where  $N$  is the density of states. Note that we have absorbed the Gutzwiller factor  $g_f$  into the density of states. From the symmetry in the problem we may also take the angular integration to be over one-eighth of the Brillouin zone, that is,  $0 \leq \theta \leq \pi/4$ . Finally we place a pseudogap  $\Delta$  on the FS starting from the antinodal direction. The amount gapped out is parametrized by an angle  $\theta_c$ . Specifically, in angular coordinates, the Green's function is given by

$$-\text{Im}[G(\epsilon, \theta)] = \begin{cases} \frac{\Gamma}{\epsilon^2 + \Gamma^2 + \Delta^2 \cos^2(2\theta)}, & 0 \leq \theta \leq \theta_c \\ \frac{\Gamma}{\epsilon^2 + \Gamma^2}, & \theta_c < \theta \leq \frac{\pi}{4}. \end{cases} \quad (4)$$

The Kubo formula for the conductivity is

$$\sigma = \frac{e^2 N}{\pi d} \int d\epsilon \frac{d\theta}{\pi/4} v_{k_x}^2 [\text{Im}[G(\epsilon, \theta)]]^2. \quad (5)$$

For the  $ab$  plane we take  $v_{k_x} = v_F$  to be an isotropic Fermi velocity. For the  $c$  axis we make the same replacement as before,  $v^2 \rightarrow d^2 t_{\parallel}^2 \cos^4(2\theta)$ .

The integrations over  $\epsilon$  and  $\theta$  can be carried out analytically. There are two contributions to the conductivity: a free-electron part  $\sigma_{\text{arc}}$  from the remaining FS and an interband part  $\sigma_{\Delta}$  from the gapped region of the FS. We obtain (units as in Fig. 3)  $\sigma^{(ab)} = \sigma_{\text{arc}}^{(ab)} + \sigma_{\Delta}^{(ab)}$  and  $\sigma^{(c)} = \sigma_{\text{arc}}^{(c)} + \sigma_{\Delta}^{(c)}$  with

$$\sigma_{\text{arc}}^{(ab)} = \frac{2}{\Gamma} \left( \frac{\pi}{4} - \theta_c \right), \quad (6)$$

$$\sigma_{\Delta}^{(ab)} = \frac{\lambda}{\Delta} \left( E(2\theta_c|\lambda^2) - \frac{\lambda^2}{2} \frac{\sin(4\theta_c)}{\sqrt{1 - \lambda^2 \sin^2(2\theta_c)}} \right), \quad (7)$$

$$\sigma_{\text{arc}}^{(c)} = \frac{1}{\Gamma} \left[ \frac{3}{4} \left( \frac{\pi}{4} - \theta_c \right) - \frac{1}{4} \sin(4\theta_c) - \frac{1}{32} \sin(8\theta_c) \right], \quad (8)$$

$$\sigma_{\Delta}^{(c)} = \frac{\lambda \Gamma^4}{\Delta^5} \left[ \left( 2 + \frac{\Delta^2}{\Gamma^2} \right) E(2\theta_c|\lambda^2) - 2F(2\theta_c|\lambda^2) - \frac{\lambda^2}{2} \frac{\sin(4\theta_c)}{\sqrt{1 - \lambda^2 \sin^2(2\theta_c)}} \right], \quad (9)$$

where  $\lambda = \Delta/\sqrt{\Delta^2 + \Gamma^2}$ ,  $F(x|\lambda^2)$  is the incomplete elliptic integral of the first kind, and  $E(x|\lambda^2)$  is the incomplete elliptic integral of the second kind.

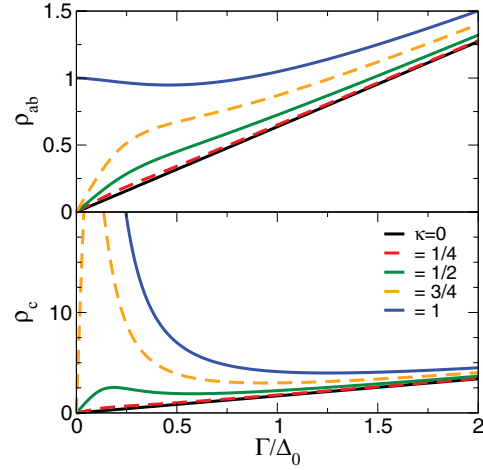


FIG. 3. (Color online) In-plane resistivity (units of  $\frac{d\pi\Delta_0}{e^2 N v_F^2}$ , where  $N$  is the density of states at the Fermi energy and  $v_F$  is the Fermi velocity) and  $c$ -axis resistivity (units of  $\frac{\pi\Delta_0}{e^2 N d t_{\parallel}^2}$ ) in the arc model for dimensionless pairing strengths  $\kappa = 0, 0.25, 0.5, 0.75$ , and  $1$ .

Unlike in the YRZ model, in the arc model the arc length is independent of the magnitude of the pseudogap. To correspond with the experiments and the YRZ model we chose to trade  $\theta_c$  for a new dimensionless variable  $\kappa = \Delta/\Delta_0$ , where  $\Delta_0$  is the magnitude of the pseudogap at 0 doping. The relationship between the strength of the pseudogap and doping can be found at the beginning of the section on the YRZ model. In principle, the function  $\theta_c(\kappa)$  is a strictly increasing function of  $\kappa$  that could be obtained by fitting the arc model to experimental data, if one desired. To highlight the essential features, and for simplicity, we chose  $\theta_c = \kappa\pi/4$ . The resulting curves are shown in Fig. 3. Since the scattering rate  $\Gamma \propto T$ , the  $x$  axis may be read as temperature.

Although the precise details of the curves differ from both the YRZ model and the experiments, the broad features are still captured by this simple model. The in-plane resistance is linear at high  $T$  and shows systematically larger deviations as the pairing strength is increased. The case  $\kappa = 1$  is distinct from the other cases and corresponds to the universal limit first discussed by Lee.<sup>23</sup> The  $c$ -axis resistivity shows progressively insulating behavior as we proceed further into the underdoped regime. This is due to the loss of FS along the antinodal direction. The  $c$ -axis tunneling matrix element is then responsible for getting rid of the remaining (nodal) states, which leads to an insulatinglike behavior.

The results of the arc model can be understood simply as a two-oscillator model: one Drude oscillator centred at  $\omega = 0$  and a displaced oscillator at  $\omega = \Delta$ . The dc conductivity is the value from these two contributions at  $\omega = 0$ . As the scattering rate is increased these two contributions broaden. At first, the broadening causes a decrease in the conductivity as the Drude peak comes down. This continues until the displaced peak at the gap energy leaks into the  $\omega = 0$  region, leading to a gain in conductivity. The conductivity then tends to decrease as the peaks broaden further. This explains the weak

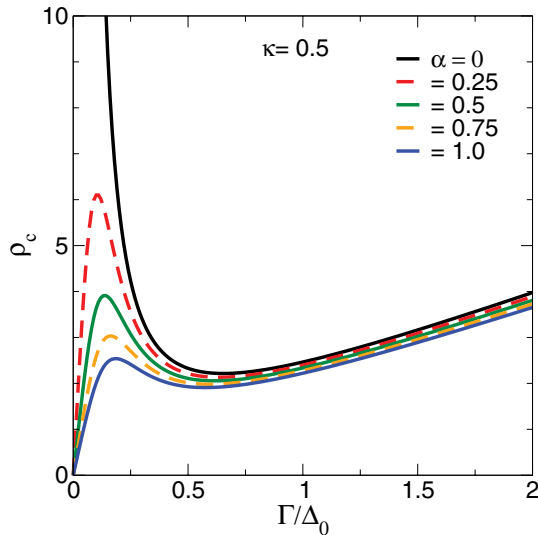


FIG. 4. (Color online) The  $c$ -axis resistivity with the weight given by the remaining FS as a tunable parameter  $\alpha$ . Specifically,  $\alpha$  enters as  $\alpha\sigma_{\text{arc}}^{(c)} + \sigma_{\Delta}^{(c)}$ . This figure shows how the FS contributes to the  $c$ -axis conductivity. The FS still gives an important contribution to the resistivity, even though the tunneling matrix element gaps out the nodal excitations.

maxima seen in both the  $ab$ -plane and the  $c$ -axis resistivity (Fig. 3). To show the two contributions explicitly we weighted the FS contribution to the conductivity by a parameter  $0 \leq \alpha \leq 1$  (Fig. 4). As we weaken the Drude component of the conductivity, the sample becomes increasingly more

resistive. This depletion of the remaining quasiparticles is precisely the same physics behind the resistive behavior coming from the  $c$ -axis tunneling matrix element.

In conclusion, we have found that the YRZ model of the pseudogap state with a linear in temperature scattering rate naturally reproduces the resistivity seen in this phase. A simpler model, the arc model, was also shown to possess qualitatively correct features of the resistivity. In the YRZ model, it was the interplay between thermal factors and a density of states that was responsible for the behavior of the resistivity. In contrast, the density of states in the arc model is constant and temperature only entered through the scattering rate. However, owing to the two distinct contributions to the conductivity, the arc model still showed qualitatively correct features.

Two elements in the YRZ calculation are vital for the agreement with experimental resistivity. First is the reconstruction of the FS as a function of doping. This reconstruction reduces the number of quasiparticles available for dc transport as the Mott insulating phase is approached. The second element is the tunneling matrix element. This matrix element effectively removes the remaining nodal quasiparticles and leaves an insulating response. The fact that FS reconstruction is so important allows us to understand why the arc model can do well, despite lacking all of the microscopic elements of the YRZ model. Indeed, one can think of the arc model as a phenomenological version of the YRZ model, where one is willing to ignore the mechanisms behind the reconstruction of the FS. Nevertheless, the arc model can still be used to help deduce the underlying physics and provides simple analytical results that are of great use.

The authors thank the Natural Sciences and Engineering Research Council of Canada and the Canadian Institute for Advanced Research for financial support.

<sup>\*</sup>ashbype@mcmaster.ca

<sup>†</sup>carbotte@mcmaster.ca

<sup>1</sup>T. Timusk and B. Statt, *Rep. Prog. Phys.* **62**, 61 (1999).

<sup>2</sup>A. Kanigel, U. Chatterjee, M. Randeria, M. R. Norman, S. Souma, M. Shi, Z. Z. Li, H. Raffy, and J. C. Campuzano, *Phys. Rev. Lett.* **99**, 157001 (2007).

<sup>3</sup>H. B. Yang, J. D. Rameau, Z. H. Pan, G. D. Gu, P. D. Johnson, H. Claus, D. G. Hinks, and T. E. Kidd, *Phys. Rev. Lett.* **107**, 047003 (2011).

<sup>4</sup>N. Doiron-Leyraud, C. Proust, D. LeBoeuf, J. Levallois, J.-B. Bonnemaison, R. Liang, D. A. Bonn, W. N. Hardy, and L. Taillefer, *Nature (London)* **447**, 565 (2007).

<sup>5</sup>M. R. Norman, A. Kanigel, M. Randeria, U. Chatterjee, and J. C. Campuzano, *Phys. Rev. B* **76**, 174501 (2007).

<sup>6</sup>Z. A. Xu, N. P. Ong, Y. Wang, T. Kakeshita, and S. Uchida, *Nature (London)* **406**, 486 (2000).

<sup>7</sup>L. Li, Y. Wang, S. Komiyama, S. Ono, Y. Ando, G. D. Gu, and N. P. Ong, *Phys. Rev. B* **81**, 054510 (2010).

<sup>8</sup>P. A. Lee, N. Nagaosa, and X.-G. Wen, *Rev. Mod. Phys.* **78**, 17 (2006).

<sup>9</sup>K.-Y. Yang, T. M. Rice, and F.-C. Zhang, *Phys. Rev. B* **73**, 174501 (2006).

<sup>10</sup>P. W. Anderson, *Science* **235**, 1196 (1987).

<sup>11</sup>F. C. Zhang, C. Gros, T. M. Rice, and H. Shiba, *Supercond. Sci. Technol.* **1**, 36 (1988).

<sup>12</sup>B. Valenzuela and E. Bascones, *Phys. Rev. Lett.* **98**, 227002 (2007).

<sup>13</sup>J. P. F. LeBlanc, J. P. Carbotte, and E. J. Nicol, *Phys. Rev. B* **81**, 064504 (2010).

<sup>14</sup>K.-Y. Yang, H. B. Yang, P. D. Johnson, T. M. Rice, and F.-C. Zhang, *Europhys. Lett.* **86**, 37002 (2009).

<sup>15</sup>J. P. F. LeBlanc, E. J. Nicol, and J. P. Carbotte, *Phys. Rev. B* **80**, 060505 (2009).

<sup>16</sup>J. P. Carbotte, K. A. G. Fisher, J. P. F. LeBlanc, and E. J. Nicol, *Phys. Rev. B* **81**, 014522 (2010).

<sup>17</sup>K.-Y. Yang, K. Huang, W.-Q. Chen, T. M. Rice, and F.-C. Zhang, *Phys. Rev. Lett.* **105**, 167004 (2010).

<sup>18</sup>N. Harrison and S. E. Sebastian, *New J. Phys.* **14**, 095023 (2012).

<sup>19</sup>S. Chakravarty, A. Sudbø, P. W. Anderson, and S. Strong, *Science* **261**, 337 (1993).

<sup>20</sup>A. Levchenko, T. Micklitz, M. R. Norman, and I. Paul, *Phys. Rev. B* **82**, 060502 (2010).

<sup>21</sup>T. Ito, K. Takenaka, and S. Uchida, *Phys. Rev. Lett.* **70**, 3995 (1993).

<sup>22</sup>K. Takenaka, K. Mizuhashi, H. Takagi, and S. Uchida, *Phys. Rev. B* **50**, 6534 (1994).

<sup>23</sup>P. A. Lee, *Phys. Rev. Lett.* **71**, 1887 (1993).

## 4.6 Paper IV – c-axis optical conductivity from the Yang-Rice-Zhang model of the underdoped cuprates

Reprinted with permission as follows: Phillip E.C. Ashby and J.P. Carbotte “*c-axis optical conductivity from the Yang-Rice-Zhang model of the underdoped cuprates*” Phys. Rev. B **87** 0184514 (2013). Copyright (2013) by the American Physical Society.

This work is an another application of the YRZ model to the underdoped cuprates. We present results on the dynamical conductivity for the c-axis which we compare with results for the ab-plane. In this paper we investigated both the pseudogap as well as the superconducting phases. We focused on c-axis properties since the c-axis data tends to show pseudogap features more clearly than the in-plane data. By including coherent interlayer tunneling we were able to study the c-axis behavior. Our findings were an explanation for a peak observed in infrared spectroscopy. This peak was previously explained by invoking an interlayer collective mode, but it appears naturally in the YRZ model. We also compared our calculations to microwave conductivity and found that the scattering rate was best described by a  $T^3$  law.

PHYSICAL REVIEW B 87, 184514 (2013)

***c*-axis optical conductivity from the Yang-Rice-Zhang model of the underdoped cuprates**

Phillip E. C. Ashby\*

*Department of Physics and Astronomy, McMaster University, Hamilton, Ontario, Canada L8S 4M1*

J. P. Carbotte†

*Department of Physics and Astronomy, McMaster University, Hamilton, Ontario, Canada L8S 4M1  
and The Canadian Institute for Advanced Research, Toronto, Ontario, Canada M5G 1Z8*

(Received 13 February 2013; revised manuscript received 9 April 2013; published 31 May 2013)

The *c*-axis optical response of the underdoped cuprates is qualitatively different from its in-plane counterpart. The features of the pseudogap show themselves more prominently in the *c*-axis than in-plane. We compute both the *c*-axis optical conductivity and the in-plane optical conductivity using the Yang-Rice-Zhang model of underdoped cuprates. This model combined with coherent interlayer tunneling is enough to explain the qualitative differences between the in-plane data and the *c*-axis data. We show how pseudogap features manifest themselves in the infrared and microwave conductivity within this model.

DOI: 10.1103/PhysRevB.87.184514

PACS number(s): 74.72.Gh, 74.25.Gz, 74.20.De

**I. INTRODUCTION**

The nature of the pseudogap phase in the underdoped cuprates is believed to be central to the understanding of high- $T_c$  superconductivity.<sup>1</sup> Many ideas have emerged to help us understand the origin of the pseudogap. Examples of theories include the idea of preformed Cooper pairs<sup>2</sup> or a competing order parameter, such as *d*-density wave order.<sup>3</sup> An alternative picture has its roots in Anderson's resonating valence bond (RVB) order.<sup>4,5</sup> Within the RVB framework the pseudogap can emerge naturally as one dopes a Mott insulating state with holes.<sup>6</sup> The model of the underdoped cuprates by Yang, Rice, and Zhang (YRZ) is based on these ideas.<sup>7</sup>

Since the YRZ model was put forward, it has proved successful in describing many features of the underdoped cuprates that cannot be understood from conventional BCS theory. The essential new feature is the presence of an additional energy scale, namely, the pseudogap. In the YRZ model the pseudogap is responsible for reconstructing the antinodal portion of the Fermi surface into closed Luttinger pockets. With this modification, the YRZ model has been able to qualitatively capture the physics of Raman spectra,<sup>8,9</sup> angle-resolved photoemission spectroscopy (ARPES),<sup>10,11</sup> specific heat,<sup>12</sup> penetration depth,<sup>13</sup> and tunneling spectroscopy.<sup>14</sup> More recently, we have applied the YRZ model to the *c*-axis transport properties where we showed that the YRZ model is able to explain the insulting-like *c*-axis behavior while remaining metallic in-plane.<sup>15</sup> It has also been shown to account for the *c*-axis violation of the Ferrell-Glover-Tinkham sum rule.<sup>16</sup> It is remarkable that such a simple modification is capable of capturing the physics of such a diverse range of topics. The recent ARPES observation of fully closed pockets in Bi2212 (Ref. 11) adds further support for the YRZ model. In fact, the results of Yang *et al.*<sup>11</sup> show that the size and shape of the Fermi pockets are in excellent agreement with those of the YRZ model.

The optical response of the *c*-axis is known to be dramatically different from the in-plane response, for both infrared<sup>17</sup> and microwave<sup>18</sup> frequencies. In this paper we examine the differences between in-plane and *c*-axis optical responses. We compute the optical conductivity using the YRZ formalism.

We show that the YRZ model is able to capture the qualitative behavior of the ac optical conductivity both in-plane and along the *c* axis. We use the conductivity to extract information about the behavior of the superfluid density, as well as the distribution of optical spectral weight. Last, we use the low-frequency portion of our data to extract the microwave conductivity and find good agreement with experimental findings. In Sec. II we introduce the formalism required to compute the optical conductivity within the YRZ model. We present our numerical results for the infrared optical conductivity in Sec. III and discuss optical sums and the microwave conductivity in Sec. IV. We summarize and conclude in Sec. V.

**II. OPTICAL CONDUCTIVITY IN THE YRZ MODEL OF THE UNDERDOPED CUPRATES**

The real part of the *c*-axis optical conductivity in the bubble approximation can be expressed in terms of the spectral density,  $A(\mathbf{k}, \omega)$ , and the Gorkov anomalous spectral density,  $B(\mathbf{k}, \omega)$ , through the Kubo formula:

$$\begin{aligned} \text{Re}[\sigma_c(\omega, T)] &= -\frac{e^2 d^2}{\omega} \sum_{\mathbf{k}} t_{\perp}^2(\mathbf{k}) \int_{-\infty}^{\infty} \frac{d\omega'}{2\pi} [f(\omega' + \omega) - f(\omega')] \\ &\quad \times [A(\mathbf{k}, \omega')A(\mathbf{k}, \omega' + \omega) + B(\mathbf{k}, \omega')B(\mathbf{k}, \omega' + \omega)]. \end{aligned} \quad (1)$$

Here  $e$  is the electron charge,  $f(\omega)$  is the Fermi distribution function,  $t_{\perp}(\mathbf{k})$  is an interlayer hopping matrix element, and  $d$  is the interlayer distance. We often make comparisons with the in-plane conductivity where  $t_{\perp}^2 d^2$  should be replaced by  $v_{k_x}^2$ , the electron velocity. The YRZ model provides the coherent part of the Green's function from which we can extract the required spectral densities. For a doping,  $x$ , the Green's function is given by

$$G(\mathbf{k}, \omega) = \sum_{\alpha=\pm} \frac{g_r(x) W_{\mathbf{k}}^{\alpha}}{\omega - E_{\mathbf{k}}^{\alpha} - \Delta_{sc}^2 / (\omega + E_{\mathbf{k}}^{\alpha})}. \quad (2)$$

In the above  $g_r(x)$  is a Gutzwiller renormalization factor and is given by  $g_r(x) = 2x/(1+x)$ . The two energy branches and

PHILLIP E. C. ASHBY AND J. P. CARBOTTE

 PHYSICAL REVIEW B **87**, 184514 (2013)

weights are given by

$$E_{\mathbf{k}}^{\pm} = \frac{1}{2} (\tilde{\xi}_{\mathbf{k}} - \xi_{\mathbf{k}}^0) \pm E_{\mathbf{k}} \quad (3)$$

and

$$W_{\mathbf{k}}^{\pm} = \frac{1}{2} \left( 1 \pm \frac{\tilde{\xi}_{\mathbf{k}}}{E_{\mathbf{k}}} \right). \quad (4)$$

Here

$$E_{\mathbf{k}} = \sqrt{\tilde{\xi}_{\mathbf{k}}^2 + \Delta_{pg}^2}, \quad (5)$$

$$\tilde{\xi}_{\mathbf{k}} = \frac{\xi_{\mathbf{k}} + \xi_{\mathbf{k}}^0}{2}, \quad (6)$$

$$\xi_{\mathbf{k}}^0 = -2t(x)(\cos k_x + \cos k_y), \quad (7)$$

and

$$\begin{aligned} \xi_{\mathbf{k}} = & \xi_{\mathbf{k}}^0 - 4t'(x) \cos k_x \cos k_y \\ & - 2t''(x)(\cos 2k_x + \cos 2k_y) - \mu_p. \end{aligned} \quad (8)$$

$\mu_p$  is a chemical potential that is determined from the Luttinger sum rule. The hopping parameters are  $t(x) = g_t(x)t_0 + (3/8)g_s(x)J\chi$ ,  $t'(x) = g_t(x)t'_0$ , and  $t''(x) = g_t(x)t''_0$ , where  $g_s(x) = 4/(1+x)^2$  is another Gutzwiller renormalization factor,  $J = t_0/3$ ,  $\chi = 0.338$ ,  $t'_0 = -0.3t_0$ , and  $t''_0 = 0.2t_0$ .

In Eq. (5),  $\Delta_{pg}$  is the pseudogap energy scale which is taken to have  $d$ -wave symmetry, along with the superconducting gap. That is,

$$\Delta_{sc} = \frac{\Delta_{sc}^0(x)}{2} (\cos k_x - \cos k_y), \quad (9)$$

$$\Delta_{pg} = \frac{\Delta_{pg}^0(x)}{2} (\cos k_x - \cos k_y). \quad (10)$$

The doping-dependent magnitudes mimic a simplified version of the cuprate phase diagram (see left panel of Fig. 1):

$$\Delta_{sc}^0(x) = 0.14[1 - 82.6(x - 0.2)^2], \quad (11)$$

$$\Delta_{pg}^0(x) = 0.6(1 - x/0.2). \quad (12)$$

This functional form places both optimal doping (the maximum of the superconducting dome, shown in dashed purple in Fig. 1) and the vanishing of the pseudogap energy scale (shown

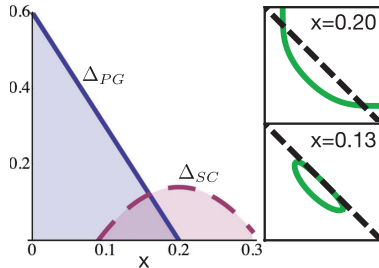


FIG. 1. (Color online) The phase diagram and Fermi surface for the YRZ model. The quantum critical point at which the pseudogap emerges is set to  $x = 0.2$  in this work and corresponds to optimally doped superconductivity. As the pseudogap grows with reduced doping the Fermi surface reconstructs from the large band structure Fermi surface at optimal doping into closed Luttinger pockets.

by the solid blue line in Fig. 1) at  $x = 0.2$ , in accordance with the original YRZ paper.<sup>7</sup> Unless otherwise specified, we use all parameters in the band structure for the YRZ model as they appear in the original publication.<sup>7</sup> In principle, one could alter these parameters to obtain fits to experimental data, but in this work we only wish to show that YRZ captures the essential physics. For the magnitude of the superconducting gap, we use the ratio  $2\Delta_{sc}^0(x, T=0)/(k_B T_c) = 6$ . We work in units where  $\hbar = 1$  and measure all of our energies in terms of  $t_0$ , the nearest-neighbor hopping amplitude.

From the Green's function we obtain the spectral densities

$$\begin{aligned} A(\mathbf{k}, \omega) = & 2\pi g_t(x) \sum_{\alpha=\pm} W_{\mathbf{k}}^{\alpha} [(u^{\alpha})^2 \delta(\omega - E_s^{\alpha}) \\ & + (v^{\alpha})^2 \delta(\omega + E_s^{\alpha})] \end{aligned} \quad (13)$$

and

$$\begin{aligned} B(\mathbf{k}, \omega) = & 2\pi g_t(x) \sum_{\alpha=\pm} W_{\mathbf{k}}^{\alpha} (u^{\alpha} v^{\alpha}) \\ & \times [\delta(\omega - E_s^{\alpha}) - \delta(\omega + E_s^{\alpha})]. \end{aligned} \quad (14)$$

The Bogoliubov quasiparticle energies,  $E_s^{\alpha}$ , and amplitudes,  $u^{\alpha}$  and  $v^{\alpha}$ , are given by

$$E_s^{\alpha} = \sqrt{E_{\mathbf{k}}^{\pm 2} + \Delta_{sc}^2}, \quad (15)$$

$$u^{\alpha} = \sqrt{\frac{1}{2} \left( 1 + \frac{E_{\mathbf{k}}^{\alpha}}{E_s^{\alpha}} \right)}, \quad (16)$$

and

$$v^{\alpha} = \sqrt{\frac{1}{2} \left( 1 - \frac{E_{\mathbf{k}}^{\alpha}}{E_s^{\alpha}} \right)}. \quad (17)$$

The right-hand frame of Fig. 1 shows the normal state [ $\Delta_{sc}^0(x) = 0$ ] Fermi surface reconstruction brought about by the emergence of the pseudogap. Only the upper-right quadrant of the Brillouin Zone (BZ) is shown. The dashed black line indicates the antiferromagnetic BZ (AFBZ) boundary. The solid green curve in the upper frame is the large Fermi surface of Fermi liquid theory for a doping of  $x = 0.2$ . The Fermi liquid contour crosses the AFBZ but is unaffected by it and is characteristic of a good metal. As the doping is reduced towards half filling the Mott insulating state is approached and the Fermi surface contours change radically. The lower frame is for a doping of  $x = 0.13$  where the Fermi surface has reconstructed into a Luttinger hole pocket. The backside of the Luttinger pocket at  $x = 0.13$  closely follows the AFBZ boundary and has very small weight [ $W_{\mathbf{k}}$  in Eq. (4)]. On the other hand, the front side is heavily weighted and is very close to the underlying Fermi liquid surface ( $\Delta_{pg} = 0$ ) in the nodal direction. As  $x$  is reduced further the Luttinger pocket continues to shrink and only a small number of well-defined quasiparticles remain in the nodal direction. This fact is very important for much of the physics that we describe in this paper.

These small holelike pockets are a prediction of the YRZ model and are in excellent agreement with recent photoemission data.<sup>11</sup> However, it is believed that some of the

transport properties in the pseudogap phase are electronlike. Experimentally, it is found that both the Hall and Seebeck coefficients are negative in the pseudogap phase. This apparent contradiction is nicely overcome in a recent proposal by Harrison and Sebastian.<sup>19</sup> They show how a nodal holelike Fermi arc can be reconstructed into electronlike pockets. Their reconstruction mechanism is due to bilayer charge ordering. The wave vectors associated with the charge modulation are responsible for the reconstruction from the holelike Fermi surface into the electronlike one. Importantly, the reconstruction happens with the nodal piece of Fermi surface in their model. The YRZ model naturally makes hole pockets with long-lived quasiparticles along the nodal direction. Additionally, YRZ predicts that these hole pockets are heavily weighted along the front side of the pocket, and so this reconstruction mechanism should apply in exactly the same way as they describe. This extra reconstruction offers a nice explanation for why these

transport coefficients are observed as negative in this part of the phase diagram.

Using the above spectral functions, the conductivity can be written as the sum of two terms,  $\text{Re}[\sigma] = \text{Re}[\sigma_D] + \text{Re}[\sigma_{IB}]$ . The first term,  $\text{Re}[\sigma_D]$ , is peaked around  $\omega = 0$  and is a Drude-like response, while the second term,  $\text{Re}[\sigma_{IB}]$ , arises from interband transitions between the different energy branches. In our calculations we take into account the effect of impurities by replacing the Dirac  $\delta$  functions by Lorentzians of half-width  $\Gamma$ . In the clean limit we find

$$\text{Re}[\sigma_D] = -2\pi e^2 d^2 g_t^2 \sum_{\mathbf{k}} t_{\perp}^2(\mathbf{k}) \delta(\omega) \times \left[ W_{\mathbf{k}}^{+2} \frac{\partial f(E_s^+)}{\partial E_s^+} + W_{\mathbf{k}}^{-2} \frac{\partial f(E_s^-)}{\partial E_s^-} \right] \quad (18)$$

and

$$\text{Re}[\sigma_{IB}] = 2\pi e^2 d^2 g_t^2 \sum_{\mathbf{k}} t_{\perp}^2(\mathbf{k}) W_{\mathbf{k}}^+ W_{\mathbf{k}}^- \left\{ (u^- v^+ - u^+ v^-)^2 \frac{1 - f(E_s^+) - f(E_s^-)}{E_s^+ + E_s^-} [\delta(\omega - E_s^+ - E_s^-) + \delta(\omega + E_s^+ + E_s^-)] - (u^+ u^- + v^+ v^-)^2 \frac{f(E_s^+) - f(E_s^-)}{E_s^+ - E_s^-} [\delta(\omega - E_s^+ + E_s^-) + \delta(\omega + E_s^+ - E_s^-)] \right\}. \quad (19)$$

When using the clean limit formulas, one must instead replace the Dirac  $\delta$  functions by Lorentzians of half-width  $2\Gamma$ .

For the interlayer tunneling matrix element we follow Chakravarty *et al.*<sup>20</sup> and choose  $t_{\perp}(\mathbf{k}) = t_{\perp}[\cos(k_x) - \cos(k_y)]^2$ . This choice reflects the geometric arrangement of the atoms between adjacent  $\text{CuO}_2$  planes. For the  $ab$  plane the velocity is simply  $v_{k_x} = d\xi/dk_x$ . The last free parameter we have is the scattering rate which broadens the Dirac  $\delta$  functions. We used

$$\Gamma = \begin{cases} 0.001 + 0.1(\frac{T}{T_c})^3, & T \leq T_c, \\ 0.051 + 0.05\frac{T}{T_c}, & T > T_c. \end{cases} \quad (20)$$

A linear in  $T$  quasiparticle scattering rate has been associated with the inelastic scattering in the high- $T_c$  oxides. It is taken to be a characteristic of their normal state. The marginal Fermi liquid phenomenology<sup>21</sup> is based on this observation as well as the idea that the dominant scattering processes involve spin and charge excitations of the electronic system itself. On entering the superconducting state, the emergence of the superconducting gap reduces both the charge and spin susceptibility and leads to a reduction in scattering. This reduction in scattering is a hallmark of an electronic mechanism for the inelastic scattering and is often referred to as the collapse of the inelastic scattering rate.<sup>22–26</sup> This collapse of the scattering rate is the accepted explanation of the large peaks observed in the microwave<sup>27</sup> and thermal conductivity<sup>28</sup> of the cuprates well below  $T_c$ . While the normal fluid density (which is resistive) is reduced with temperature, the inelastic scattering lifetime increases. The increase ceases when the residual scattering becomes dominant and it is the further

reduction in normal fluid density that drives the conductivity to zero as observed in the experiment.<sup>27</sup>

### III. NUMERICAL RESULTS

After all of these choices we can evaluate the conductivity. In all of our plots  $\text{Re}[\sigma_{ab}]$  is in units of  $e^2/d$  while  $\text{Re}[\sigma_c]$  is measured in units of  $e^2 d t_{\perp}^2$ . This choice of units does not limit us to a particular material. Once one chooses values for  $t_{\perp}$ ,  $d$ , and the band structure parameters (which determine the Fermi velocity), then our calculations can be compared to any cuprate superconductor. Note that in these units, the in-plane conductivity need not be greater than its  $c$ -axis counterpart, which it is for any realistic value of Fermi velocity and tunneling matrix element. Figure 2 shows the result of a calculation at  $T = 0.25T_c$  for optimal doping ( $x = 0.20$ ) as well as underdoped ( $x = 0.13$ ). We chose  $x = 0.2$  to highlight the physics in the absence of a pseudogap. By contrast, the  $x = 0.13$  case has sizable pseudogap and superconducting energy scales. This choice allows us to see the effect of both energy scales in our data most easily. In the  $x = 0.20$  case (bottom two frames of Fig. 2), there is only a coherent Drude-like response from the large Fermi surface in both the  $ab$  plane and the  $c$  axis. The  $c$ -axis response is reduced as compared with the  $ab$  response by the out-of-plane matrix element  $t_{\perp}(\mathbf{k})$  which gives less weight to the part of the Fermi surface in the nodal direction. In the underdoped case (top two frames of Fig. 2), there is still a Drude response from the remaining Fermi surface. It is suppressed in both the  $ab$  plane and the  $c$  axis due to both the shrinking size of the Fermi

PHILLIP E. C. ASHBY AND J. P. CARBOTTE

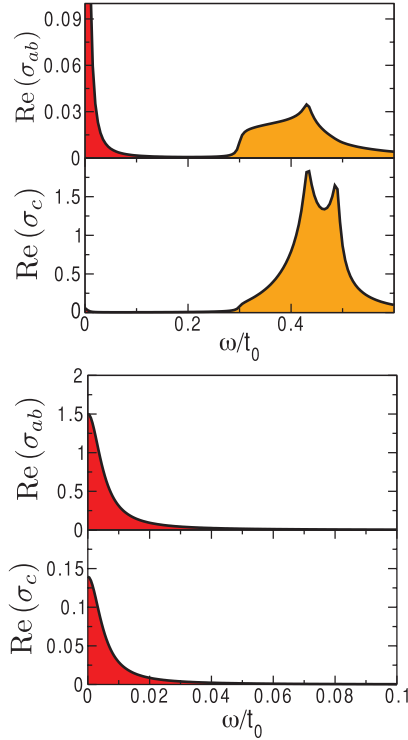
 PHYSICAL REVIEW B **87**, 184514 (2013)


FIG. 2. (Color online) Top panel: The optical conductivity [ $\text{Re}(\sigma_{ab})$  measured in units of  $e^2/d$ , and  $\text{Re}(\sigma_c)$  measured in units of  $e^2 dt_0^2$ ] at doping  $x = 0.13$  and  $T = 0.25T_c$ . Both the  $ab$  plane and the  $c$  axis contain a coherent Drude response (red/shaded area on left) and an interband contribution from the presence of the pseudogap energy (orange/shaded area on right). Bottom panel: The optical conductivity at optimal doping ( $x = 0.20$ ) and  $T = 0.25T_c$ . At optimal doping the pseudogap vanishes and there is only a Drude contribution to the conductivity.

surface and the Gutzwiller renormalization factors. There is also a piece due to interband transitions at higher energies. This piece is the signature of the pseudogap energy scale. It is the dominant feature in the  $c$ -axis data.

With a more realistic treatment of the inelastic scattering we expect this interband feature to broaden beyond what is shown in Fig. 2. In the cuprates the inelastic scattering rate is known to have a strong energy dependence<sup>29</sup> in addition to temperature variation. In Eq. (20) we have included only temperature dependence through an impurity model; i.e., there is no dependence on  $\omega$ . This model for the inelastic scattering rate is perfectly adequate as far as dc properties are concerned. It is oversimplified when the photon energy falls in the infrared. In this energy range,  $\Gamma(T, \omega)$  can be much larger than its  $\omega = 0$  value, modeled in Eq. (20). Consequently, the interband optical transition peak in  $\text{Re}[\sigma(t, \omega)]$  will be broadened.

In Fig. 3 the optical conductivity is shown as a function of frequency for four temperatures: as labeled in the figure,  $T = 4T_c$ , dashed blue line;  $T = 2T_c$ , solid orange line;

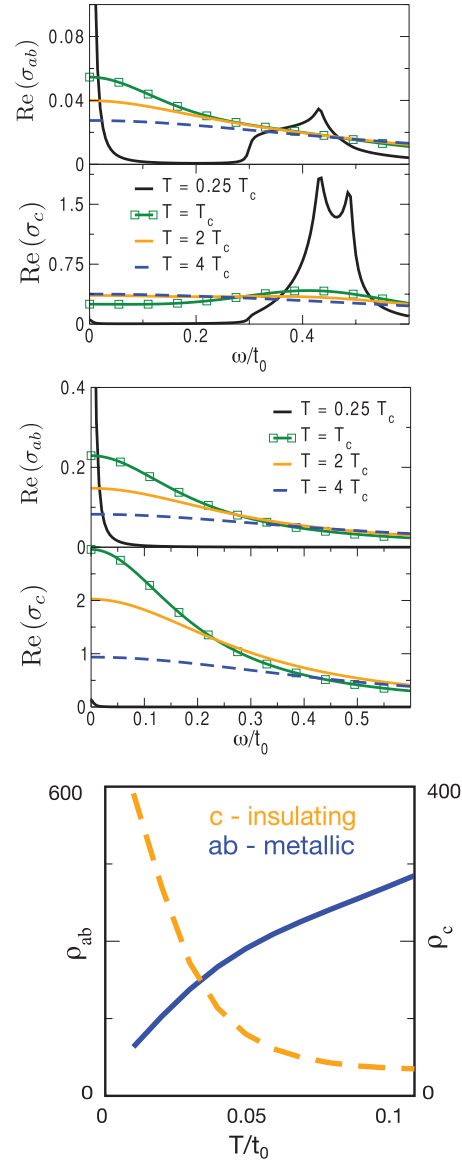


FIG. 3. (Color online) Top panel: The optical conductivity [ $\text{Re}(\sigma_{ab})$  measured in units of  $e^2/d$ , and  $\text{Re}(\sigma_c)$  measured in units of  $e^2 dt_0^2$ ] at doping  $x = 0.13$  for temperatures  $T = 0.25T_c$ ,  $T_c$ ,  $2T_c$ , and  $4T_c$ . The Drude peak becomes increasingly broadened with temperature. At low temperatures a feature of the pseudogap emerges beyond  $\omega = 0.3t_0$ . This feature is a natural explanation for the broad peak observed at  $400 \text{ cm}^{-1}$  in Homes *et al.*<sup>17</sup> Middle panel: The optical conductivity at doping  $x = 0.20$  for temperatures  $T = 0.25T_c$ ,  $T_c$ ,  $2T_c$ , and  $4T_c$ . Both in-plane and  $c$  axis only have Drude contributions which become increasingly broadened with temperature. Bottom panel: The resistivity in the underdoped cuprates from the YRZ model as a function of temperature at  $x = 0.05$ . The underdoped phase is metallic in-plane and resistive along the  $c$  axis. Taken with permission from Ashby and Carbotte.<sup>15</sup>

$T = T_c$ , in solid green with boxes and  $T = 0.25T_c$  in solid black. The top two frames are for doping  $x = 0.13$  and the middle two frames are at optimal doping ( $x = 0.2$ ). For  $\omega \lesssim 0.2t_0$  all curves are Drude like and order in temperature in the usual way, *except* the  $c$ -axis curves in the underdoped case. In this case, we see a different trend, the curves order in the opposite sense as temperature is reduced. This behavior is emphasized in the lowest frame where we show our results (for  $x = 0.05$ ) for the dc resistivity as a function of temperature. We see that the  $c$  axis displays insulating like behavior ( $\rho_c$  increases as  $T$  decreases), while the  $ab$  plane response remains metallic ( $\rho_{ab}$  decreases as  $T$  decreases). We stress that the YRZ model captures this behavior through a coherent tunneling Hamiltonian.<sup>15,30,31</sup>

The top two frames of Fig. 3 are to be compared with the experimental work of Homes *et al.*<sup>17</sup> on the  $c$ -axis conductivity of yttrium barium copper oxide (YBCO). As in the experiments, the signatures of the pseudogap are more pronounced at low energies. This is characterized by a flat region at low frequency which becomes increasingly suppressed at lower temperatures. The reduction we calculate is not as dramatic as that observed in the experimental data. If one wished to obtain better fits to the experimental results this could be achieved by adjusting the scattering rate or the magnitude of the pseudogap energy scale. Note that the low-frequency  $c$ -axis conductivity behaves very differently from the in-plane conductivity as a function of temperature. Perhaps the most striking feature in Fig. 3 is the broad interband feature from  $\omega \sim 0.3t_0$  to  $\omega \sim 0.5t_0$  associated with the pseudogap. This feature is a natural explanation for the broad peak observed in Homes *et al.*<sup>17</sup> at  $400 \text{ cm}^{-1}$ . Taking  $t_0 = 125 \text{ meV}$ , this feature falls in the range of  $300\text{--}500 \text{ cm}^{-1}$ , in agreement with the experiments. Previous explanations of this feature invoke the existence of an interlayer plasmon collective mode.<sup>32</sup> Within the YRZ model this peak is produced only from pseudogap physics with no need for this collective mode.

#### IV. OPTICAL SUM AND MICROWAVE CONDUCTIVITY

##### A. Optical sums

Sum rules and partial optical sums also provide useful information. In a conventional superconductor, the suppression of  $\text{Re}[\sigma]$  for  $T < T_c$  is connected to the appearance of a superconducting condensate. The “missing” optical spectral weight appears in a  $\delta$  function of the appropriate weight at  $\omega = 0$ . This fact is usually presented as the Ferrel-Glover-Tinkham sum rule. In terms of the superfluid stiffness,  $\rho_s$ ,

$$N_N - N_S = \rho_s, \quad (21)$$

where

$$N_N = \int_{0^+}^{\infty} d\omega \text{Re}[\sigma_n(\omega, T)] \quad (22)$$

is the normal state optical sum and

$$N_S = \int_{0^+}^{\infty} d\omega \text{Re}[\sigma_s(\omega, T)] \quad (23)$$

is the superconducting optical sum. While this sum rule holds in-plane, it is known to be violated in the  $c$  axis.<sup>33</sup> The

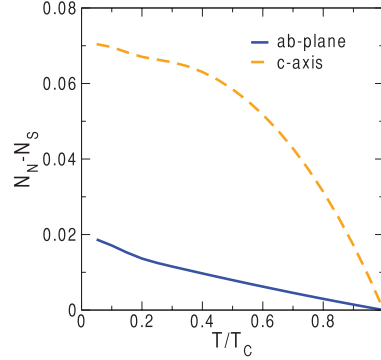


FIG. 4. (Color online) Normal state optical sum minus superconducting state optical sum as a function of temperature for doping  $x = 0.13$ . The behavior of the superfluid density in the  $c$  direction is qualitatively different from that in the  $ab$  plane.

YRZ model with the same interlayer tunneling matrix element that we use displays a violation of this sum rule.<sup>16</sup> This is understood most simply in a limit of the YRZ model that reduces to a Fermi arc model. In this model the Fermi surface is confined about the nodal direction; the remainder of the large Fermi surface from Fermi liquid theory is gapped out by the pseudogap. Only the electrons on the arc contribute the usual amount to the optical sum rule, while those on the gapped out portion contribute less. In any case,  $N_N - N_S$  is well defined and is shown in Fig. 4. The solid blue line is the  $ab$ -plane result, while the orange dashed line applies to the  $c$  direction. As a function of the reduced temperature,  $t = T/T_c$ , those curves behave in much the same way as is found for the superfluid density itself.<sup>13,34</sup> The superfluid density follows from the imaginary part of the conductivity as

$$\frac{1}{\lambda^2(T)} = \lim_{\omega \rightarrow 0} \frac{4\pi}{c^2} \omega \text{Im}[\sigma(T, \omega)], \quad (24)$$

with  $c$  being the velocity of light. The temperature behaviors are in agreement with the superfluid density inferred from microwave experiments.<sup>18</sup> The  $ab$ -plane superfluid density decreases linearly with temperature while the  $c$ -axis is flat at low temperatures.

A related quantity, the partial optical sum,

$$I(\omega) = \int_{0^+}^{\omega} d\omega' \{ \text{Re}[\sigma_n(\omega', T)] - \text{Re}[\sigma_s(\omega', T)] \}, \quad (25)$$

provides information about the distribution of spectral weight that goes into the superconducting condensate. The partial optical sums for the YRZ model, normalized to their value at  $\omega = 1$ , are shown in the top panel of Fig. 5. The solid blue curve is for the  $ab$  plane and the dashed orange curve is for the  $c$  axis. For a regular superconductor this curve would sharply rise towards 1, with the scattering rate,  $\Gamma$ , setting the energy scale of the rise. In the YRZ model the presence of the pseudogap causes a redistribution of spectral weight from the Drude to the high-frequency region. This redistribution shows itself in the suppressed flat region at low frequencies accompanied by a pileup of spectral weight above the pseudogap energy scale. This redistribution is much more pronounced for the  $c$  axis.

PHILLIP E. C. ASHBY AND J. P. CARBOTTE

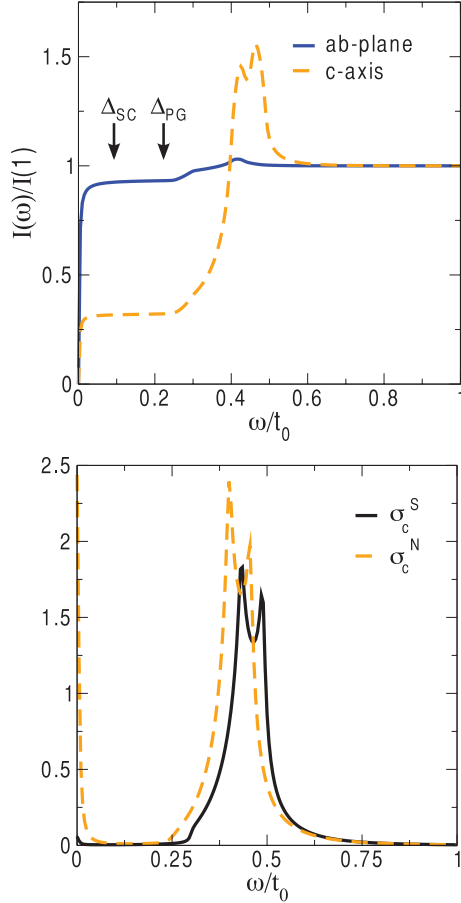
 PHYSICAL REVIEW B **87**, 184514 (2013)


FIG. 5. (Color online) Top panel: Partial optical sum at  $T = 0.25T_c$  for doping  $x = 0.13$  for the *ab* plane and the *c* axis. The gap scales are indicated in the figure. The pseudogap causes an extra suppression and redistributes the charge carriers available for condensation to high frequencies. Bottom panel: *c*-axis conductivities in the superconducting and normal states for  $x = 0.13$  at  $T = 0.25T_c$ . The redistribution of spectral weight due to having superconductivity leads to a shift in the interband peak.

Insight into these shifts in spectral weight can be gleaned from the lower frame where we show the real part of the conductivity as a function of frequency for  $x = 0.13$  at  $T = 0.25T_c$ . The dashed orange curve is the normal state ( $\Delta_{pg} = 0$ ) and the black curve is the corresponding superconducting case. We see that the opening of the superconducting gap shifts the interband transitions to higher energies. This shift accounts for the large peak seen in the orange curve in the top frame of Fig. 5 for  $\omega \gtrsim 0.4t_0$ .

### B. Microwave conductivity

The microwave data are qualitatively different for the in-plane conductivity and the *c* axis conductivity.<sup>18</sup> The in-plane

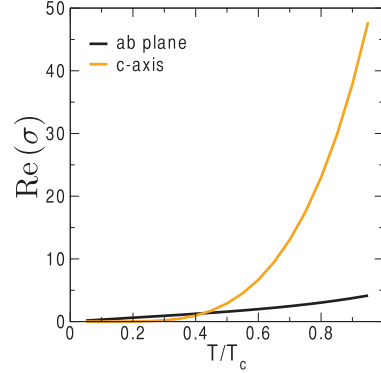


FIG. 6. (Color online) Microwave conductivity [ $\text{Re}(\sigma_{ab})$ ] measured in units of  $e^2/d$ , and  $\text{Re}(\sigma_c)$  measured in units of  $e^2 dt_0^2$  for a constant  $\Gamma = 0.005$  as a function of temperature. This is proportional to the number of particles able to absorb low-frequency radiation. The behavior in-plane is linear in  $T$ , while the *c* axis behaves roughly like  $T^5$ .

data contain a peak, while the *c*-axis data do not. The peak is attributed to the interplay between the quasiparticle lifetime and the amount of fluid which can absorb radiation. As the system is cooled below  $T_c$  the quasiparticle scattering lifetime changes. As the temperature decreases the normal component of the fluid vanishes linearly (Fig. 6). If the lifetime increases faster than the normal part of the fluid, this will lead to an increasing conductivity. At low enough temperature, the lifetime will saturate to the value set by the residual scattering rate, and the conductivity will decrease as the remaining normal fluid condenses. This behavior generally produces a peak in the microwave data. It is thus, very surprising that the *c* axis lacks a peak. This was originally interpreted as evidence for incoherent *c*-axis transport.<sup>18</sup> In this work we take a coherent model for *c*-axis transport and interpret the difference as a signature of how the superfluid density is changing. This view is similar to the work of T. Xiang and collaborators<sup>31,35</sup> where they obtained good agreement with the resistivity and microwave conductivity using a different phenomenological model.

The microwave conductivity is obtained from the low-frequency part of  $\text{Re}[\sigma(\omega)]$ . We obtain the microwave conductivity by taking  $\lim_{\omega \rightarrow 0} \text{Re}[\sigma(\omega)]$ . In Fig. 6 we show the microwave conductivity for a constant scattering rate,  $\Gamma = 0.005$ . The solid black curve is  $\text{Re}[\sigma(T, \omega = 0)]$  for the *ab* plane while the orange curve is for the *c* axis, both as a function of reduced temperature,  $T/T_c$ . Their temperature dependence is strikingly different as we would have expected based on the results presented in Fig. 4 for  $N_N - N_S$  vs  $T/T_c$ . For a first understanding of the experimental results for  $\text{Re}[\sigma(T, \omega = 0)]$ , it is helpful to take guidance from the two-fluid model. Under the assumption that only the normal fluid component,  $n$ , is involved in the absorption, the expression for the Drude conductivity is

$$\text{Re}[\sigma] = \frac{ne^2}{m\Gamma}. \quad (26)$$

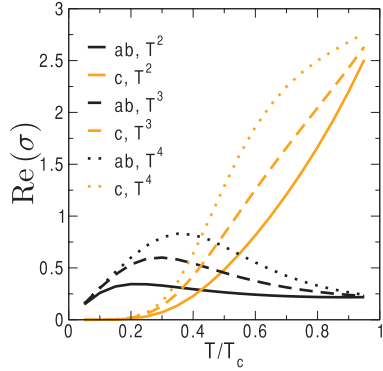


FIG. 7. (Color online) The in-plane and *c*-axis microwave conductivity [ $\text{Re}(\sigma_{ab})$ ] measured in units of  $e^2/d$ , and  $\text{Re}(\sigma_c)$  measured in units of  $e^2 d t_{\perp}^2$  for  $x = 0.20$  as a function of temperature for various different forms of scattering rate.

Here  $e$  is the electron charge and  $m$  is the mass. We see in Fig. 6 that  $n$  is nearly linear in plane and  $\propto T^5$  out of plane.

In Fig. 7 we show the microwave conductivity at optimal doping for different scattering rates. We used  $\Gamma = 0.001 + 0.1(T/T_c)^\alpha$  for  $\alpha = 2, 3, 4$ . Dotted lines correspond to  $T^4$  law, dashed lines to  $T^3$ , and solid lines to  $T^2$ , with black for the *ab* plane and orange for the *c* axis. The in-plane data always contains a peak, as we expect. If the scattering rate becomes too strongly temperature dependent, the *c*-axis conductivity is no longer convex like in the experiments. Using the Drude form for the conductivity with  $\Gamma = A + BT^\alpha$  and  $n \propto T^\beta$  we can show that for the conductivity to be convex that  $\alpha < 1 - 2\beta + 2\sqrt{2\beta(\beta - 1)}$ . Using  $\beta \approx 5$  from our constant scattering rate calculation, we see this sets an upper bound of  $\alpha = 3.65$ .

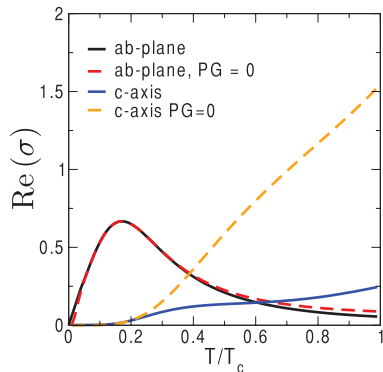


FIG. 8. (Color online) The microwave conductivity [ $\text{Re}(\sigma_{ab})$ ] measured in units of  $e^2/d$ , and  $\text{Re}(\sigma_c)$  measured in units of  $e^2 d t_{\perp}^2$  in the underdoped phase ( $x = 0.13$ ) as a function of temperature. We also show the calculation with  $\Delta_{pg} = 0$ . The pseudogap has almost no effect on the in-plane conductivity, but leads to a dramatic suppression for the *c* axis.

In Fig. 8 we show the microwave conductivity for  $x = 0.13$ . To isolate the effect of the pseudogap, we redid the calculation with  $\Delta_{pg} = 0$ . The solid curves are with the pseudogap and the dashed curves are without. The low-temperature behavior is unaffected by pseudogap formation. It does cause a dramatic suppression of the *c*-axis conductivity at high temperatures, but this effect is much more modest in-plane (Fig. 8). There is a great similarity between the change in temperature behavior of the *c*-axis microwave conductivity and the specific heat.<sup>36</sup> In both cases the low-temperature part of the curve is unaffected since this region depends only on the thermal excitations in the nodal direction. This part of the electronic structure is not appreciably changed by the pseudogap. As the temperature is increased towards  $T_c$  the specific heat is strongly suppressed below its  $\Delta_{pg} = 0$  value, much like the *c*-axis conductivity. This is not surprising as both quantities are closely tied to the electronic density of states. The in-plane microwave conductivity is not and is seen to behave much differently than its *c*-axis counterpart. Unfortunately *c*-axis measurements are technically challenging and experimental data only exist for optimal doping. It would be very interesting to look for the effect of the pseudogap in an underdoped sample.

## V. DISCUSSION AND CONCLUSIONS

We have investigated the *c*-axis optical conductivity in the underdoped cuprates using the YRZ model. We focused on properties in the superconducting phase of the underdoped cuprates at  $x = 0.2$  (optimal doping) and  $x = 0.13$  (underdoped) to highlight the essential features of the model. For the *c*-axis calculations we used a coherent tunneling matrix element to describe interlayer hopping. Our choice of matrix element is one related to the geometric alignment of atoms between adjacent layers, but any matrix element which gives little weight to states along the nodal direction should give qualitatively similar results. We saw that the reduction in the density of states caused by the pseudogap resulted in the low-frequency region of the normal state optical conductivity decreasing as temperature decreased instead of increasing as observed in-plane. This is in agreement with the experimental findings. This decrease continued in the superconducting state with the spectral weight redistributed to higher energies set by the pseudogap energy scale. This redistribution could serve as an explanation for the observation of the broad peak at  $400 \text{ cm}^{-1}$  in underdoped YBCO ( $\text{YBa}_2\text{Cu}_3\text{O}_{6.7}$ ) which is not present in the optimally doped sample ( $\text{YBa}_2\text{Cu}_3\text{O}_{6.95}$ ).<sup>17</sup>

We were also able to extract the behavior of the superfluid density from both a sum rule and from the microwave conductivity. The superfluid density behaves very differently for in-plane and out-of-plane, which manifested itself in the different shapes of the microwave conductivity as a function of temperature. The in-plane microwave conductivity exhibits a peak, while the *c* axis conductivity does not. A previous interpretation<sup>18</sup> took this observation to mean that the *c*-axis interplane transport was incoherent. Here we attribute this to the very different temperature law associated with the *c*-axis superfluid density as compared to that of the *ab* plane. The shape of the *c*-axis conductivity constrains the temperature

PHILLIP E. C. ASHBY AND J. P. CARBOTTE

PHYSICAL REVIEW B **87**, 184514 (2013)

dependence of the scattering in the superconducting state. We also showed that the pseudogap suppresses the microwave conductivity at high temperatures. It would be interesting to see more  $c$ -axis measurements, as they display pseudogap physics more strongly than the in-plane counterparts.

## ACKNOWLEDGMENTS

This work was supported by the Natural Sciences and Engineering Research Council of Canada and the Canadian Institute for Advanced Research.

<sup>\*</sup>ashbype@mcmaster.ca

<sup>†</sup>carbotte@mcmaster.ca

<sup>1</sup>T. Timusk and B. Statt, *Rep. Prog. Phys.* **62**, 61 (1999).

<sup>2</sup>M. R. Norman, A. Kanigel, M. Randeria, U. Chatterjee, and J. C. Campuzano, *Phys. Rev. B* **76**, 174501 (2007).

<sup>3</sup>S. Chakravarty, R. B. Laughlin, D. K. Morr, and C. Nayak, *Phys. Rev. B* **63**, 094503 (2001).

<sup>4</sup>P. W. Anderson, *Science* **235**, 1196 (1987).

<sup>5</sup>F. C. Zhang, C. Gros, T. M. Rice, and H. Shiba, *Supercond. Sci. Technol.* **1**, 36 (1988).

<sup>6</sup>P. A. Lee, N. Nagaosa, and X.-G. Wen, *Rev. Mod. Phys.* **78**, 17 (2006).

<sup>7</sup>K.-Y. Yang, T. M. Rice, and F.-C. Zhang, *Phys. Rev. B* **73**, 174501 (2006).

<sup>8</sup>B. Valenzuela and E. Bascones, *Phys. Rev. Lett.* **98**, 227002 (2007).

<sup>9</sup>J. P. F. LeBlanc, J. P. Carbotte, and E. J. Nicol, *Phys. Rev. B* **81**, 064504 (2010).

<sup>10</sup>K.-Y. Yang, H. B. Yang, P. D. Johnson, T. M. Rice, and F.-C. Zhang, *Europhys. Lett.* **86**, 37002 (2009).

<sup>11</sup>H. B. Yang, J. D. Rameau, Z. H. Pan, G. D. Gu, P. D. Johnson, H. Claus, D. G. Hinks, and T. E. Kidd, *Phys. Rev. Lett.* **107**, 047003 (2011).

<sup>12</sup>J. P. F. LeBlanc, E. J. Nicol, and J. P. Carbotte, *Phys. Rev. B* **80**, 060505 (2009).

<sup>13</sup>J. P. Carbotte, K. A. G. Fisher, J. P. F. LeBlanc, and E. J. Nicol, *Phys. Rev. B* **81**, 014522 (2010).

<sup>14</sup>K.-Y. Yang, K. Huang, W.-Q. Chen, T. M. Rice, and F.-C. Zhang, *Phys. Rev. Lett.* **105**, 167004 (2010).

<sup>15</sup>P. E. C. Ashby and J. P. Carbotte, *Phys. Rev. B* **87**, 014514 (2013).

<sup>16</sup>J. P. Carbotte and E. Schachinger, *Phys. Rev. B* **86**, 224512 (2012).

<sup>17</sup>C. C. Homes, T. Timusk, R. Liang, D. A. Bonn, and W. N. Hardy, *Phys. Rev. Lett.* **71**, 1645 (1993).

<sup>18</sup>A. Hosseini, S. Kamal, D. A. Bonn, R. Liang, and W. N. Hardy, *Phys. Rev. Lett.* **81**, 1298 (1998).

<sup>19</sup>N. Harrison and S. E. Sebastian, *New J. Phys.* **14**, 095023 (2012).

<sup>20</sup>S. Chakravarty, A. Sudbø, P. W. Anderson, and S. Strong, *Science* **261**, 337 (1993).

<sup>21</sup>C. M. Varma, P. B. Littlewood, S. Schmitt-Rink, E. Abrahams, and A. E. Ruckenstein, *Phys. Rev. Lett.* **63**, 1996 (1989).

<sup>22</sup>M. C. Nuss, P. M. Mankiewich, M. L. O'Malley, E. H. Westerwick, and P. B. Littlewood, *Phys. Rev. Lett.* **66**, 3305 (1991).

<sup>23</sup>E. Schachinger, J. P. Carbotte, and F. Marsiglio, *Phys. Rev. B* **56**, 2738 (1997).

<sup>24</sup>E. J. Nicol and J. P. Carbotte, *Phys. Rev. B* **44**, 7741 (1991).

<sup>25</sup>A. Hosseini, R. Harris, S. Kamal, P. Dosanjh, J. Preston, R. Liang, W. N. Hardy, and D. A. Bonn, *Phys. Rev. B* **60**, 1349 (1999).

<sup>26</sup>F. Marsiglio, *Phys. Rev. B* **73**, 064507 (2006).

<sup>27</sup>D. A. Bonn, S. Kamal, K. Zhang, R. Liang, D. J. Baar, E. Klein, and W. N. Hardy, *Phys. Rev. B* **50**, 4051 (1994).

<sup>28</sup>M. Matsukawa, T. Mizukoshi, K. Noto, and Y. Shiohara, *Phys. Rev. B* **53**, R6034 (1996).

<sup>29</sup>E. Schachinger, J. J. Tu, and J. P. Carbotte, *Phys. Rev. B* **67**, 214508 (2003).

<sup>30</sup>A. Levchenko, T. Micklitz, M. R. Norman, and I. Paul, *Phys. Rev. B* **82**, 060502 (2010).

<sup>31</sup>Y. H. Su, H. G. Luo, and T. Xiang, *Phys. Rev. B* **73**, 134510 (2006).

<sup>32</sup>M. Grüninger, D. van der Marel, A. A. Tsvetkov, and A. Erb, *Phys. Rev. Lett.* **84**, 1575 (2000).

<sup>33</sup>D. N. Basov, S. I. Woods, A. S. Katz, E. J. Singley, R. C. Dynes, M. Xu, D. G. Hinks, C. C. Homes, and M. Strongin, *Science* **283**, 49 (1999).

<sup>34</sup>J. P. Carbotte and E. Schachinger, *J. Phys.: Condens. Matter* **25**, 165702 (2013).

<sup>35</sup>T. Xiang and W. N. Hardy, *Phys. Rev. B* **63**, 024506 (2000).

<sup>36</sup>A. J. H. Borne, J. P. Carbotte, and E. J. Nicol, *Phys. Rev. B* **82**, 094523 (2010).



## Weyl Semimetals

In a non-interacting picture, we understand that materials with partially filled bands are metals. Likewise, materials without partially filled bands and an energy gap between the valence and conduction bands are insulators. When there are no partially filled bands, and the bands just touch, the material is a semimetal. This classification was one of the great triumphs of the band theory of solids.

Recently it was realized that even within materials of a single category, say insulators, that there could be qualitative difference in their properties [34]. We now realize that there are a class of insulators that are insulating in the bulk, but have conductive surfaces. Interestingly, these conductive surfaces are also incredibly robust against perturbations, as long as the perturbation leaves the system an insulator. Materials of the second type are the so called topological insulators. These ideas have called for a refinement in the classification of solids. The new concept that has proved useful in this refinement is the study of the topology of the band structure.

In a gapped system, like an insulator or a superconductor, the wavefunctions may have non-trivial winding around the Brillouin zone. This non-trivial winding is what separates a topological phase from a normal trivial phase. Perhaps the most famous example of a topological insulator is the quantum Hall effect. The quantum Hall effect was first observed in the 1980's [35] in two dimensional electronic systems subjected to high magnetic fields. The Hall conductivity was observed to have plateaus as a function of magnetic field (see Figure 5.1). These plateaus took on very precise values,

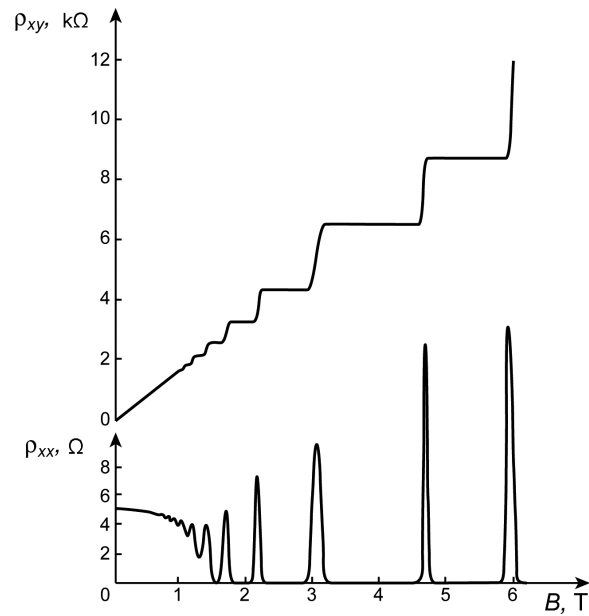


Figure 5.1: The Hall resistivity (top) and diagonal resistivity (bottom) as a function of applied field. Notice the plateaus in the Hall resistivity. These plateaus are quantized and robust against disorder. They are a sign of the momentum space topology of the quantum Hall wavefunctions. Taken from wikimedia. Released under the GNU Free Documentation License.

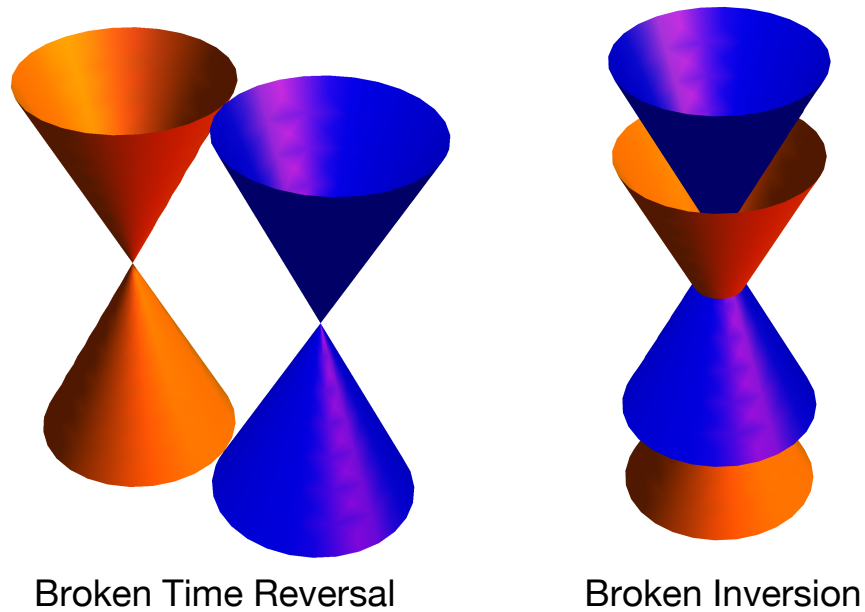


Figure 5.2: The low energy spectra for different broken symmetries is shown. The case of broken time reversal symmetry is pictured on the left, while broken inversion symmetry is shown on the right. This separation leads to interesting physical effects, such as an anomalous Hall effect.

and seemed insensitive to the amount of disorder in the system. These values were quantized at  $ne^2/(2\pi)$  for integer  $n$ . This robustness to disorder is now understood from the underlying topological nature of this phase. The quantum Hall systems are bulk insulators whose edges are conducting wires. These systems were the first examples of topological insulators.

For a gapless phase, like a semimetal or a metal, if the band structure contains topological defects in momentum space then it can be classified according to winding of the Green's function around these defects [36]. The Weyl semimetal is an example of such a topologically non-trivial band structure. It is for this reason that Weyl semimetals have become quite popular in recent years.

The Hamiltonian for an isolated Weyl point with chirality  $\nu = \pm 1$  takes the form

$$\mathcal{H} = \pm v_F \boldsymbol{\sigma} \cdot \mathbf{k}, \quad (5.1)$$

here  $\mathbf{k}$  is the distance from the Weyl point in momentum space.

The Nielsen-Nyomiya theorem [37] states that such points must always come in pairs of opposite chirality. Furthermore, in any system with both time-reversal symmetry and inversion symmetry, these two points must lie on top of each other. The proof of this is as follows. Suppose there is a Weyl node of chirality +1 at some point  $\mathbf{k}_1$  in the Brillouin zone. Action under time reversal tells us there must be a state with chirality +1 at  $-\mathbf{k}_1$ . But the Nielsen-Nyomiya theorem tells us that the total chirality in the Brillouin zone must be zero. So by the preceding logic there must be two Weyl points of chirality  $-1$  at  $\mathbf{k}_2$  and  $-\mathbf{k}_2$ . Now we consider action under inversion symmetry. Inversion symmetry requires that points  $\mathbf{k}$  and  $-\mathbf{k}$  have opposite chirality. So we must have  $\mathbf{k}_1 = \mathbf{k}_2$ . Thus to have isolated Weyl nodes, one of the time reversal or inversion symmetries must be broken. Breaking each of these symmetries separates the Weyl points in different ways. This is pictured in Figure 5.2. When time reversal symmetry is broken the Weyl points are separated in momentum. On the other hand, when inversion symmetry is broken they are separated in energy.

One can see from the form of the Hamiltonian that it is very robust against perturbations. Since all three Pauli matrices are used up, one cannot add a perturbation that will easily destroy the Weyl point. There is no extra Pauli matrix to gap out the Weyl node. The only way that one can be destroyed is by adding a perturbation large enough to push two Weyl point into each other, or by allowing for scattering between the Weyl points.

A number of very interesting effects have been predicted based on the topological nature of these Weyl points. Theoretical work [38, 39] shows that their low energy electrodynamic response is governed by a topological term

$$\frac{e^2}{8\pi^2} \int d^4x \theta(x) \mathbf{E} \cdot \mathbf{B}, \quad (5.2)$$

where  $\theta$  is ‘axion’ angle and is proportional to the separation of the Weyl points in momentum space. This term leads to the result that the hall conductivity is proportional to the separation of the Weyl points [40]. It is given by  $\sigma_{xy} = e^2/(4\pi^2)\Delta k$ , where  $\Delta k$  is the separation of the Weyl points. This peculiar response to applied magnetic and electric fields of the form  $\mathbf{E} \cdot \mathbf{B}$  could potentially be used to drive

a current between two Weyl nodes [41]. This would open the door to the field of valleytronics in these materials.

Weyl semimetals are also expected to have interesting conductive surface states. These surface states are open segments of Fermi surface that terminate at Weyl nodes [42]. Both the top and bottom surfaces are predicted to have open segments of Fermi surface on them. These two segments taken together would constitute a closed Fermi surface. Observation of these unique surface states by a technique like Angle resolved photoemission spectroscopy (ARPES) would be good evidence for the existence of a Weyl semimetal.

A potential candidate for the existence of the Weyl semimetallic state is in certain quasicrystalline samples [43]. These samples show linear conductivity over a large range of frequency. For a Hamiltonian linear in momentum in 3-dimensions a linear conductivity is expected[44]. Furthermore, the optical evidence shows no sign of a Drude peak. This is a sign that there are very few free charge carriers in the system, and thus the chemical potential may lie at the Weyl node.

## 5.1 Paper V – Magneto-optical conductivity of Weyl semimetals

Reprinted with permission as follows: Phillip E.C. Ashby and J.P. Carbotte “*Magneto-optical conductivity of Weyl semimetals*” Phys. Rev. B **87** 245131 (2013). Copyright (2013) by the American Physical Society.

Motivated by the possibility that quasicrystals might be Weyl semimetals we were encouraged by Tom Timusk to pursue this project. Fermi-arcs and anomalous Hall conductivity would be good evidence for a Weyl semimetal, but many physical observables have not yet been calculated for this state. A previous paper had studied the finite frequency conductivity in the presence of disorder and found two regimes of transport. In this paper we studied the finite frequency conductivity in an applied magnetic field. We were motivated to do this since Weyl semimetals have an interesting response to electromagnetic fields. We found that the conductivity was given by a set of asymmetric series of peaks lying on top of the zero-field limit. These peaks appear at frequencies that are clear signature of the relativistic Hamiltonian, and are robust against modest disorder.

PHYSICAL REVIEW B 87, 245131 (2013)

**Magneto-optical conductivity of Weyl semimetals**

Phillip E. C. Ashby\*

*Department of Physics and Astronomy, McMaster University, Hamilton, Ontario, Canada L8S 4M1*

J. P. Carbotte†

*Department of Physics and Astronomy, McMaster University, Hamilton, Ontario, Canada L8S 4M1 and  
The Canadian Institute for Advanced Research, Toronto, Ontario, Canada M5G 1Z8*

(Received 1 May 2013; revised manuscript received 10 June 2013; published 27 June 2013)

Weyl semimetals are a topological phase of matter that have drawn recent interest and have been suggested as a possible phase of the pyrochlore iridates, among other materials. Here we compute the magneto-optical response of an isolated Weyl point. We find that the conductivity is a series of asymmetric peaks lying on top of a linear background. We find additional features in the conductivity that are explained by the underlying Landau level structure. We show that weak disorder tends to blur out the peaks, but they still show up as measurable oscillations on a linear background.

DOI: [10.1103/PhysRevB.87.245131](https://doi.org/10.1103/PhysRevB.87.245131)

PACS number(s): 78.20.Ls, 71.70.Di, 71.90.+g

**I. INTRODUCTION**

A Dirac semimetal is a material in which the conduction and valence bands only touch at isolated points within the Brillouin zone (BZ). Around these points the dispersion is linear and the low energy theory is described by a Dirac Hamiltonian. Perhaps the most famous Dirac material is graphene, which contains two inequivalent Dirac points in its BZ. These two-dimensional (2D) Dirac points are not robust against perturbations. Any perturbation proportional to  $\sigma_z$  will gap out the band touching. For example, in graphene spin-orbit coupling should induce a mass gap. However, since carbon has such a small atomic number, spin-orbit coupling is very weak and this splitting has never been measured in graphene. Furthermore, only intrinsic spin-orbit interactions will induce a mass gap. Extrinsic interactions of the Rashba type do not induce a gap in the Dirac spectrum.<sup>1</sup>

Dirac semimetals can also exist in three dimensions (3D). An isolated band touching is described by the Hamiltonian

$$\mathcal{H} = v_F \boldsymbol{\sigma} \cdot \mathbf{k}, \quad (1)$$

where  $v_F$  is the Fermi velocity,  $\boldsymbol{\sigma}$  is the vector of Pauli matrices, and  $\mathbf{k}$  is the momentum as measured from the band touching. This equation is the electronic analog of the Weyl equation from particle physics. Materials described by such a Hamiltonian have become known as *Weyl semimetals*. The Weyl Hamiltonian is completely robust against any perturbation since it uses all three of the Pauli matrices. In materials with time reversal symmetry ( $\mathcal{T}$ ) and inversion symmetry ( $\mathcal{I}$ ) then there must be four bands linearly dispersing around any band touching point in the BZ. Such a material is called a 3D Dirac semimetal and it is not robust against perturbations since there are additional Dirac matrices in the  $4 \times 4$  representation. In a system with broken  $\mathcal{T}$  or  $\mathcal{I}$  it is possible to have a phase described by the Weyl Hamiltonian.

Weyl points also have interesting topological properties. They are monopoles of Berry flux in the BZ. This peculiar momentum space topology manifests itself in several ways. One way is the peculiar nature of the gapless surface states. The surface states of a Weyl semimetal are known as Fermi arcs.<sup>2</sup> These Fermi arcs are open segments of Fermi surface

connecting the projections of the Weyl points onto the 2D surface BZ. These arcs connect Weyl points of opposite chirality and are a signature of the topological nature of the Weyl points. Another manifestation of the topological nature of Weyl points is in the low energy electromagnetic response. The low energy effective action contains a topological  $\theta$  term and is described by axion electrodynamics.<sup>3</sup> The physical effect of this exotic  $\theta$  term is an anomalous Hall conductivity.<sup>4</sup> The equations of motion also show that these materials could exhibit a chiral magnetic effect—dissipationless currents in response to an applied magnetic field.<sup>5</sup> Recent numerical experiments found no evidence for the chiral magnetic effect using their lattice model for a Weyl semimetal.<sup>6</sup> Charge transport in Weyl semimetals in the presence of disorder have also been studied, where they found two distinct regimes for the conductivity.<sup>7</sup> The direct observation of Fermi arcs or the anomalous Hall effect would be good evidence for the existence of a Weyl semimetal.

Although Weyl semimetals have not yet been observed there are several candidates. The pyrochlore iridates<sup>2,8–10</sup> are a promising host for the Weyl semimetallic phase. Proposals have also been made for the existence of a Weyl semimetallic phase in topological insulator heterostructures,<sup>4,11–13</sup> as well as in magnetically doped topological insulators.<sup>14,15</sup> A recent paper shows that it may even be possible to induce a topological phase transition to a Weyl semimetal using the electron-phonon interaction.<sup>16</sup>

The optical conductivity in a variety of quasicrystalline materials is linear over a broad range in frequencies.<sup>17</sup> This has been interpreted as evidence for Dirac fermions in these materials. Further evidence is needed to show that the physics in the quasicrystalline samples is due to Weyl fermions and not simply Dirac fermions. The magneto-optical response<sup>18–20</sup> is one possible tool that can help distinguish various exotic materials.

In this paper we compute the magneto-optical conductivity for a single Weyl point. For  $N_W$  Weyl nodes the conductivity simply scales by a factor of  $N_W$ . We find that the transverse optical conductivity is a series of asymmetric peaks with onsets proportional to the square root of the magnetic field.

PHILLIP E. C. ASHBY AND J. P. CARBOTTE

PHYSICAL REVIEW B **87**, 245131 (2013)

These peaks lie on the background of the zero magnetic field limit. The structure of these peaks as the chemical potential is changed is rich, and its behavior follows from the underlying dispersive Landau levels. We obtain formulas for the absorptive parts of both the transverse and Hall conductivities in the clean limit. Lastly, we examine the conductivity for circularly polarized light, as well as the semiclassical limit. These all provide verifiable predictions distinct to Dirac physics that can give additional support for the existence of a Weyl semimetal.

## II. DYNAMICAL CONDUCTIVITY OF A WEYL SEMIMETAL

The Hamiltonian for an isolated Weyl point in a magnetic field is given by

$$\mathcal{H} = \left[ -i\nabla + \frac{e}{c}\mathbf{A} \right] \cdot \boldsymbol{\sigma}, \quad (2)$$

where  $e$  is the electron charge and  $c$  is the speed of light. In the above we have ignored the effect of Zeeman splitting since this effect should be small at accessible magnetic field strengths. The spin degeneracy is accounted for in the number of Weyl points  $N_W$ . We consider a field  $\mathbf{B} = B\hat{z}$ , and use the gauge  $A_y = A_z = 0$  and  $A_x = -By$ . We work in units where  $\hbar = k_B = v_F = 1$ . It is convenient to define the magnetic length which is given by  $l_B^2 = c/eB$ . We define the operators

$$a = \frac{l_B}{\sqrt{2}}(\Pi_x - i\Pi_y), \quad (3)$$

$$a^\dagger = \frac{l_B}{\sqrt{2}}(\Pi_x + i\Pi_y), \quad (4)$$

where  $\boldsymbol{\Pi} = -i\nabla + e\mathbf{A}$ . Then, the Hamiltonian is given by the following set of  $2 \times 2$  matrices

$$\mathcal{H} = \begin{pmatrix} k_z & \frac{\sqrt{2}}{l_B}a \\ \frac{\sqrt{2}}{l_B}a^\dagger & -k_z \end{pmatrix}. \quad (5)$$

First we find solutions to the eigenvalue problem  $\mathcal{H}\psi = E\psi$ . We take  $\psi = \begin{pmatrix} \lambda u_{n\lambda} \\ v_{n\lambda} \end{pmatrix}$  and for  $n \neq 0$  we obtain

$$\pm E_n = \pm \sqrt{\frac{2n}{l_B^2} + k_z^2} = \lambda \sqrt{\frac{2n}{l_B^2} + k_z^2} = E_{n\lambda} \quad (6)$$

and

$$v_{n\lambda} \frac{\sqrt{2n}}{l_B} = u_{n\lambda} \lambda (E_{n\lambda} - k_z). \quad (7)$$

This is the same equation as for a superconductor, with the identification  $k_z = \epsilon$ ,  $E_{n\lambda} = E$  and  $\sqrt{2n}/l_B = \Delta$ . So

$$u_{n\lambda} = \sqrt{\frac{1}{2} \left( 1 + \frac{k_z}{E_{n\lambda}} \right)}, \quad (8)$$

$$v_{n\lambda} = \sqrt{\frac{1}{2} \left( 1 - \frac{k_z}{E_{n\lambda}} \right)}. \quad (9)$$

For  $n = 0$  we have

$$E_0 = -k_z \quad (10)$$

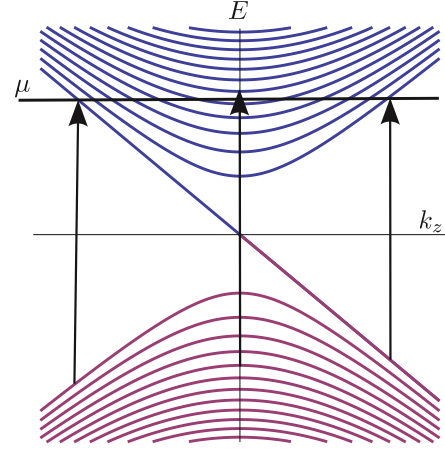


FIG. 1. (Color online) Dispersive Landau level structure for a Weyl semimetal at finite chemical potential. In this figure the chemical potential lies between the fifth and sixth Landau levels. The arrow at  $k_z = 0$  shows an interband transition from  $n = 5$  to  $n = 6$ . These interband transitions at  $k_z = 0$  give the main set of peaks shown in Fig. 2. The two transitions at finite  $k_z$  occur between the  $n = 0$  and  $n = 1$  Landau levels. They occur when  $\mu$  lies between two Landau levels and are responsible for the additional bumps seen in Fig. 4.

and

$$\psi = \begin{pmatrix} 0 \\ 1 \end{pmatrix}. \quad (11)$$

These equations describe the energy level structure and wave functions for the set of 3D Landau levels generated by the magnetic field. Unlike in the 2D case these Landau levels are dispersive (in  $k_z$ ) as shown in Fig. 1. The structure of these energy levels will control the shape of the dynamical conductivity, as we will elaborate on later.

The dynamical conductivity tensor can be obtained from the Kubo formula. Expressed in the Landau level basis in the clean limit we have

$$\sigma_{\alpha\beta} = -\frac{ie^2}{2\pi l_B^2} \sum_{nn'} \sum_{\lambda\lambda'} \int \frac{dk_z}{2\pi} \left( \frac{f(E_{n\lambda}) - f(E_{n'\lambda'})}{E_{n\lambda} - E_{n'\lambda'}} \right) \times \frac{\langle \psi_{n,\lambda,k_z} | j_\alpha | \psi_{n',\lambda',k_z} \rangle \langle \psi_{n',\lambda',k_z} | j_\beta | \psi_{n,\lambda,k_z} \rangle}{\omega + E_{n\lambda} - E_{n'\lambda'} + i0^+}, \quad (12)$$

where  $f(x) = 1/(1 + e^{\beta(x-\mu)})$ ,  $\beta$  is the inverse temperature, and  $\mu$  is the chemical potential. The current operators are given by  $j_\alpha = i[\mathcal{H}, x_\alpha] = \sigma_\alpha$ . The chemical potential is related to the density of carriers  $n_0$  through the density of states in a magnetic field  $N(\omega)$  by

$$n_0 = \int_{-\infty}^{\infty} d\omega N(\omega) f(\omega), \quad (13)$$

$$N(\omega) = \frac{1}{2\pi^2 l_B^2} \left[ 1 + 2 \sum_{n=1}^{\infty} \text{Re} \left( \frac{|\omega|}{\sqrt{\omega^2 - 2n}} \right) \right]. \quad (14)$$

We first perform the sum over  $\lambda$  and  $\lambda'$ , this introduces extra terms for the  $n = 0$  level, but these additional terms all vanish.

Then, for the dissipative components of the conductivity tensor  $\text{Re}(\sigma_{xx})$  and  $\text{Im}(\sigma_{xy})$  we arrive at

$$\begin{aligned} \text{Re}(\sigma_{xx}) = & -\frac{e^2}{8l_B^2} \sum_n \int \frac{dk_z}{2\pi} \left[ \left( \frac{f(E_n) - f(E_{n+1}) + f(-E_{n+1}) - f(-E_n)}{E_n - E_{n+1}} \right) \left( 1 - \frac{k_z^2}{E_n E_{n+1}} \right) \delta(\omega + E_n - E_{n+1}) \right. \\ & \left. + \left( \frac{f(E_{n+1}) - f(-E_n) + f(E_n) - f(-E_{n+1})}{E_n + E_{n+1}} \right) \left( 1 + \frac{k_z^2}{E_n E_{n+1}} \right) \delta(\omega - E_n - E_{n+1}) \right], \end{aligned} \quad (15)$$

and

$$\begin{aligned} \text{Im}(\sigma_{xy}) = & -\frac{e^2}{8l_B^2} \sum_n \int \frac{dk_z}{2\pi} \left[ \left( \frac{f(E_{n+1}) - f(E_n) + f(-E_{n+1}) - f(-E_n)}{E_n - E_{n+1}} \right) \left( 1 - \frac{k_z^2}{E_n E_{n+1}} \right) \delta(\omega + E_n - E_{n+1}) \right. \\ & \left. + \left( \frac{f(-E_n) - f(E_{n+1}) + f(E_n) - f(-E_{n+1})}{E_n + E_{n+1}} \right) \left( 1 + \frac{k_z^2}{E_n E_{n+1}} \right) \delta(\omega - E_n - E_{n+1}) \right]. \end{aligned} \quad (16)$$

In this problem the magnetic length  $l_B$  sets a natural energy scale for the problem. So, for convenience, we define  $\bar{\omega} = l_B \omega$ ,  $\bar{k} = l_B k_z$ , and  $\bar{E}_n = l_B E_n = \sqrt{2n + \bar{k}^2}$ . This choice of units will allow us to produce a single plot for all magnetic fields. In the clean limit we can use the  $\delta$  functions to do the integration over  $k_z$ . We find that there are contributions from

$$\bar{k} = \bar{k}_{\pm} = \pm \frac{1}{2} \sqrt{4 - 4\bar{\omega}^2(2n + 1) + \bar{\omega}^4}, \quad (17)$$

and we obtain the following formulas for the absorptive part of the conductivity tensor:

$$\begin{aligned} \text{Re}(\sigma_{xx}) = & \frac{e^2}{8\pi l_B} \left[ \frac{\sinh\left(\frac{2+\bar{\omega}^2}{2\bar{\omega}T}\right)}{\cosh\left(\frac{\bar{\mu}}{T}\right) + \cosh\left(\frac{2+\bar{\omega}^2}{2\bar{\omega}T}\right)} - \frac{\sinh\left(\frac{2-\bar{\omega}^2}{2\bar{\omega}T}\right)}{\cosh\left(\frac{\bar{\mu}}{T}\right) + \cosh\left(\frac{2-\bar{\omega}^2}{2\bar{\omega}T}\right)} \right] \sum_{n=0}^{\lfloor \frac{(\bar{\omega}^2-2)^2}{8\bar{\omega}^2} \rfloor} \left[ \frac{|2(2n+1) - \bar{\omega}^2|}{\bar{\omega}\sqrt{\bar{\omega}^4 - 4\bar{\omega}^2(2n+1) + 4}} \theta(|\sqrt{2} - \bar{\omega}|) \right], \\ -\text{Im}(\sigma_{xy}) = & \frac{e^2}{8\pi l_B} \left[ \frac{e^{\bar{\mu}/T} + \cosh\left(\frac{2-\bar{\omega}^2}{2\bar{\omega}T}\right)}{\cosh\left(\frac{\bar{\mu}}{T}\right) + \cosh\left(\frac{2-\bar{\omega}^2}{2\bar{\omega}T}\right)} - \frac{e^{\bar{\mu}/T} + \cosh\left(\frac{2+\bar{\omega}^2}{2\bar{\omega}T}\right)}{\cosh\left(\frac{\bar{\mu}}{T}\right) + \cosh\left(\frac{2+\bar{\omega}^2}{2\bar{\omega}T}\right)} \right] \sum_{n=0}^{\lfloor \frac{(\bar{\omega}^2-2)^2}{8\bar{\omega}^2} \rfloor} \left[ \frac{|2(2n+1) - \bar{\omega}^2|}{\bar{\omega}\sqrt{\bar{\omega}^4 - 4\bar{\omega}^2(2n+1) + 4}} \theta(|\sqrt{2} - \bar{\omega}|) \right]. \end{aligned} \quad (18)$$

In the above expressions  $\lfloor x \rfloor$  denotes the integer part of  $x$ .  $\text{Re}(\sigma_{xx})$  contains a series of peaks that sit on a linear background (Fig. 2). The background is the result for free Dirac fermions in absence of a magnetic field, namely  $\sigma_0 = \frac{e^2}{24\pi} |\omega|$ . In the units of our plots this is a straight line with slope 1/3. In the inset of Fig. 2 we show the real part of  $\sigma_{xx}$  over a larger frequency range, showing that it becomes linear at large  $\bar{\omega}$  with small oscillations from the Landau level structure. For  $\mu = 0$  the peaks occur at  $\bar{\omega} = \sqrt{2(n+1)} + \sqrt{2n}$  for integer  $n$ . The series of peaks corresponds to allowed interband transitions in the Landau level structure. This peak spacing is proportional to  $\sqrt{B}$ . From an experimental point of view this means one can see well spaced peaks even for modest fields. The asymmetry of the peaks is reflected by the square root singularity in Eq. (18), physically it comes from the dispersive structure of the Landau levels. The long tails of the peaks originate from the square root singularity and add together to provide the linear background we observe. In Fig. 2 we have shown the real conductivity for three values of the chemical potential. These values of the chemical potential are given by the energies of the Landau levels. We see that as the chemical potential is increased, the peaks at low energies disappear, and the optical spectral weight is entirely transferred into an intraband peak at low frequency. The pattern for how the peaks disappear is reminiscent of what happens in graphene.<sup>21</sup> For comparison

we have calculated the optical conductivity for graphene (Fig. 3). Indeed, the peaks occur at the same positions as for a Weyl semimetal, and disappear as the chemical potential is increased. However, in graphene the Landau levels are nondispersive, and changes to the optical conductivity can only happen when the chemical potential passes through a Landau level. In a Weyl semimetal, the dispersive nature of the Landau levels produces a richer structure. Note the double peak structure associated with the intraband peak in the dashed curve of Fig. 3 at low energy. One comes from the  $1 \rightarrow 2$  transition and the other from the  $2 \rightarrow 3$  transition. Both are allowed for  $\mu = 2$  which falls in the middle of a Landau level.

Figure 4 shows how the dispersive Landau level structure affects the optical conductivity. The top panel shows the evolution as the chemical potential is moved between two adjacent Landau levels. Unlike in graphene, the spectral weight of the interband peaks is continuously redistributed into the intraband peak. The bottom panel shows how the conductivity changes as the chemical potential moves through a Landau level. As the chemical potential passes through a Landau level there is a large redistribution of spectral weight, much like in graphene. The lowest peak in the solid black curve disappears entirely as  $\mu$  sweeps through the energy of the first Landau level, while the rest of the curve is unaffected. It reappears as a peak in the dashed orange curve that comes from the intraband

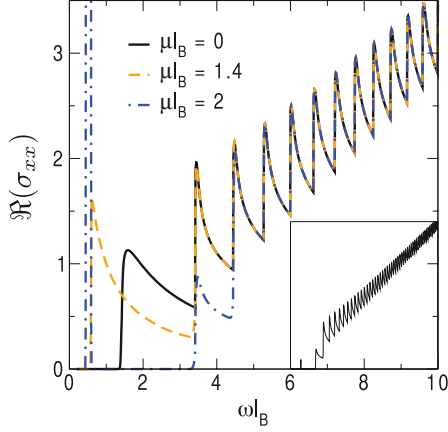


FIG. 2. (Color online) The real part of the optical conductivity (in units of  $e^2/8\pi l_B$ ) for  $\mu l_B = 0, 1.4,$  and  $2$  as a function of  $\omega l_B$ . In this figure we took  $Tl_B = 0.01$ . The conductivity is a series of peaks which sit on a linear background. These peaks occur at the  $k_z = 0$  value of the Landau levels shown in Fig. 1. The inset shows the  $\mu = 0$  conductivity over a larger frequency range, demonstrating its linearity. The background conductivity should be the result for free fermions, which is a straight line of slope  $1/3$  in our units.

transition between the  $n = 1$  and  $n = 2$  Landau levels. The tails of this new peak overlap with the original curve. As  $\mu$  is incremented further to  $2$  (the energy of the  $n = 2$  Landau level) the second peak in the black curve also becomes modified and now carries only half its original spectral weight. In a next step the remainder of this second peak will entirely disappear into the intraband transitions. The dispersive Landau levels decorate the graph with additional features. Both the top and bottom panel of Fig. 4 show additional shoulders that are not

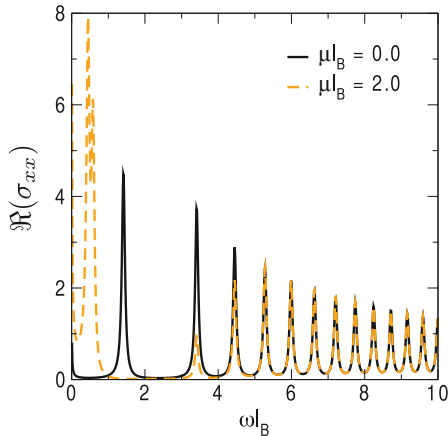


FIG. 3. (Color online) The real part of the optical conductivity (in units of  $e^2/8\pi l_B$ ) for graphene in the clean limit. Here  $Tl_B = 0.01$ . For  $\mu = 0$  there is a series of peaks at  $\tilde{\omega} = \sqrt{2(n+1)} + \sqrt{2n}$ . As  $\mu$  is increased these peaks disappear and are transferred into the intraband peak at low frequency.

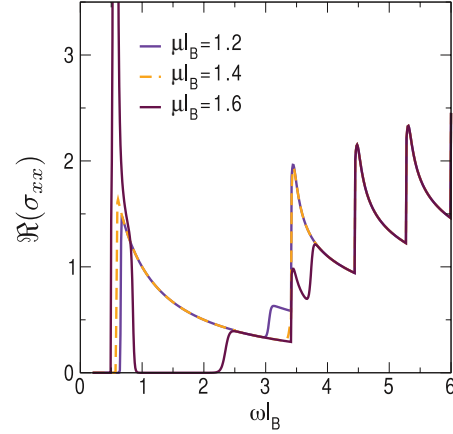
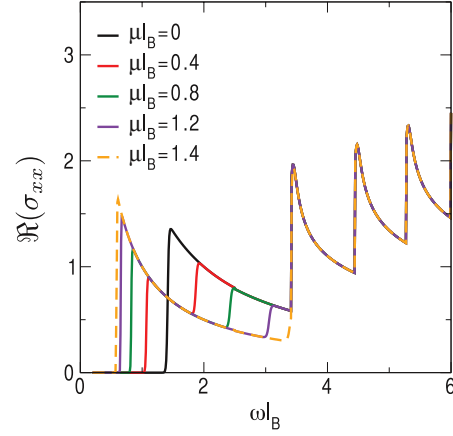


FIG. 4. (Color online) The real part of the conductivity (in units of  $e^2/8\pi l_B$ ) as a function of frequency for several values of the chemical potential. The top panel illustrates how the conductivity changes as the chemical potential sweeps between adjacent Landau levels. The bottom panel illustrates the change in the optical conductivity as a Landau level is crossed.

located at the signature frequencies  $\tilde{\omega} = \sqrt{2(n+1)} + \sqrt{2n}$ . These additional features are interband transitions involving the zeroth Landau level. More precisely they are the  $n = 0 \rightarrow n = 1$  and  $n = 1 \rightarrow n = 0$  transitions. Since the zeroth Landau level is an envelope for all the other Landau levels these additional features exist for all values of the chemical potential. For a chemical potential  $\tilde{\mu}$  the shoulders onset at  $\tilde{\omega} = \tilde{\mu} + \sqrt{\tilde{\mu}^2 + 2}$  and  $\tilde{\omega} = \tilde{\mu} + \sqrt{\tilde{\mu}^2 - 2}$ .

So far we have only discussed the diagonal conductivity  $\text{Re}(\sigma_{xx})$ . For experiments that probe the polarization of light, such as the Faraday and Kerr effects, the quantity  $\sigma_{\pm} = \sigma_{xx} \pm i\sigma_{xy}$  is appropriate.  $\sigma_+$  describes light with right handed polarization, and  $\sigma_-$  describes light with left handed polarization. The absorptive part of  $\sigma_{\pm}$  is  $\text{Re}(\sigma_{\pm}) = \text{Re}(\sigma_{xx}) \mp \text{Im}(\sigma_{xy})$ . A plot of  $\text{Re}(\sigma_-)$  is shown in Fig. 5. For left handed light there is a cancellation between the Hall conductivity and the longitudinal conductivity in the frequency range  $\omega \lesssim 2\mu$ .

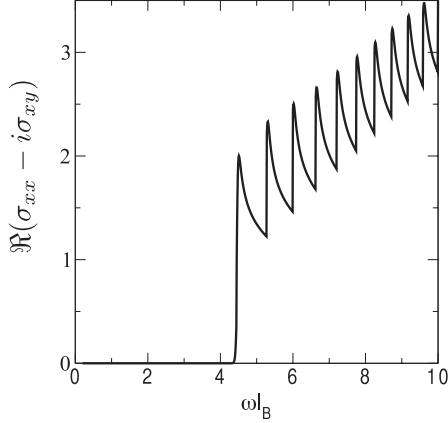


FIG. 5. The real part of the optical conductivity (in units of  $e^2/8\pi l_B$ ) for left handed circularly polarized light for  $\bar{\mu} = 2.0$  and  $\bar{T} = 0.01$ . In the low temperature limit, the imaginary part of the Hall conductivity exactly cancels the real part of the diagonal conductivity for  $\bar{\omega} \lesssim 2\bar{\mu}$ .

For right handed polarization (not shown) the peaks in the region  $\omega \lesssim 2\mu$  have double the magnitude as in Fig. 2. The presence of peaks for left circularly polarized light in this region could be a signature of correlation effects.

To realistically treat the problem of disorder (especially at large scattering rates) one would need the study of the Kubo formula expressed in terms of the spectral density  $A(k, \omega)$ . By solving a Boltzmann equation, one could obtain an expression for the self-energy. The imaginary part of the self-energy then serves to broaden the spectral densities. Here we capture the effect phenomenologically by introducing a scattering rate  $\Gamma$ . By making the replacement

$$\delta(z) \rightarrow \frac{1}{\pi} \frac{\Gamma}{\Gamma^2 + z^2} \quad (20)$$

in Eq. (15) we can understand how weak scattering will effect the conductivity. This replacement should give a qualitatively correct picture for small values of the inverse scattering time  $\bar{\Gamma}$ .

Figure 6 shows the real part of the transverse conductivity for  $\bar{\Gamma} = 0.05, 0.1, \text{ and } 0.2$ . The straight red line shows the conductivity of free 3D fermions  $\sigma_0$  for comparison. The disorder tends to smear out the peaks, and at large  $\omega l_B$  the conductivity trends towards the free limit as the disorder is increased. In particular the scattering rate needs to be large compared to the energy level spacing to see any peaks. In Fig. 6 the first few peaks are still very well defined for  $\bar{\Gamma} = 0.2$ . For a Fermi velocity of  $v_F \sim 10^6$  m/s, and  $B$  measured in Tesla, this corresponds to a scattering rate of  $\Gamma \sim 7\sqrt{B}$  meV.

Finally we consider the semiclassical limit. The semiclassical limit occurs when the Landau level quantization is no longer important.<sup>22</sup> This occurs when the chemical potential is the largest energy scale in the problem. For  $\bar{E}_N < \bar{\mu} < \bar{E}_{N+1}$ , with  $N \gg 1$  we have that

$$\Delta \bar{E} = \bar{E}_{N+1} - \bar{E}_N \simeq \frac{1}{\bar{\mu}}. \quad (21)$$

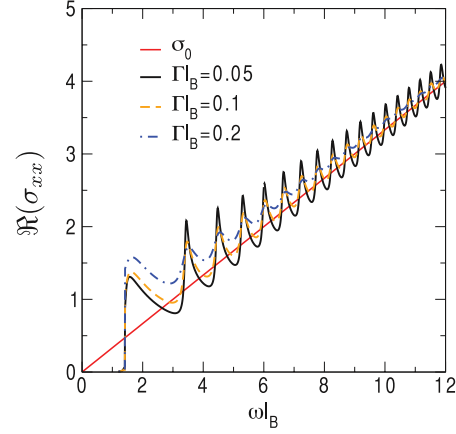


FIG. 6. (Color online) The real part of the optical conductivity (in units of  $e^2/8\pi l_B$ ) for  $\bar{\mu} = 0.0$  and  $\bar{T} = 0.01$  for several values of scattering rate  $\bar{\Gamma}$ . The red line shows the conductivity in the absence of a magnetic field. Increasing disorder tends to blur out the peaks towards the free limit.

In this limit, if one goes back to the unbarred units, the energy spacing goes like  $B$  in contrast to the  $\sqrt{B}$  behavior at small  $\mu$ . The semiclassical resonance is shown in Fig. 7 for  $\bar{\mu} = 5, \text{ and } 10$ . It appears as a peak at  $1/\bar{\mu}$ , and contains the spectral weight from the interband transitions that have disappeared between  $0 < \bar{\omega} < 2\bar{\mu}$ . In graphene where the Landau levels are flat this line is due only to the  $E_N \rightarrow E_{N+1}$  intraband transition. In the present case however, the dispersive Landau level structure gives contributions to this line shape from the set of transitions  $E_n \rightarrow E_{n+1}$  with  $n \in [0, N]$ . We can also see in Fig. 7 that as we doubled  $\mu$  the amount of area in the semiclassical peak quadrupled. This is a reflection of the linear background of the conductivity. For a chemical potential of  $\mu$ , interband

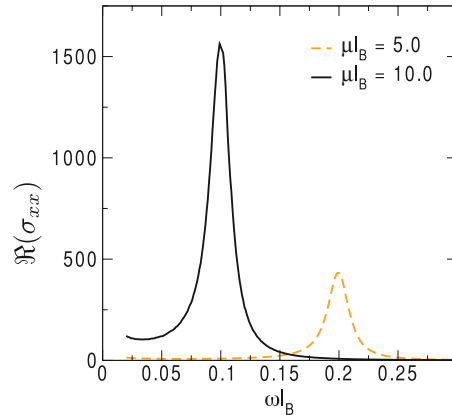


FIG. 7. (Color online) The real part of the optical conductivity (in units of  $e^2/8\pi l_B$ ) in the semiclassical limit. This occurs for large values of the chemical potential. All the spectral weight of the now forbidden interband transitions piles up into a single resonance at low frequency.

PHILLIP E. C. ASHBY AND J. P. CARBOTTE

PHYSICAL REVIEW B **87**, 245131 (2013)

transitions are forbidden out to  $\omega = 2\mu$ . The linearity of the conductivity combined with a sum rule shows that the area under this peak should scale like  $\mu^2$ , as we observe.

### III. DISCUSSION AND CONCLUSIONS

In this paper we calculated the optical conductivity for a Weyl semimetal in the presence of a magnetic field. We found that the dispersive Landau level structure produced a set of asymmetric peaks on a linear background. The peaks have a  $\sqrt{B}$  spacing, a signature of Dirac physics. The shape of the peaks reflects a square root singularity, and their long tails conspire together to give the linear background in this case. The positions of the peaks occur at the same frequencies as in graphene, although there are additional features when the chemical potential falls between two Landau levels. We also showed that for left hand polarized light that there is a cancellation for frequencies  $\omega < 2\mu$ , and peaks in this region could be associated with interaction effects. We showed that the semiclassical resonance has a typical line shape, but that it consists of many intraband transitions and has spectral weight that scale like  $\mu^2$ . We also showed the effect of weak disorder. The sharp peaks tend to blur out towards the linear background as the scattering rate increased. This may make the peaks hard to see in dirty samples. In particular, the scattering rate needs to be less than the Landau level spacing for the peaks to still be observable.

Finally, we would like to make a remark on units. Throughout the paper we have used the dimensionless units where  $l_B$  set the energy scale. For convenience we include the conversion to “real” units. For  $v_F$  measured in m/s and  $B$  measured in T we have

$$l_B^{-1} = 36.3v_F\sqrt{B} \times 10^{-9} \text{ eV}. \quad (22)$$

This conversion will be useful for comparing to experimental results. For the quasicrystals the chemical potential sits at the Fermi level. The estimated value for the Fermi velocity is  $v_F = 4.3 \times 10^7$  cm/s.<sup>17</sup> This sets the magnetic energy at  $l_B^{-1} = 15.6\sqrt{B}$  meV for the quasicrystalline candidates. In the pyrochlore iridates (such as  $\text{Y}_2\text{Ir}_2\text{O}_7$ ) the chemical potential also sits at the Fermi level and the Fermi velocities are estimated to be about an order of magnitude smaller than in graphene.<sup>2</sup> In this case the magnetic energy is approximately  $l_B^{-1} = 3.63\sqrt{B}$  meV. At accessible magnetic fields  $0 < \sqrt{B} \lesssim 6$ , and so the effects presented in this paper should be observable at reasonable energies.

### ACKNOWLEDGMENTS

This work was supported by the Natural Sciences and Engineering Research Council of Canada and the Canadian Institute for Advanced Research. We thank Tom Timusk for encouraging us to pursue this topic.

\*ashbype@mcmaster.ca

†carbotte@mcmaster.ca

<sup>1</sup>D. Huertas-Hernando, F. Guinea, and A. Brataas, *Phys. Rev. B* **74**, 155426 (2006).

<sup>2</sup>X. Wan, A. M. Turner, A. Vishwanath, and S. Y. Savrasov, *Phys. Rev. B* **83**, 205101 (2011).

<sup>3</sup>P. Goswami and S. Tewari, *arXiv:1210.6352* [cond-mat.mes-hall].

<sup>4</sup>A. A. Burkov and L. Balents, *Phys. Rev. Lett.* **107**, 127205 (2011).

<sup>5</sup>Z. Jian-Hui, J. Hua, N. Qian, and S. Jun-Ren, *Chin. Phys. Lett.* **30**, 027101 (2013).

<sup>6</sup>M. Vazifeh and M. Franz, *arXiv:1303.5784* [cond-mat.mes-hall].

<sup>7</sup>P. Hosur, S. A. Parameswaran, and A. Vishwanath, *Phys. Rev. Lett.* **108**, 046602 (2012).

<sup>8</sup>W. Witczak-Krempa and Y. B. Kim, *Phys. Rev. B* **85**, 045124 (2012).

<sup>9</sup>F. F. Tafti, J. J. Ishikawa, A. McCollam, S. Nakatsuji, and S. R. Julian, *Phys. Rev. B* **85**, 205104 (2012).

<sup>10</sup>J. J. Ishikawa, E. C. T. O’Farrell, and S. Nakatsuji, *Phys. Rev. B* **85**, 245109 (2012).

<sup>11</sup>A. A. Burkov, M. D. Hook, and L. Balents, *Phys. Rev. B* **84**, 235126 (2011).

<sup>12</sup>A. A. Zyuzin, S. Wu, and A. A. Burkov, *Phys. Rev. B* **85**, 165110 (2012).

<sup>13</sup>G. B. Halász and L. Balents, *Phys. Rev. B* **85**, 035103 (2012).

<sup>14</sup>G. Y. Cho, *arXiv:1110.1939* [cond-mat.str-el].

<sup>15</sup>P. Y. Chao-Xing Liu and X.-L. Qi, *Phys. Rev. B* **87**, 235306 (2013).

<sup>16</sup>I. Garate, *Phys. Rev. Lett.* **110**, 046402 (2013).

<sup>17</sup>T. Timusk, J. P. Carbotte, C. C. Homes, D. N. Basov, and S. G. Sharapov, *Phys. Rev. B* **87**, 235121 (2013).

<sup>18</sup>O. Fuseya and Fukuyama, *J. Phys. Soc. Jpn.* **81**, 013704 (2011).

<sup>19</sup>C. J. Tabert and E. J. Nicol, *Phys. Rev. Lett.* **110**, 197402 (2013).

<sup>20</sup>Z. Li and J. P. Carbotte, *arXiv:1306.1199* [cond-mat.mes-hall].

<sup>21</sup>V. P. Gusynin, S. G. Sharapov, and J. P. Carbotte, *J. Phys.: Condens. Matter* **19**, 026222 (2007).

<sup>22</sup>A. Pound, J. P. Carbotte, and E. J. Nicol, *Phys. Rev. B* **85**, 125422 (2012).

# Chapter 6

## Conclusions

In this thesis we presented the results for the finite frequency optical conductivity in a variety of materials that exhibit Dirac like physics in their low energy excitations.

Papers I and II describe calculations relevant for a new experimental technique, near field optics. Near field optics pushes spectroscopy into the finite momentum transfer regime. It can be used to study collective modes such as plasmons or plasmareons. It also allows for the extraction of the finite  $\mathbf{q}$  conductivity. Previously, measurements of the optical conductivity were limited to  $\sigma(q = 0, \omega)$ . That is, the conductivity only contained information about frequency. The new near field technique give information about both momentum,  $\mathbf{q}$  and frequency,  $\omega$ . This puts the technique on equal footing with ARPES. ARPES is able to directly probe the band structure of solids, but is limited by being a surface sensitive probe. The optical conductivity directly probes the bulk states. Thus, this near field optical technique will be able to directly probe the band structure of the bulk states.

Further extensions of this work can be the application of this technique to many other systems. It will be exciting to see what kinds of systems near field optics can be applied to. This technique may open the door to presently unmeasurable quantities. An example of such a quantity is the Hall viscosity. The Hall viscosity is the anti-symmetric part of the viscosity tensor (in analogy with the Hall conductivity). For systems that preserve time reversal it is guaranteed to vanish. For systems that spontaneously break time-reversal (like quantum Hall states) it may be non-vanishing.

It has been noted that the Hall viscosity is related to the  $q^2$  part of the finite momentum conductivity. Thus, it might be possible to extract information about the Hall viscosity from near field optics. This would be a very exciting possibility!

Papers III and IV focused on the application of the YRZ model of the underdoped cuprates. This model has been successful at agreeing qualitatively with a wide range of experiential data. In this thesis we presented the extension to the c-axis optical properties. Our calculations show excellent agreement with the existing experimental data. The YRZ model naturally explains many previously anomalous results since it naturally reconstructs the Fermi surface as doping is changed. Any model that has a reconstructed Fermi surface should also agree with the existing data. It would be very useful to find instances in which the YRZ model does not succeed. Perhaps more intimately linking it with a microscopic model will be able to expose some of the weaknesses of the YRZ model.

There are still some further directions that one could push the YRZ model. We added a scattering rate in an ad-hoc fashion. It would be nice to have a derivation for the form of the scattering rate, perhaps from the solution of a quantum Boltzmann equation. It is also not clear how to study the properties in a Magnetic field using the YRZ model. Since the model does not start with a Hamiltonian it is hard to know how to correctly add a magnetic field to the calculations. It would be very interesting to look for quantum oscillations in a magnetic field using an appropriate extension of the YRZ model.

Lastly, we considered a new topological class of materials, the Weyl semimetal. We focused on calculating the magneto-optical response, and found signatures of the underlying relativistic physics. Candidate materials could be checked for Weyl points by examining the Landau level structure in a magnetic field. A shortcoming of this calculation is that we only considered the bulk states. Weyl semimetals also have interesting surface states that will make a contribution to the conductivity. The surface state contribution could play an important role, especially at low energies. Starting from a simple microscopic Hamiltonian, it would be possible to include the effects of both the bulk and the surface states. Our inclusion of scattering was also treated in the simplest approximation. For a realistic discussion of scattering one needs to go

---

back to the spectral functions in a magnetic field and add the appropriate self-energy corrections. This direction may need to be explored if scattering is important in candidate Weyl semimetals.

Weyl semimetals have still not been observed in Nature, and so it is important to classify them further. For the most part research has focused on the properties most directly related to their non-trivial topology. Further calculations could include the study of thermodynamic properties in a magnetic field, for example. It could also be interesting to look at the effect of a Weyl semimetal under strain. Graphene is known to have a very interesting response to strain. In graphene strain can induce pseudomagnetic fields on the order of 100's of Tesla. Once some candidate Weyl semimetals are more clearly established, one could look for the shear modes of the lattice and see if a similar effect is expected to exist in these materials.



# Bibliography

- [1] P. A. M. Dirac. The quantum theory of the electron. *Proceedings of the Royal Society of London. Series A*, 117(778):610–624, 02 1928.
- [2] Carl D. Anderson. The positive electron. *Physical Review*, 43(6):491–494, 03 1933.
- [3] Hermann Weyl. Elektron und gravitation. i. 56(5-6):330–352, 1929.
- [4] Conyers Herring. Accidental degeneracy in the energy bands of crystals. *Physical Review*, 52(4):365–373, 08 1937.
- [5] Conyers Herring. Effect of time-reversal symmetry on energy bands of crystals. *Physical Review*, 52(4):361–365, 08 1937.
- [6] B. I. Halperin and T. M. Rice. Possible anomalies at a semimetal-semiconductor transition. *Reviews of Modern Physics*, 40(4):755–766, 10 1968.
- [7] S.D. Beneslavskii A.A. Abrikosov. Possible existence of substances intermediate between metals and dielectrics. *Journal of Experimental and Theoretical Physics*, 59(4):1280, 1971.
- [8] A. A. Abrikosov and S. D. Beneslavskii. Some properties of gapless semiconductors of the second kind. 5(2):141–154, 1971.
- [9] Ashcroft and Mermin. *Solid State Physics*. Thompson Learning, 1976.

- 
- [10] Gerald D. Mahan. *Many-Particle Physics*. Plenum Press, 1990.
- [11] A. Altland and B. Simons. *Condensed Matter Field Theory*. Cambridge University Press, 2007.
- [12] P. R. Wallace. The band theory of graphite. *Physical Review*, 71(9):622–634, 05 1947.
- [13] N. D. Mermin and H. Wagner. Absence of ferromagnetism or antiferromagnetism in one- or two-dimensional isotropic heisenberg models. *Physical Review Letters*, 17(22):1133–1136, 11 1966.
- [14] P. C. Hohenberg. Existence of long-range order in one and two dimensions. *Physical Review*, 158(2):383–386, 06 1967.
- [15] K. S. Novoselov, A. K. Geim, S. V. Morozov, D. Jiang, Y. Zhang, S. V. Dubonos, I. V. Grigorieva, and A. A. Firsov. Electric field effect in atomically thin carbon films. *Science*, 306(5696):666–669, 10 2004.
- [16] O. Klein. Die reflexion von elektronen an einem potentialsprung nach der relativistischen dynamik von dirac. 53(3-4):157–165, 1929.
- [17] W. Meissner and R. Ochsenfeld. Ein neuer effekt bei eintritt der supraleitfähigkeit. 21(44):787–788, 1933.
- [18] HK Onnes. The resistance of pure mercury at helium temperatures. *Commun. Phys. Lab. Univ. Leiden*, 12:120, 1911.
- [19] F. London and H. London. The electromagnetic equations of the supraconductor. *Proceedings of the Royal Society of London. Series A, Mathematical and Physical Sciences*, 149(866):71–88, 03 1935.
- [20] V.L. Ginzburg and L.D. Landau. On the theory of superconductivity. *Zh.Eksp.Teor.Fiz.*, 20:1064–1082, 1950.
- [21] J. Bardeen, L. N. Cooper, and J. R. Schrieffer. Microscopic theory of superconductivity. *Physical Review*, 106(1):162–164, 04 1957.

- [22] Leon N. Cooper. Bound electron pairs in a degenerate fermi gas. *Physical Review*, 104(4):1189–1190, 11 1956.
- [23] L. P. Gor'kov. Microscopic derivation of the ginzburg-landau equations in the theory of superconductivity. *Sov. Phys. JETP*, 9:1364–1367, 1959.
- [24] W. Kohn and J. M. Luttinger. New mechanism for superconductivity. *Physical Review Letters*, 15(12):524–526, 09 1965.
- [25] J. G. Bednorz and K. A. Müller. Possible high  $T_c$  superconductivity in the BaCuO system. 64(2):189–193, 1986.
- [26] J. Georg Bednorz and K. Alex Müller. Perovskite-type oxides—the new approach to high- $T_c$  superconductivity. *Reviews of Modern Physics*, 60(3):585–600, 07 1988.
- [27] M. K. Wu, J. R. Ashburn, C. J. Torng, P. H. Hor, R. L. Meng, L. Gao, Z. J. Huang, Y. Q. Wang, and C. W. Chu. Superconductivity at 93 K in a new mixed-phase Y-Ba-Cu-O compound system at ambient pressure. *Physical Review Letters*, 58(9):908–910, 03 1987.
- [28] Kai-Yu Yang, T. M. Rice, and Fu-Chun Zhang. Phenomenological theory of the pseudogap state. *Phys. Rev. B*, 73(17):174501–, 05 2006.
- [29] R. M. Konik, T. M. Rice, and A. M. Tsvelik. Doped spin liquid: Luttinger sum rule and low temperature order. *Phys. Rev. Lett.*, 96(8):086407–, 03 2006.
- [30] L. D. Landau. *Sov. Phys. JETP*, 3:920, 1956.
- [31] J. M. Luttinger. Fermi surface and some simple equilibrium properties of a system of interacting fermions. *Physical Review*, 119(4):1153–1163, 08 1960.
- [32] L. P. Gor'kov, A. A. Abrikosov and I. E. Dzyaloshinskii. *Methods of Quantum Field Theory in Statistical Physics*. Dover, New York, 1975.

- 
- [33] A. Levchenko, T. Micklitz, M. R. Norman, and I. Paul. Transport implications of fermi arcs in the pseudogap phase of the cuprates. *Phys. Rev. B*, 82(6):060502–, 08 2010.
- [34] C. L. Kane and E. J. Mele.  $Z_2$  topological order and the quantum spin hall effect. *Physical Review Letters*, 95(14):146802–, 09 2005.
- [35] K. v. Klitzing, G. Dorda, and M. Pepper. New method for high-accuracy determination of the fine-structure constant based on quantized hall resistance. *Physical Review Letters*, 45(6):494–497, 08 1980.
- [36] G. E. Volovik. Flat band in the core of topological defects: Bulk-vortex correspondence in topological superfluids with fermi points. 93(2):66–69, 2011.
- [37] H. B. Nielsen and M. Ninomiya. A no-go theorem for regularizing chiral fermions. *Physics Letters B*, 105(2–3):219–223, 10 1981.
- [38] Dam Thanh Son and Naoki Yamamoto. Berry curvature, triangle anomalies, and the chiral magnetic effect in fermi liquids. *Physical Review Letters*, 109(18):181602–, 11 2012.
- [39] A. A. Zyuzin, Si Wu, and A. A. Burkov. Weyl semimetal with broken time reversal and inversion symmetries. *Physical Review B*, 85(16):165110–, 04 2012.
- [40] A. A. Burkov and Leon Balents. Weyl semimetal in a topological insulator multilayer. *Physical Review Letters*, 107(12):127205–, 09 2011.
- [41] Zhou Jian-Hui, Jiang Hua, Niu Qian, and Shi Jun-Ren. Topological invariants of metals and the related physical effects. *Chinese Physics Letters*, 30(2):027101, 2013.
- [42] Xiangang Wan, Ari M. Turner, Ashvin Vishwanath, and Sergey Y. Savrasov. Topological semimetal and fermi-arc surface states in the electronic structure of pyrochlore iridates. *Physical Review B*, 83(20):205101–, 05 2011.

- 
- [43] T. Timusk, J. P. Carbotte, C. C. Homes, D. N. Basov, and S. G. Sharapov. Three-dimensional dirac fermions in quasicrystals as seen via optical conductivity. *Physical Review B*, 87(23):235121–, 06 2013.
- [44] m Bcsi and Attila Virosztek. Low-frequency optical conductivity in graphene and in other scale-invariant two-band systems. *Physical Review B*, 87(12):125425–, 03 2013.